UNICA

UNIVERSITÀ
DEGLI STUDI
DI CAGLIARI

Ph.D. DEGREE IN
PHYSICS

Cycle XXXVI

Purification of Argon via Distillation with Aria and Purity Monitoring for Dark Matter Searches

FIS/01

Ph.D. Student: Riccardo Stefanizzi

Supervisor Dott. Walter Bonivento

Final exam. Academic Year 2022/2023
Thesis defence: January 2024 Session

Phd in Physics

Purification of Argon via Distillation with Aria and Purity Monitoring for Dark Matter Searches

Supervisor:
Dott. Walter Bonivento

Candidate:
Riccardo Stefanizzi

XXXVI ciclo
Final exam Academic Year 2022/2023
Thesis defense: January 2024 Session

Chapter 0

Short Abstract

The search for dark matter is one of the most promising fields of physics research. Approximately 80% of the universe's matter is classifiable as non-baryonic dark matter. So far it has not yet been directly detected. To verify the existence of WIMPs, which are hypothesized to be dark matter particles, various methods, including direct interactions with ordinary matter, are being pursued. One of the most commonly used materials for WIMP detection is argon, forming the active target of the already completed DarkSide-50 experiment and the subsequent DarkSide-20k experiment. The latter will employ 20 tonnes of ultra-pure liquid argon to investigate interactions with dark matter.
In this thesis, I've analyzed the data obtained from DarkSide-50 to measure the consequences of potential contaminants in argon and their influence on the measurements. This method will allow us to establish a threshold for contaminants, mainly nitrogen and oxygen, below which the measurements have minimal or no impact.
The argon that is going to be used by DarkSide-20k, called Underground argon, will be extracted by the Urania facility in Colorado. To ensure that it fulfills the required level of purity, it must undergo chemical purification through cryogenic distillation. This constitutes the primary goal of the Aria project, the central focus of this thesis. Furthermore, a crucial aspect is the capability of the Aria distillation column to separate isotopes, which consequently can contribute to achieving radiopurity, in particular concerning the isotope ^{39}Ar inside the argon extracted from the Urania facility.
In this thesis, I've performed several simulations for the cryogenic distillation process and participated in the run of the prototype column Seruci-0, in particular setting up and analyzing the sampling system. The results of my work were summarized in the publications [1] and [2]. All these results are original and were not present in the scientific literature beforehand.
The purpose of Aria extends beyond the DarkSide-20k procurement of argon. The Underground argon will also be provided for the veto system of the LEGEND-1000 experiment for neutrino-less double beta decay search. Moreover, Aria will be used for the isotopic enrichment of germanium for future expansion of LEGEND-1000, as well as the production of isotopes with various applications in different fields, such as ^{13}C, ^{18}O, ^{17}O, ^{15}N. I've also performed simulations for some of these isotopes.

Contents

List of Figures

Chapter 1

Introduction

Dark matter is an unseen type of matter that does not interact with light or does not emit any form of radiation. Its detection and study pose a significant challenge. However, several models suggest how dark matter plays a fundamental role in the formation of the universe.

The notion of dark matter was initially postulated by astronomer Fritz Zwicky [3]. He observed that the gravitational forces holding galaxy clusters together exceeded what could be explained only by visible matter. To explain this disparity, he proposed the existence of an invisible substance, which was called dark matter.

Much evidence supporting the existence of dark matter has been discovered in the last century. One of the most important pieces of evidence comes from the study of galactic rotational velocities. According to the distribution of visible matter in galaxies, the observed velocities of stars should decrease as we move farther away from the galactic center. However, these velocities remain constant or even increase according to different observations, implying the presence of additional unseen matter.

Even though its precise composition is unknown, various theoretical models propose that dark matter consists of exotic particles interacting only weakly with ordinary matter. These particles do not emit, absorb, or reflect radiation, and this explains why traditional astronomical instruments cannot directly detect dark matter.

Dark matter is fundamental as it gravitationally interacts with ordinary matter and provides the gravitational pull necessary to keep galaxies and galaxy clusters together. The observed structures and motions of celestial objects would be inexplicable without dark matter. It is expected to play a fundamental role in the birth of the universe and the formation of galaxies as well [4].

Dark Matter presence is suggested by many phenomena that are caused or influenced by it. They are internal movements of galaxies, irregularities in the cosmic microwave background radiation on a large scale, interactions of colliding galaxy clusters, and other phenomena. It is widely acknowledged within the scientific community today that approximately 80% of the matter in the universe exists in a non-baryonic state, which does not emit or absorb electromagnetic radiation.

However, dark matter has not yet been found via direct detection. Various indirect methods have been used looking for its gravitational effects and interactions with other particles. Many experiments are currently looking for evidence of dark matter particles, such as underground detectors and particle accelerators. They will be discussed in the next chapters.

Detecting dark matter and understanding its nature are two of the most important challenges in physics. Its discovery would deepen our comprehension of the universe's

composition.

One possible candidate for dark matter is *weakly interacting massive particles* (WIMPs). According to this hypothesis, WIMPs are sufficiently heavy to be in a non-relativistic state when they detach from the hot plasma during the early stages of the universe. However, no such particles are accounted for in the Standard Model, nor have they been directly detected at particle accelerators or through other means. As a result, the true nature of dark matter is yet to be understood. While the Standard Model of particle physics does not offer a valid candidate for dark matter, different theories beyond the Standard Model propose the existence of WIMPs, that could potentially explain its composition. Therefore, the discovery of WIMPs would be evidence for new physics that extends beyond the Standard Model [5].

WIMP searches can be categorized into three main groups:

1. Direct detection experiments using shielded underground detectors.
2. Indirect detection methods involving ground-based telescopes that seek signals caused by dark matter annihilation.
3. Direct production of dark matter particles through high-energy collisions taking place at particle colliders.

To detect WIMPs, at least 0.1–10 tons of targets may be required at low background. Thus we need cosmic ray suppression by locating the experiments deep underground, selecting materials for low radioactivity, and using instruments that can reject residual backgrounds looking at the sought-after nuclear recoil events [7].

One potential target is argon, which distinguishes itself in Atmospheric Argon (AAr) and Underground Argon (UAr). The first contains a naturally occurring radioisotope (^{39}Ar) with an isotopic abundance of $8 \cdot 10^{16}$. This β-emitter poses concerns due to its activity of approximately 1 Bq/kg and it contributes to background and pile-up issues. The liquid argon target provides an advantageous capability to distinguish between nuclear and electron recoil scintillation signals through pulse-shape discrimination. However, this discrimination method does not apply to experiments that solely examine the ionization signal. Underground Argon (UAr), extracted from subterranean wells, offers a substantially reduced concentration of ^{39}Ar. UAr plays a fundamental role in direct dark matter search experiments and will be extracted from the Urania [6] facilities.

Regarding direct detection of WIMPs, DarkSide-50 was a pivotal experiment with an exposure duration of 532.4 days dedicated to the search for dark matter. It employed a Time Projection Chamber (TPC) filled with approximately 50 kg of high-purity liquid argon, complemented by a liquid-scintillator veto (LSV) for the rejection of neutrons and -rays, as well as a water Cherenkov veto (WCV) for shielding purposes and the detection of muons. This technique provides excellent background rejection capabilities by detecting both the scintillation light and ionization electrons generated by recoiling nuclei [7]. Based on the measured upper limit on ^{39}Ar contamination in UAr used in DarkSide-50, which is more than 1500 times lower than atmospheric argon, this corresponds to a ^{39}Ar background equivalent to at least $2.15 \cdot 10^5$ kg/d or 0.6 t/yr with UAr. This crucial outcome demonstrates that the ^{39}Ar background in the full DarkSide-50 run using UAr can be effectively suppressed, providing support for the claim that future ton-scale LAr TPCs (DarkSide-20k) with significantly larger UAr exposures can be free of ^{39}Ar background contribution. More

details about the principles of the DarkSide experiments will be explained in the next chapters of this thesis. The DarkSide-20k experiment aims to achieve a remarkable sensitivity for directly detecting WIMPs, with a target cross-section of $1.2 \cdot 10^{-47}\text{cm}^2$ for a mass of 1 TeV/c^2. This would represent a significant enhancement of at least 50 times compared to PandaX-II [8] findings, which have been the most successful thus far at the same mass. The DarkSide-20k experiment will employ a liquid argon time projection chamber (LAr TPC) detector with an active (fiducial) mass of 20 tons, accumulating a total exposure of 100 tonne-years over a 5-year run. Additionally, thanks to its exceptionally low instrumental background, DarkSide-20k has the potential to extend its operation to a decade, leading to an exposure of 200 tonne-years and achieving a sensitivity of $7.4 \cdot 10^{-48}\text{cm}^2$.

In this thesis, we will also analyze the data from DarkSide-50 to quantify the effects of potential impurities in argon and we will explain how these impurities impact the measurements. Doing so we will be able to identify a threshold for impurities, primarily nitrogen and oxygen, below which the measurements are not significantly affected. Consequently, we will be able to establish a minimum target for the purity of argon after it has been purified. To understand this, the waveforms of DarkSide-50 were analyzed, and at the same time, a study was conducted to comprehend the relationship between single-electron events (prompt emission events believed to be caused by isolated electrons) and impurities, particularly nitrogen.

What has been said about the argon used for DarkSide-20k is fundamental and is closely linked to the Aria project, which is one of the key topics of this thesis. The ongoing installation of the cryogenic isotopic distillation facility, Aria, located in a mine shaft at CarboSulcis S.p.A. in Nuraxi-Figus (SU), Italy, aims to achieve chemical purification of UAr from impurities and a possible future further reduction of the ^{39}Ar isotopic fraction for DarkSide LowMass experiment [1]. This plant has a production rate of several kilograms per day. The construction of the distillation column, measuring 350 meters and with an inner diameter of 31.8 centimeters, aligns with the requirements of both DarkSide LowMass [9] in terms of production capacity and DarkSide-20k in terms of effectively purifying the UAr from chemical impurities. We summarize the most important of the possible applications of the Aria cryogenic distillation column.

1. Chemical purification via distillation of undesired impurities in argon, such as N_2, O_2, CH_4, CO_2 and more. The simulations that will be shown and explained in the next chapters clearly show how these impurities can be reduced to completely negligible values (much smaller than the 1 ppm required according to [5]). Although more recent simulations, not yet confirmed and therefore not included in the thesis, indicate the potential to achieve levels below parts per billion (ppb) even with Seruci-0. Furthermore, the production rate could be greater than 25 kg/h and therefore the 100 t requested by DarkSide20k could be produced in a reasonable time. However, the capacity to generate flow may be constrained by the pipelines, and therefore, further experimental tests with the prototype are expected to confirm the actual flux (kg/h). Regarding chemical distillation, however, there are ongoing discussions about whether to perform it using the Seruci-0 prototype or Seruci-1, and whether to conduct it in a single pass (removing only nitrogen) or in two passes (removing the other possible impurities as well). Consequently, all these cases will be discussed in the thesis.

2. Further removal of ^{39}Ar from UAr for DarkSide LowMass as mentioned before.

Once the two main purposes have been concluded, the column can be used for other types

of separations:

1. Oxygen isotopes: ^{18}O and ^{17}O concentration can be enhanced up 99.5% and 4% respectively. They are used in the field of medical physics in particular for PET (^{18}O) and in the production chain of ^{18}F for magnetic resonance.

2. ^{74}Ge. Via GeH_4 the concentration of the isotope ^{74}Ge may be increased and used for LEGEND, and experiment looking for neutrinoless double beta decay.

3. All CO and NO isotopes can be separated efficiently introducing a second distillation column that will be discussed in the next chapters.

So far, two runs have been conducted using Seruci-0, a prototype of approximately 30 meters in height, consisting of only one of the modules that will constitute the actual Seruci-1 column. Despite its significantly reduced height, its performance is expected to be proportionally analogous to that of Seruci-1, more details in [1]. The first run involved the isotopic separation of nitrogen, while the second run focused on the same process with argon. Both runs lead to excellent results, demonstrating how even the prototype alone is sufficient to achieve and measure a significant isotopic separation. Furthermore, these runs have been fundamental in proving the reliability of the system and the instrumentation. Specifically, the separation is measured using a Universal Gas Analyzer (UGA), which is a mass spectrometer with an internal pressure reduction system that allows for the differentiation of the various elements composing the gas coming from the column at approximately atmospheric pressure. To accurately measure the separation, it was necessary to comprehend, calibrate, and properly operate the UGA. Therefore, this will be extensively discussed in the upcoming chapters, alongside a description of the results obtained from the two test runs.

In the first chapter, we will delve into a detailed discussion of dark matter, the search for WIMPs, and the experiments encompassed by DarkSide (2.4). We will study the results from DarkSide-50 to understand the role of impurities in argon (3). Subsequently, we will explain the Aria project and how cryogenic distillation works, exploring its numerous applications (4). The next chapter will discuss the operation and use of the UGA (5.1), followed by the presentation of the results from the two Seruci-0 runs conducted so far (5.3, 5.2). We will then proceed to discuss the simulations carried out for the Seruci-0 and Seruci-1 columns (7.1, 6.2, 6), as well as ideas for potential future prototypes (7.2, 7.4).

Chapter 2

Dark matter and the DarkSide experiments

In this chapter after a brief introduction about Dark Matter 2.1 we are going to discuss WIMPs 2.2 and Dark Matter detection techniques. We will focus in particular on direct detection with detectors filled with noble gasses in liquid phase 2.3 and finally we will discuss DarkSide experiments 2.4: DarkSide-50 2.4.1 and DarkSide-20k 2.4.3. In the last part, we will discuss the theory behind a relevant issue of the TPC, that is the single electron candidates and events 2.4.5.

2.1 Dark Matter

As explained in "History of dark matter" [3] Fritz Zwicky in 1933, conducted a study on the redshifts of various galaxy clusters, and he focused in particular on the Coma Cluster, where he observed a significant dispersion in the velocities of eight galaxies exceeding thousands of km/s. While Hubble and Humason had previously noticed the high-velocity dispersion in Coma compared to other clusters, Zwicky applied the virial theorem to estimate the cluster's mass. Zwicky began his estimation by multiplying the number of observed galaxies (800) by the average mass of a galaxy. Hubble's idea of 10^9 solar masses was used as the basis for this estimation. Additionally, he assumed the size of the system, which he approximated around 10^6 light-years. Through this, he determined the potential energy of the system. Subsequently, he calculated the average kinetic energy and, lastly, the velocity dispersion. Based on his calculations, he expected that 800 galaxies with 10^9 solar masses and confined within a sphere of 10^6 light-years, would show a velocity dispersion of 80 km/s. However, the observed average velocity dispersion was approximately 1000 km/s. This led him to the idea that dark matter might exist in much greater quantities than visible matter. Current estimates suggest that the average density of dark matter in our galaxy is in a ratio of 5 compared to visible matter [3]. Under the assumption of spherical symmetry and considering a star located within the plane of a disk galaxy, according to Newtonian gravitational relationships, we would expect that the gravitational acceleration is equal and opposite to the centrifugal acceleration. This ensures that the star is in a stationary state and that means that its distance from the center of the galaxy is expected to remain constant.

$$\frac{v^2}{R} = \frac{M(R)G}{R^2} \tag{2.1}$$

where R is the distance from the center of the galaxy, G is the gravitational constant, v is the circular velocity of the star, and $M(R)$ is the mass included in a sphere of radius R

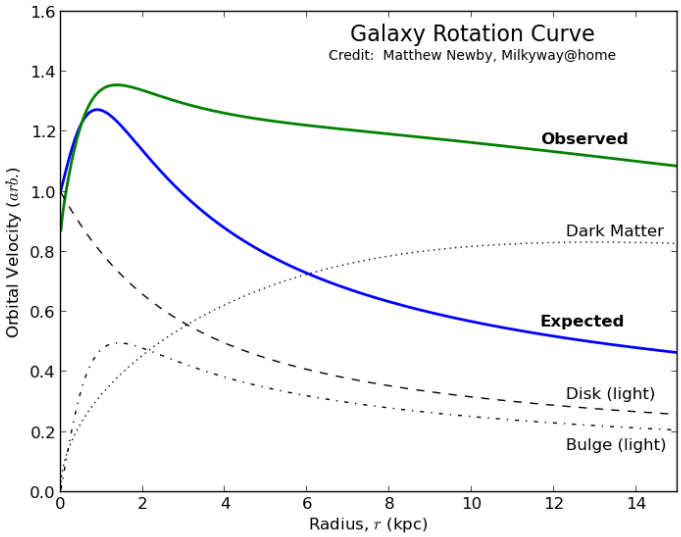

Figure 2.1: Example of the discrepancy between expected (blue) and observed (green) orbital velocity in a galaxy as a function of the distance from the center. The difference may be explained by the presence of the dark matter distribution (dashed line) [10]

centered in the center of the galaxy. Thus we get

$$M(R) = \frac{v^2 R}{G} \tag{2.2}$$

This is fundamental as it means that, if we know the distribution of the velocity of the stars of a given galaxy as a function of R we can determine the mass distribution. Alternatively, we can find the velocity as

$$v^2 = \frac{M(R)G}{R} \tag{2.3}$$

Clearly, these calculations would need to be refined with relativistic corrections. However, these would not significantly change the reasoning.

Observations of the luminous mass distribution within galaxies suggest how the majority of the mass is concentrated in their centers. Thus, the mass function M(R) increases as R^2 until reaching a radius comparable to that of the bulge, where it levels off to a constant value. Consequently, for the circular velocity of galaxies, 4.3 implies that the velocity has a component that increases as $\sqrt{R}$ and another component that decreases as $1\sqrt{R}$. Overall, it shows a peak near the galaxy's radius, as depicted by the blue line in 2.1. However, observations using redshift measurements do not reveal significant variations in velocity along the galaxy. In other words, v remains constant, which, according to 2.2, implies that the mass must vary linearly with the radius. This discrepancy can be interpreted as evidence of invisible matter, commonly known as dark matter, which extends beyond the luminous disk. Many other phenomena are thought to be strongly influenced by the presence of dark matter. For example, in the case of gravitational lensing, the observed image is distorted because the light coming from distant galaxies reaches us after passing through regions of space with large masses, which gravitationally deflect photons thus distorting the images. Gravitational lensing, hypothesized by Einstein, provides an excellent method to estimate the masses crossed by light. However, even in this case, the mass calculated from the

observations is significantly larger than what is visibly observed. It is therefore believed that also in this case the discrepancy is due to the presence of dark matter. [11], [12] In particular, the existence of Massive Compact Halo Objects (MACHOs) is hypothesized, which refers to non-luminous, massive, and compact objects. Other hypotheses are referred to the cosmological context, particularly about the formation of galaxies. For instance, the Λ CDM (Lambda Cold Dark Matter) model says that in the early universe, there were clusters of cold dark matter that began to gravitationally collapse before baryonic matter (it is assumed that dark matter only interacts gravitationally), leading to spatial anisotropy that might explain the distribution of the cosmic microwave background radiation. By studying the cosmic microwave background radiation, some properties of dark matter have been understood, alongside the fact that it constitutes approximately 80% of the total matter content of the universe. The temperature anisotropies observed in the cosmic microwave background radiation are sensitive to various cosmological constants. Through precise analysis of data from COBE [13], WMAP [14], and PLANCK [15] satellite experiments, we calculated of the density parameters:

1. Visible baryonic matter: $\Omega_b \simeq 0.0484$
2. Dark Matter: $\Omega_c \simeq 0.258$
3. Total matter: $\Omega_m \simeq 0.308$
4. “Quintessence” (dark energy): $\Omega_\Delta \simeq 0.692$

where $\Omega_i = \rho_i/\rho_c$. In cosmology, the term "baryonic matter" is used to refer to normal atomic matter, including protons and neutrons, while excluding electrons (which are leptons) due to their negligible mass contribution ($\simeq 0.0005$ of the total). However, these observations do not provide direct information about the nature of dark matter (DM).

Non-visible baryonic matter may consist of astrophysical objects such as remnants of white dwarf stars, black holes, neutron stars, and giant planets like Jupiter. The majority of non-baryonic dark matter could be composed of weakly interacting particles, with a distinction between cold dark matter (non-relativistic) and hot dark matter (relativistic) based on the mass of the DM particle candidate (with a threshold at the mass of circa 1 keV) [16]. Cold dark matter candidates are commonly referred to as Weakly Interacting Massive Particles (WIMPs). Among the WIMP candidates, the neutralino stands out as the most favored candidate, being the lightest stable supersymmetric particle (LSP) with a mass around $(10^2 \div 10^3)$ GeV, more details in [17] and [18].

Direct searches for WIMPs involve measuring the recoil energy of a nucleus (few keV) after elastic scattering with a WIMP inside the detector. New-generation cryogenic calorimeters are employed to achieve the required low energy threshold, enabling the detection of the weak photonic signal generated by the ionization or excitation produced in the detector material by the recoiling nucleus. However, the challenge lies in the high background due to environmental radioactivity, making it crucial to distinguish the possible WIMP signal from background events. The DAMA/LIBRA [19] [20] experiment at the Gran Sasso Laboratory uses a clever strategy by exploiting the concept of a "WIMPs wind" surrounding our galaxy. There are variations in the WIMPs flux as the Earth moves around the Sun, with a maximum in June (when the revolution speed of the Earth adds to the speed of the solar system) and a minimum in December (when the two velocities have opposite directions). This temporal variation aids in discriminating the potential WIMP signal from background noise. However, subsequent similar experiments, notably ANAIS-112 [21] [22] and COSINE-100 [23], have led to results conflicting with those of DAMA/LIBRA, failing

to observe such modulation within the same energy range. Consequently, the discussion regarding the experimental confirmation of direct interaction with dark matter remains open [24].

We can summarize the possible DM candidates in 2.2

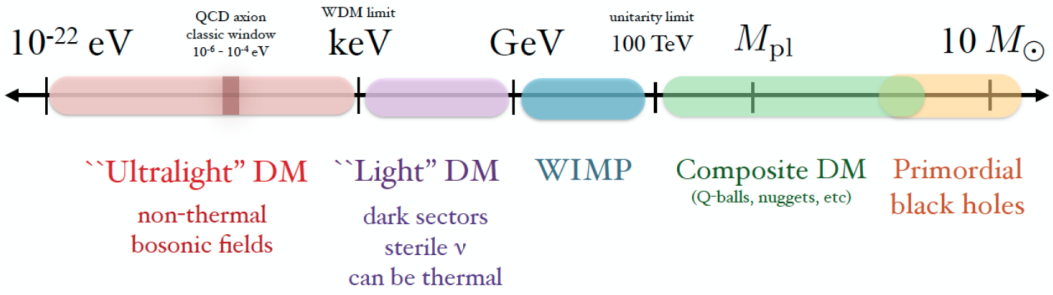

Figure 2.2: Picture from [25]. Schematic representation of possible DM candidates.

The direct search for dark matter is now one of the most promising areas of physics research, and several projects are pursuing this, with DarkSide-50 and DarkSide-20k being notable examples.
In this thesis, we will only focus on investigating and detecting WIMPs.

2.2 WIMPs and Dark Matter search

Within the standard model of particle physics, the neutrino is the only particle that fits the criteria of being stable, uncharged, and possessing mass, making it a potential candidate for dark matter. However, recent observations have shown that the neutrino's mass is too small to account for the required total mass. Additionally, the clumpy structure observed in the universe during its formation contradicts the relativistic nature of neutrinos.

To explain the observed large-scale structure of the universe, a dark matter particle produced in thermic equilibrium during the early stages would need to have a relatively high mass. Therefore, a Weakly Interacting Massive Particle emerges as an important candidate for resolving the dark matter problem. While a WIMP is widely discussed as a candidate, it should be acknowledged that other potential solutions to the dark matter problem exist, such as axions, for example. However, for this thesis, our focus will be solely on WIMPs [26]. More details about the general status of dark matter searches are in [27] and [28]

As Supersymmetric WIMPs are Majorana particles we would expect annihilation between the two of them to occur. The regions of annihilation include the centers of galaxies and the cores of astronomical entities like the Sun and Earth with high density, where WIMPs are believed to have accumulated. The identification of annihilation products resulting from WIMPs is commonly referred to as indirect dark matter detection.

Annihilation can take place if the densities of particles and anti-particles are comparable. When annihilation occurs within a dense celestial body, the only detectable products are high-energy neutrinos. Extensive neutrino detectors such as SuperKamiokande [29] and IceCube [30] have conducted searches for such signals, but so far only limits on the flux of high-energy neutrinos have been found.

Numerous experiments, such as PAMELA and VERITAS [31], are dedicated to the indirect detection of neutrinos. However, in this thesis, we will focus on the direct detection of dark matter [26].

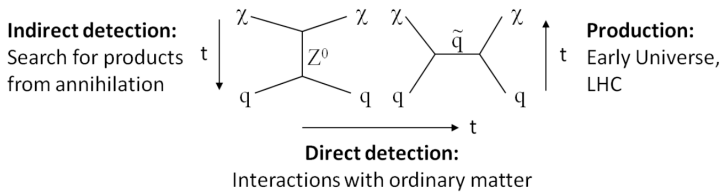

Figure 2.3: Feynmann diagram of the difference between direct and indirect detection for WIMPs. [26]

If WIMPs were generated during the early universe in thermal equilibrium or if they undergo annihilation processes with standard model particles, we expect they would also engage in direct interactions with ordinary matter. This arises from the similarity of Feynman diagrams describing these interactions. Considering that the escape velocity is approximately a few hundred km/s, it can be reasonably estimated that the maximum energy transferred from a WIMP to an initially stationary electron would be in the range of electronvolts (eV). We expect the energy transfer to an atomic nucleus to be in the order of tens of keV. Hence, direct detection experiments primarily focus on detecting nuclear recoils induced by WIMP [26].

In the range of momentum transfer relevant to WIMP-nucleus scattering, it has been observed that the scattering amplitudes of all nucleons within a nucleus exhibit constructive interference, resulting in a scattering amplitude proportional to the number of nucleons A. Since the probability of scattering is proportional to the square of the amplitude, it follows that the cross-section is proportional to A^2, favoring nuclei with higher mass. This relationship holds for nuclei of medium size. However, for very heavy nuclei and at higher momentum transfers coherence is lost, and the effective cross-section increases at a slower rate with A.

It is worth noting that depending on the specific theoretical framework, the WIMP may primarily couple to the spin of nucleons. In this case, coherence becomes a disadvantage as scattering amplitudes of nucleons with opposite spins cancel each other out. Consequently, for spin-dependent interactions, nuclei with unpaired nucleons and high spin factors are required as target nuclei.

Minimal Supersymmetric models are among the commonly studied extensions of the standard model of particle physics. However, even within this specific model, the predicted WIMP-nucleon interaction cross-section may vary by many orders of magnitude. Typical values for the spin-independent cross-section are between 10^{-10} pb and 10^{-12} pb between 10 GeV and 10 TeV. Such small cross-sections need large target masses and long measurement times [26].

The fact that WIMPs rarely interact with ordinary matter is the biggest issue with dark matter detection, thus it is fundamental to remove or minimize the background or other signals that can be confused with WIMPs. Most false positive signals can arise from interactions with cosmic rays, which is why underground laboratories are often used. By doing so, the flux of cosmic rays reaching the experiment site is significantly reduced.

Additionally, further shielding materials are used, avoiding those that could decay and constitute an additional source of background. Muon veto detectors are also used to identify (and therefore reject) any muons that are not shielded by the aforementioned systems.

Lastly, it is necessary to find a way to distinguish or discriminate the background from other signals. This can be achieved by exploiting three phenomena.

1. As explained earlier, the WIMP signal interacts with a larger cross-section of atomic nuclei. This results in the scintillation of the incident particle upon interaction with the target material (such as noble gases like xenon or argon), instantly emitting scintillation photons that are characteristic of the target.

2. Near the location of the interaction, electrons are generated through ionization. These electrons can then undergo positional changes or trigger cascades to produce additional electrons if the detector is immersed in an electric field. Many other processes may contribute to the formation of electrons in the detector, such as spontaneous grid emission or delayed emissions. Therefore, it is necessary to understand and distinguish these processes.

3. The lattice of the impacted target material can vibrate, generating heat that can be detected.

Typically, experiments employ two out of these three techniques to reject certain events (e.g., DarkSide uses the first two). However, by studying each signal individually, through pulse shape discrimination, sometimes even a single technique can be sufficient (e.g., DEAP/CLEAN [32] and [33]).

2.2.1 Experiments looking for dark matter

Noble gasses are often used in this type of experiment as scintillation materials as they are easy to isolate, do not undergo chemical reactions, and generally exhibit efficient scintillation when impacted by particles within a specific energy range (which depends on the chosen material). Additionally, due to their inert nature, ionization electrons have a long lifetime and can drift over long distances when immersed in an electric field. Thus, noble gases are commonly employed to build time projection chambers, where by measuring the time between the scintillation event and when the drifted ionization electrons reach a detector, the position along the z-axis of the interaction can be reconstructed.

The choice of which noble gas to use in this type of detector is crucial. Generally, it is preferable to use elements with higher atomic mass, as this would increase the cross-section and thus the probability of interaction with WIMPs. However, to avoid additional background, it is important to use non-radioactive elements or those without radioactive isotopes. This narrows the choice down to xenon and argon. Xenon has been the most widely used thus far, having the advantage of a larger atomic mass A. On the other hand, argon is significantly less expensive (2 dollars per kilogram compared to 1.5 dollars per gram of xenon [34] and exhibits a bigger scintillation yield [35] and [36]. However, argon does contain the radioactive isotope ^{39}Ar, which has a small concentration in atmospheric argon of (10^{-16}). Nevertheless, given the low interaction rate of WIMPs with matter, it would still contribute to an excessive background. One of the goals of the Aria project is precisely the removal of this isotope to make argon more competitive. Furthermore, Argon allows a better pulse shape discrimination between nuclear and electron recoil compared to Xenon [7]. The main (ongoing, concluded, or under construction) experiments for direct WIMPs-matter interactions are the following

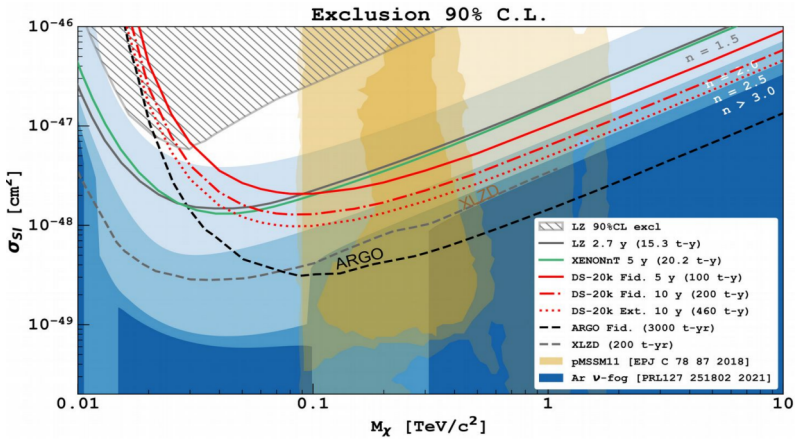

Figure 2.4: Mean exclusion sensitivity as a function of the mass of the WIMP. The blue region is delimited from above by the "coherent neutrino-nucleus scattering floor," which represents the ultimate experimental limit for any given exposure. This limit is caused by the uncertainty of the neutrino background. [5]

1. Bubble chambers. PICO, PICASSO, COUPP
2. Cryogenic bolometers with ionization or scintillation detection. CDMS, SuperCDMS, CRESST, EDELWEISS
3. Cesium/sodium scintillation detectors. DAMA/LIBRA and KIMS
4. Point contact germanium detectors. MALBEK, CoGeNT
5. Liquid Xenon as scintillation material. XENONnT, XENON-100, LUX, ZEPLIN, XMASS, PandaX-II, XENON1T, PandaX-I, LZ
6. DarkSide-50, DarkSide-20k, DEAP-3600, WaRP, ArDM, MiniCLEAN

The list and references to all these experiments are in [5]. In Figure 2.4 which refers to [5], the sensitivity limits are depicted as a function of the assumed WIMP mass for the various mentioned experiments. The cross-section represents a lower limit, meaning that it represents the minimum cross-section for each experiment that still allows the identification of the interaction (90 % confidence level). The lower gray limit is determined by cosmological neutrinos (which are not shielded by the underground rocks of the laboratories). The analysis in [37] (and the more recent [38]) specifically highlights how these neutrinos can perfectly mimic WIMP interactions below a certain threshold, despite having significantly lower masses and thus represent a limit to the experiment and its exposure as they are physically indistinguishable from dark matter.

2.3 Dark Matter detection with noble gases

The noble gases, such as neon (Ne), argon (Ar), and xenon (Xe), are good candidates for WIMP (Weakly Interacting Massive Particles) searches due to their favorable properties as liquid-phase target materials. Their boiling points, ranging from 27.1 K (Ne) to 165.0 K (Xe), and 87.3 K (Ar), make them more accessible for operation compared to detectors requiring temperatures at the order of mK. The advantage of Xe and Ar is that they can even be liquefied using liquid nitrogen. Additionally, these elements exhibit excellent

scintillation properties with high light yields and enable direct measurements of ionization signals produced by particle interactions. Consequently, liquid xenon (LXe) and liquid argon (LAr) are commonly employed in current and future experiments, making them the focus of this section [39].

Element	Xe	Ar
Boiling point	165.0 K	87.3 K
Liquid density	2.94 g/cm^3	1.40 g/cm^3
Price	high	low
Atomic number Z	54	18
Atomic mass	131.3	40.0
Scintillation wavelength	178 nm	128 nm
W-value energy	21.6 ev	24.4 ev
Ionization energy	15.6	23.6

Table 2.1: Main characteristic of liquid xenon and liquid argon for dark matter search [39]

Reference 2.1 provides an overview of some material properties. Cryogenic noble liquid detectors, particularly LXe and LAr, offer the advantage of being scalable to large setups, making them attractive for WIMP searches as they can reach ton-scale and beyond. Moreover, Ar is relatively cost-effective compared to Xe. However, it should be noted that while Xe is intrinsically clean in terms of radioactivity (absence of long-lived Xe isotopes, while radioactive contaminations such as ^{85}Kr can be eliminated through cryogenic distillation), natural argon contains radioactive ^{39}Ar at the level of 1 Bq/kg, leading to background and pile-up challenges. Another distinction between the two gases lies in the wavelength of their scintillation light: LXe emits light at 178 nm, a wavelength for which the PMTs' window is transparent, while LAr-based detectors require wavelength shifters, such as TPB (tetraphenyl butadiene), to detect the light.

Scintillation in liquid noble gases is generated as follows [40]:

1. Upon excitation, the atoms rapidly form weakly bound excited dimers, known as excimers [41], which undergo radiative de-excitation, thereby emitting ultraviolet photons [42].

$$\mathrm{Xe}^+ + \mathrm{Xe} \rightarrow \mathrm{Xe_2}^* \tag{2.4}$$

$$\mathrm{Xe_2}^* \rightarrow 2\mathrm{Xe} + \gamma \tag{2.5}$$

2. Additionally, the ionized atoms form ionized dimers, which subsequently recombine with electrons. After relaxation via non-radiative processes, the de-excitation sequence results in the release of an ultraviolet photon.

$$\mathrm{Xe}^+ + \mathrm{Xe} \rightarrow \mathrm{Xe_2}^+ \tag{2.6}$$

$$\mathrm{Xe_2}^+ + e^- \rightarrow \mathrm{Xe}^{**} + \mathrm{Xe} \tag{2.7}$$

$$\mathrm{Xe}^{**} \rightarrow \mathrm{Xe}^* + \mathrm{heat} \tag{2.8}$$

$$\mathrm{Xe}^* \rightarrow +\mathrm{Xe} \rightarrow \mathrm{Xe_2}^* \tag{2.9}$$

$$\mathrm{Xe_2}^* \rightarrow 2\mathrm{Xe} + \gamma \tag{2.10}$$

This is true for both Ar and Xe. Argon scintillation is described more in detail in the next chapters about DarkSide.

Regarding WIMP-nucleon scattering interactions, the expected nuclear recoil energy spectra exhibit featureless exponential behavior, and the interaction rate is expected to scale with the atomic mass A squared (A^2). Consequently, the much heavier Xe is preferred due to its higher A value. However, the larger nucleus also leads to a loss of coherence for large momentum transfers, resulting in a form factor suppression of the rate at higher nuclear recoil energy. Therefore, LXe requires a low detector threshold to solve this issue. In contrast, LAr possesses an overall smaller interaction rate. [39]

If Weakly Interacting Massive Particles (WIMPs) do exist, their interactions are expected to be extremely difficult to detect compared to the backgrounds arising from natural radioactivity and cosmic ray-induced events. To mitigate these backgrounds, experiments are conducted in deep underground laboratories, protected by several kilometers of rocks. Additionally, massive shields made of carefully selected radiopure materials are used to counter environmental radioactivity. Among the significant bothers are neutrons, which can generate nuclear recoils similar to those expected from WIMPs, making them indistinguishable if they interact only once. However, some of these interactions may be discarded, as neutrons often interact with the scintillation inside the detector multiple times or may likely interact with argon in the outer part of the TPC. Therefore, in the search for interactions with WIMPs, only the argon in the central region of the TPC is considered (fiducial volume, as opposed to the active volume contained within the detector). In dark matter experiments, gamma and beta backgrounds, which generate electronic recoils, constitute the most prevalent sources of nuisance. However, electronic recoils have different energy loss rates (dE/dx) compared to nuclear recoils, thus we can exploit the differences in their signals for discrimination of the background with respect to the signal. For instance, in liquid argon (LAr), the pulse shape of the scintillation signal provides valuable insights into the interaction taking place. The excimers responsible for light emission have distinct decay times for their singlet and triplet states, allowing for the rejection of electronic recoils. Nevertheless, to meet the challenge of the significant background from ^{39}Ar, even higher rejection rates are necessary. Simultaneously measuring the charge and light signals for each event offers an additional method to distinguish between electronic recoil backgrounds and nuclear recoil signals. This approach exploits different dE/dx values, producing a unique charge/light ratio. In liquid xenon (LXe), the discrimination range is between $5 \cdot 10^{-3}$ and $1 \cdot 10^{-4}$ at a 50% nuclear recoil acceptance rate. While this technique is also used in LAr, its performance is not as robust as pulse shape discrimination alone, and, by itself, may not be enough to reduce the ^{39}Ar background to the required low levels. Therefore, a combination of multiple techniques is employed to achieve severe background reduction in dark matter experiments [39]. Detectors using noble gases in the liquid phase are either single-phase or double-phase.

Single-phase detectors present a straightforward concept, where a considerable volume of a noble gas in the liquid phase is observed by multiple light sensors, usually, photomultiplier tubes (PMTs), to lower the detection threshold (2.5, on the left). Since the scintillation light signals are relatively short (a few μs), single-phase detectors can handle relatively high event rates without significant pile-up issues. The chosen spherical geometry maximizes self-shielding benefits. The arrangement of PMTs covering a complete solid angle allows for rough event reconstruction, with a resolution typically in the range of several centimeters.

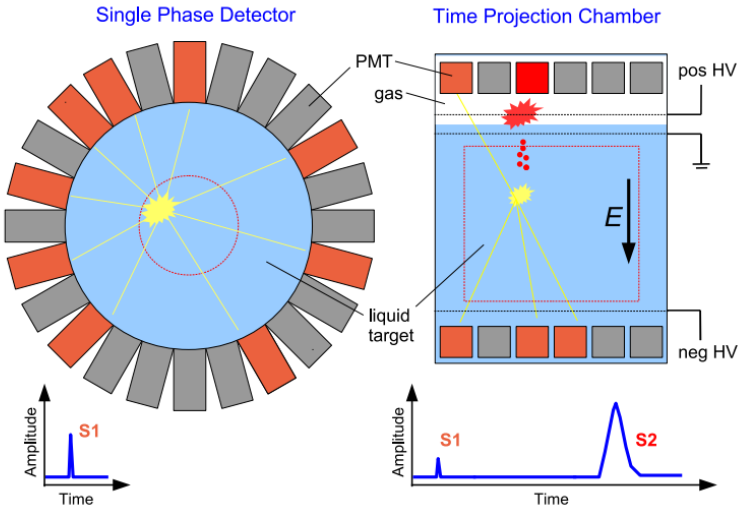

Figure 2.5: From [39], a schematic representation of single-phase (left) and dual-phase (right) liquid noble gasses detectors.

However, this reconstruction accuracy relies on the number of detected photons and weakens near the threshold. As single-phase detectors only detect light, background discrimination using the charge/light ratio is not possible. Therefore, these experiments rely on pulse shape discrimination. Consequently, most experiments use only the innermost region of the detector as the WIMP target, with the outer part (comprising up to 60% of the mass) serving as a background shield and veto [39].

In contrast, double-phase detectors, or Time Projection Chambers (TPCs), offer significantly improved 3-dimensional reconstruction, having z-resolutions below 1 mm and a xy-resolution of approximately at the order of mm (depending on the experiment). This is achieved by simultaneously measuring the scintillation light and the ionization charge signal. When a particle interacts, scintillation occurs, and ionization electrons are emitted, moving away from the interaction due to the effect of a moderate electric field (drift field at the order of 0.1 kV/cm). The drifting electrons reach the top of the cylindrical detector, where they are extracted into the gas phase above the liquid, generating a secondary light signal (S2) proportional to the charge. The light pattern on the top PMT array provides information on the location on plane x-y, while the time difference between the light (S1) and charge (S2) signals determines z. The excellent detection capabilities enable powerful background rejection through fiducialization and identification of events of multiple scattering, supported by charge/light discrimination (and pulse shape discrimination for LAr detectors). However, the optical coverage with photosensors in TPCs is typically smaller than that of single-phase detectors, potentially leading to a higher threshold. Additionally, TPCs represent a technical challenge as they need a high voltage system [39].

2.3.1 Liquid Xenon

Xenon, as a detection medium, has several advantageous characteristics [43]. Assuming an averaged W-value of 15.6 eV for both scintillation and ionization, xenon exhibits high scintillation yields, reaching approximately 65 photons per keV for gamma rays with energies around 100 keV with no field [44] and [45]. Even for nuclear recoils, the yields remain at about 10% of that level, even at energies below 10 keV. Remarkably, energy resolutions

better than 1% (σ/E) have been achieved at MeV scales, and spatial resolutions in the millimeter range can be achieved.

While liquid xenon may naturally contain radioactive isotopes like ^{37}Ar, ^{85}Kr, or ^{222}Rn,

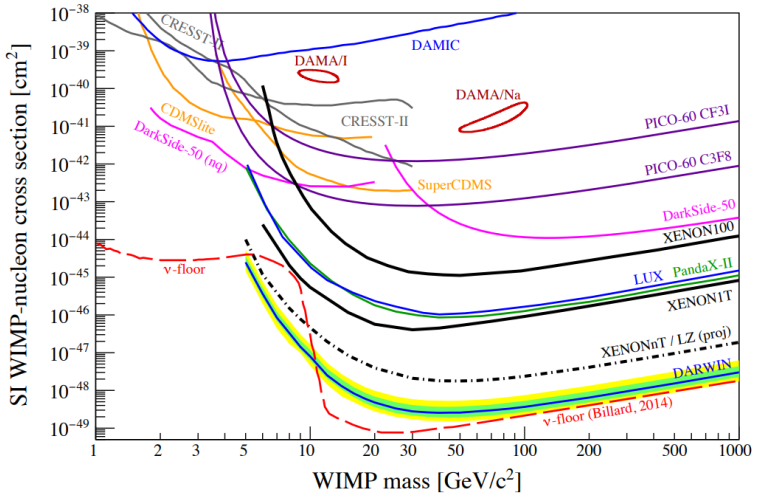

Figure 2.6: Picture from [46] showing 90% exclusion limits (solid lines) and projected sensitivities (dashed) of different dark matter experiments exploiting liquid noble gases.

purification processes to very high levels have been successfully achieved in dark matter and neutrinoless double-beta decay experiments. Xenon has a high charge number, mass number, and density, thus enabling shielding against backgrounds of gammas, which often undergo multiple scatterings, particularly in the external part of the fiducial volume [43]. Xenon has isotopes with an odd number of neutrons which fulfill the conditions for r spin-dependent neutron coupling. Other isotopes can be used looking for neutrinoless double-beta decay [47] and double electron capture research. Lastly, the mass of the xenon nucleus makes it ideal for detecting WIMPs with mass bigger than 10 GeV/c^2 [43]. More details about the xenon experiments are in [50] and [43] The most important experiments using liquid xenon looking for WIMPs were Xenon1T, Xenon100, and now XENONnT [43].

The XENON1T instrument is composed of around 3.3 tons of liquid xenon stored within a vacuum-insulated cryostat consisting of a double vessel built using low-radioactivity stainless steel. The inner cryostat's dimensions are specifically designed to accommodate the XENON1T Time Projection Chamber (TPC). The sensitive target of XENON1T comprehends about 2 tonnes of LXe confined within a TPC with a diameter and height of about 1 meter. The detection of scintillation signals is made by 121 PMTs in the lower part and 127 in the upper one. To maintain a uniform electric field, 74 copper rings are placed for field shaping. The main sources of background include electronic recoils within the detector materials and nuclear recoils from radiogenic and cosmogenic neutrons. [48], [46]. To reduce NR, the XENON1T detector is surrounded by a veto system, made to identify the interaction and the products of the interactions of the neutrons in the system, which can contribute to background events. The Muon Veto (a large stainless steel tank filled with ultrapure water) detects the Cherenkov light emitted by particles crossing the water. The light is detected by 84 PMTs with 8 cm diameter. The rest of the neutron background caused by muons in XENON1T is negligible, measuring < 0.01 events per year in a 1 t fiducial mass.

Currently, the XENONnT experiment [49] is under construction, using 5.9 tons of ar-

gon (4 tons fiducial) for the detection of WIMPs. The system is analogous to that of previous Xenon experiments. The cross-section is expected to be $1.4 \cdot 10^{48}\text{cm}^2$ for a WIMP with a mass of 50 GeV/c^2 at a 90% confidence level, considering a detection period of 20 years and a recoil energy range of 4 to 50 keV for nuclear recoils, we expect a background rate of $(2.2 \pm 0.5) \cdot 10^3$ (keV t y)$^{-1}$ [46] [49].

2.3.2 Liquid Argon

Liquid argon offers several advantages as a detection medium due to its abundance in Earth's atmosphere and the fact that it is easy to purify by removing electronegative impurities. These features make it a more cost-effective option compared to other noble liquids, thus making the construction of large detectors more reasonable. In natural argon, the most abundant component is the stable isotope ^{40}Ar, generated through the electron capture of ^{40}K. The production rate of ^{40}Ar is directly proportional to the number of ^{40}K atoms present [40].

$$^{40}\text{K} \rightarrow {}^{40}\text{Ar} + e^- \tag{2.11}$$

The majority of ^{40}Ar production takes place underground and later it leaks into the atmosphere. The natural abundance of ^{40}Ar in underground argon makes it a suitable choice for detectors, particularly in the search for dark matter and other rare events.

The main concern regarding the use of argon lies in the presence of the radioactive isotopes ^{39}Ar, ^{37}Ar, and ^{42}Ar. As discussed in the introduction 1 about the issue of ^{39}Ar, significant reduction can be achieved by extracting argon from underground locations and potentially further purifying it through distillation using the Seruci-1 column of the Aria project.
On the other hand, ^{37}Ar is produced in the atmosphere when neutrons interact with argon and undergo electron capture decay with a half-life of 35 days. Given that underground experiments are strongly shielded from cosmic rays, it is expected that after several months, this isotope will have completely decayed [51].
As for ^{42}Ar, it has a much longer half-life of approximately 33 years, but its activity is very low, around 92 μBq/kg. However, this isotope contributes to the background, which must be taken into account during experiments [52].

Regarding the scintillation of argon, the same formulas and mechanisms shown in 2.3 are still valid.
In liquid argon, the wavelength of the ultraviolet photon is 128 nm. In both channels of excimer formation (Ar_2^*), the lowest excited level undergoes deexcitation to the ground state emitting a gamma, as other decay channels are forbidden due to a large energy gap. Experimental measurements have shown that about $4 \cdot 10^4$ scintillation photons are produced per 1 MeV electron in liquid argon.
Ionizing radiation in noble liquids leads to the creation of excimers in either singlet or triplet states, which have different decay times. The lifetimes of the dimer (Ar_2^*) in its singlet and triplet states are approximately $\tau_s = 5.0$ ns and $\tau_l = 1.6$ μs. The type of particle causing the recoil does not change the decay times, but it significantly affects the ratio of singlet to triplet states. This ratio, defined as fast divided by slow component, exhibits different values for events produced by nuclear recoils (NRs) such as α-particles, neutrons, and WIMP interactions, if compared to events caused by γ-rays and electrons, which are referred called (ERs). For ERs, the ratio is around 0.3, while for NRs, it falls in the range of 1.3 to 3.3 [40], [53], and [54].
This difference in the intensity ratio of the two components works as a powerful tool for

distinguishing between NRs and ERs based on the shape of the scintillation time profile. This is the pulse shape discrimination (PSD), and for liquid argon, it enables the rejection of approximately $10^7 - 10^8$ ER events for every event misidentified as NR. PSD represents a significant advantage of liquid argon over other noble liquids. For instance, xenon can also use the pulse shape discrimination technique, but it is inherently less effective due to the closer values of the xenon singlet and triplet state lifetimes ($\tau_s = 4.3$ ns and $\tau_l = 22$ ns). The observed ionization-scintillation ratio also depends on whether the recoil is taking place with the nucleus or with an election. This and the 3D event position reconstruction can be used to distinguish between the two types of events, thereby improving discrimination [40].

2.4 DarkSide experiments

2.4.1 DarkSide-50

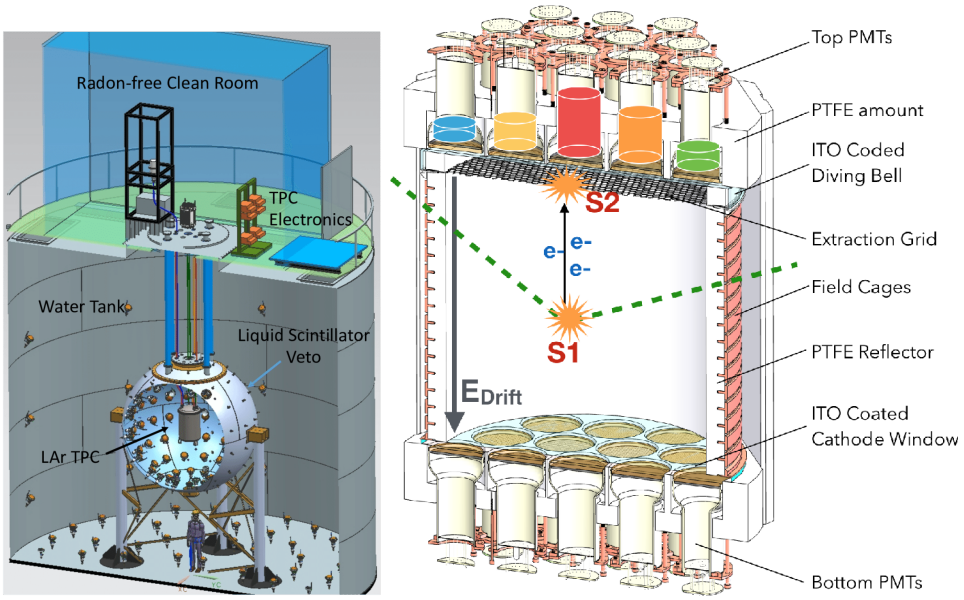

Figure 2.7: Pictures from [56], [7] and [55]. The general structure of DarkSide-50 is on the left and its time projection chamber (TPC) is on the right.

In recent years research has intensified on masses below 10 GeV and above 1 TeV, where the sensitivity is lower. [57] Given the lower probability of interaction, we need to increase the exposure (by increasing mass, exposure time, or both) and we need more effective signal-background discrimination as well. DarkSide-50 and DarkSide-20k have been designed to do so. These experiments use argon as the scintillation material, which, as mentioned in the previous section, exhibits excellent Pulse Shape Discrimination, allowing us to distinguish between nuclear and electron recoils. Furthermore, both are essentially a Time Projection Chamber (TPC) and so they allow for the reconstruction of the interaction position, mitigating edge effects. To compensate for the lower atomic number of argon compared to xenon, large quantities of argon are employed, particularly in the case of DarkSide-20k. A schematic representation of the experimental setup of DarkSide-50 is shown in 2.7 on the left.

DarkSide-50 consists of three nested detectors.

1. The outermost detector works as a veto system to identify coincident muons and

provides general shielding for the inner detectors. It is composed of 10^5 kg of water, has a diameter of 11 m, and is 10 m tall. Further technical details can be found in [58].

2. The intermediate detector also works as a veto system to avoid gamma-ray coincidences, as well as to mitigate radiogenic and cosmogenic neutrons and cosmic muons. It works as additional shielding for the Time Projection Chamber (TPC) located inside. This intermediate detector has a diameter of 4 m is made of stainless steel and is filled with 30 t of borated liquid scintillator [57]. For additional technical information, refer to [58].
   The presence of a specific isotope of boron, ^{10}B, is exploited in this detector. It has a high probability of capturing thermal neutrons (cross-section is $3.84 \cdot 10^{-25} m^2$ and neutron capture time is 2.2 μs). Following neutron capture, ^{10}B becomes ^{11}B and decays in ^{7}Li emitting an alpha particle and a 478 keV gamma photon. This emitted gamma photon is quenched to around 50 to 60 keV, which is then measured and identified by 110 PMTs [55].

3. Finally, the location where the main interaction should occur is the inner detector, namely the Time Projection Chamber (TPC), which is housed inside a stainless steel cryostat. The structure and its components are shown in 2.7, on the right. 38 PMTs surround the TPC, half above and half below. These PMTs are in liquid argon and have fused silica windows. This makes sure that the inner surfaces serve as anode and cathode, respectively, considering the upper and lower PMTs. Furthermore, the reflectors above and below the detector and the cylindrical wall are coated with a material that allows for shifting the wavelength of the scintillation signal emitted by the argon. This material is called TPC (tetraphenyl butadiene) and it converts the ultraviolet signal emitted by the argon (mostly at 128 nm) into visible light around 420 nm. The thickness of the TPC is not constant around the TPC; for further details, please refer to [57].

In 2.7, the schematic representation of the mechanism leading to the formation of signals, particularly S1 and S2, is shown. The S1 signal, as we will see, works to distinguish between an electron signal and a nuclear recoil signal, while the S2 signal is used to reconstruct the three-dimensional position of the interaction. The combination of these signals provides an additional veto, thereby rejecting background events. The scintillation mechanism is as follows:

An ionizing particle in liquid argon produces Ar^+, e^- (electron-hole couple), and Ar*, that is an excited state of argon, whose ratio is 5 to 1 in favor of Ar^+ according to [59] and [60]. The process described in [61] explains how collisions between Ar* form Ar_2^* via a self-trapping process in 10 ps. Moreover Ar^+ will form Ar_2^* in circa 100 ps via electron recombination and other processes. Ar_2^* might be in a singlet or triplet state [61] and in both cases they decay as follows

$$Ar_2^* \rightarrow 2Ar + \gamma \tag{2.12}$$

The emitted photon has a wavelength of 128 nm and a Gaussian distribution with an FWHM of 6 nm. The time dependence of the scintillation depends on whether we are considering a singlet or triplet excited state. In the first case (fast component) different measures show how the decay rate is between 1 ns and 8 ns. In the second one, the slow component has a decay rate between 1000 ns and 1700 ns. These data are in [62], [63], [64], and [66]; more details will be discussed in the chapter about the DarkSide50 waveform

study and a single electron.

These ionizations cause a fundamentally instantaneous scintillation signal, denoted as S1, which is measured by the PMTs. The amount of signal measured by the different PMTs, allows us to reconstruct the position of the interaction on the plane of the cylinder. Other non-recombined electrons are then drifted upward by an electric field until they reach a layer of gaseous argon situated between the liquid argon and the anode (as illustrated in 2.7). Under the influence of the electric field, these electrons acquire enough energy to produce a secondary signal of electroluminescence, referred to as S2, which is also measured by the same PMTs used for S1. The time difference between S1 and S2 enables us to determine the position along the z-axis of the TPC where the interaction occurred. Consequently, we obtain the 3D position of the interaction. It is worth noting that additional delayed signals, referred to as S3, S4, and so on, have sometimes been measured. These signals are typically much smaller in magnitude compared to S2. S3, in particular, is always observed at a fixed time difference from S2, corresponding to a distance equal to the length of the TPC (anode-cathode distance). It is believed to originate from electrons emitted by the cathode when it is struck by ultraviolet radiation.

The ratio between the number of singlet and triplet states is 0.3 for minimum ionizing particles: according to [65] this ratio strongly depends on the type of particle the interaction with liquid argon (while the decay rates are not affected). It is around 1.3 for alpha particles and it rises to 3 for nuclear recoils. This is important as it enables effective pulse shape discrimination. Indeed, by studying the primary signal S1 measured by the PMTs following argon scintillation, if a greater contribution from the fast component of scintillation is identified, then we are dealing with a nuclear recoil event; if not, it will indicate an electron recoil event.

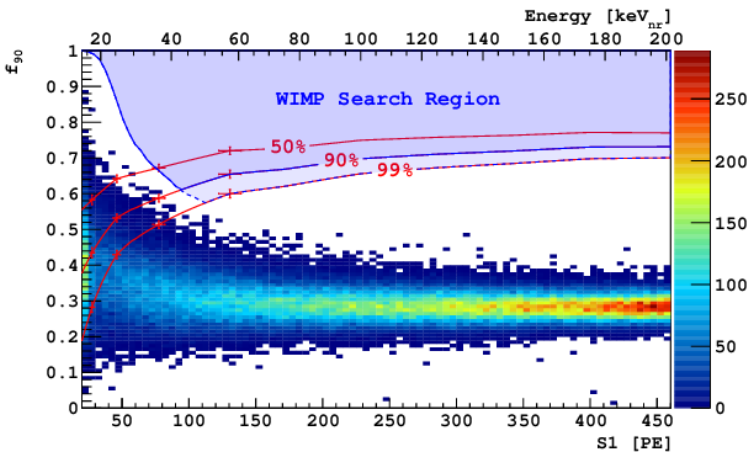

Figure 2.8: Factor f_{90} (defined in the text) as a function of the signal S1 expressed in photo-electrons and energy. Data are from DarkSide-50 [67] while the acceptance curve for nuclear recoil (in red) is from SCENE [68].

It is possible to define a factor f_{90} as the ratio between the S1 signal in the first 90 ns and the total signal (taken as the integral up to 7000 ns). This factor is expected to be around 0.3 for electron recoils (beta or gamma interactions) and 0.7 for nuclear recoils. As evident from the graph in 2.8, the majority of electron recoil events exhibit an S1 signal of around 450 photoelectrons and an f_{90} value of 0.3. On the other hand, nuclear recoil events are found at higher values of f_{90} in the upper region. The red curves represent the

acceptance of events as nuclear recoils measured by SCENE [68], where it can be seen that even with 99% acceptance, we are still far from the electron recoil background. Furthermore, discrimination does not solely depend on f_{90} but also on the ratio between S1 and S2 in general. This occurs because beta and gamma events generate electron-ion pairs with lower density and thus less recombination, resulting in a higher number of free electrons and a higher S2/S1 ratio compared to nuclear recoils.

2.4.2 Particle detection in DarkSide-50 and activities in detector materials

The processes involved in shielding the detector from unwanted interactions are summarized as follows.

1. In the case of alpha particles, external alphas are effectively screened out as they would be easily absorbed by external shielding. The main sources of concern are ^{210}Po, ^{222}Rn, and their decay products, which can be introduced during the construction phase or through the recirculation of liquid argon [57]. Some of their decays (or the daughters) exhibit similar f_{90} values to those of nuclear recoils. Therefore, we need to distinguish them, and they may contribute to the background only in certain cases. For more details, refer to ([7], Chapter 3A).

2. Is difficult to distinguish between nuclear recoil events and interactions of neutrons in the detector. So these are some of the most challenging interactions that constitute the background. We can start identifying multiple S2 signals, since neutrons are likely to interact multiple times with the detector material, thus causing multiple signals. Similarly, they probably interact within the liquid argon used for the veto (the intermediate layer). Furthermore, since neutrons have a small interaction length, we can exclude many interactions with neutrons by reconstructing the position of the interaction and rejecting events near the edges. [57] highlights that the most challenging neutrons to eliminate, which contribute to the background, are those resulting from (α,n) interactions originating from the ceramic plates that hold the dynodes and the borosilicate glass.

3. As mentioned earlier, the two external veto systems adjacent to the TPC enable the discrimination and elimination of external beta and gamma particles. Therefore, the main source of concern is located within the argon itself, specifically its isotope ^{39}Ar. This isotope is produced through the interaction between cosmic rays and the argon in the atmosphere. In the atmosphere, it has an activity of 1 Bq/kg, which is significantly reduced to 0.73 mBq/kg [69] using underground argon (due to shielding from cosmic rays). Hence the importance of the Urania project [57], which involves the extraction, purification from chemical contaminants, and subsequent transportation of underground argon. In addition to that, there is the activity of ^{85}Kr at 1.9 mBq/kg found in underground argon. Both ^{39}Ar and ^{85}Kr undergo beta decay, resulting in a detectable signal.

Therefore, overall, the internal sources, which are components of the detector, contribute significantly to the background. 2.9 displays the spectrum of the components constituting the background, where ^{39}Ar is already significantly suppressed by using UAr. Otherwise, this component would be 1400 times larger and dominant compared to the others. In addition to ^{39}Ar, other sources of background are found in the PMTs, the cryostat, or the fused silica [57].

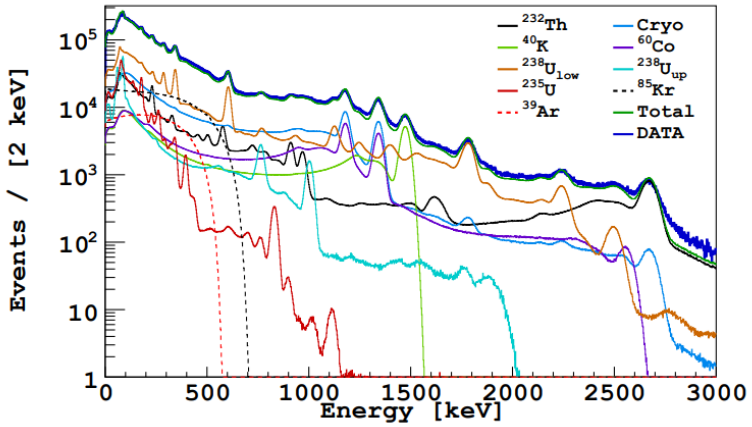

Figure 2.9: DarkSide-50 expected background, more details in text. [57]

2.4.3 DarkSide-20k and beyond

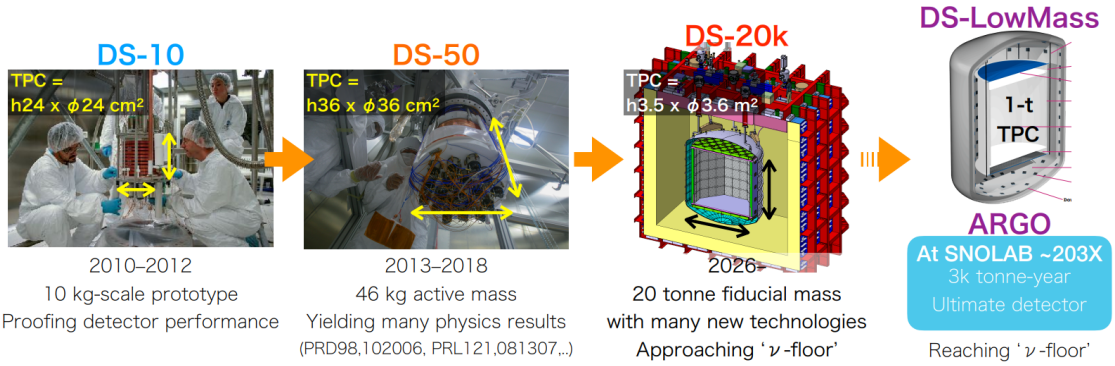

Figure 2.10: Brief history of the DarkSide projects. In the pictures are indicated the dimensions of the detectors. [70]

After the excellent results achieved by DarkSide-50, it was decided to expand the project to the ambitious DarkSide-20k experiment. This new attempt keeps the overall structure, parameters, and functioning of its predecessor but enhances its effectiveness by using a significantly larger volume of argon (20 tons compared to the previous 50 kg), thereby increasing the exposure as well. DarkSide-20k aims to ensure a minimum operational period of 5 years while maintaining a background level of fewer than 0.1 events in the WIMP search region [5].

DarkSide-20k is being constructed in Hall-C of the Gran Sasso Underground Laboratory at a depth of 3.8 km. It will consist of the following components [70]

1. An octagonal TPC, measuring 3.5 m in height and width, filled internally with 50 tons of active UAr (Ultra-Pure Argon) and 20 tons of fiducial UAr.

2. A cryogenic system designed to maintain the argon in a liquid state.

3. Surrounding the TPC, there will be a 40 cm thick veto region containing 35 tons of UAr. This veto region will be equipped with multiple Silicon PhotoMultipliers to analyze the veto signals. Further details can be found in reference [71]

4. Gd-doped acrylic panels will be used for neutron background veto.

5. An external veto system will be implemented, consisting of a PROTODune-like cryostat [72] containing 700 tons of AAr (Atmospheric Argon).

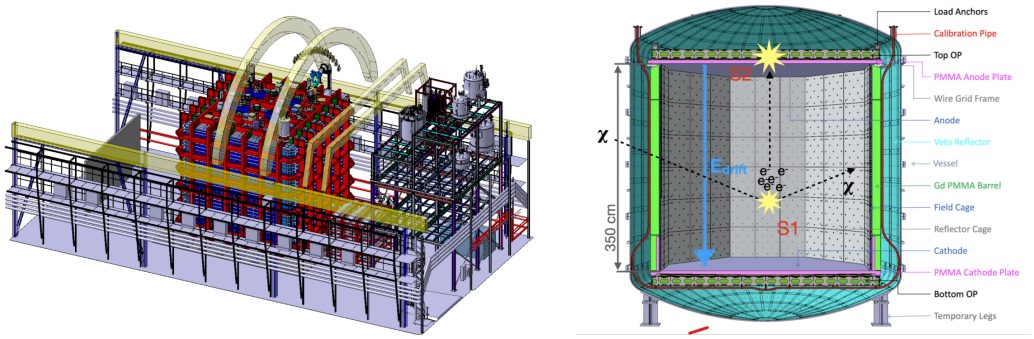

Figure 2.11: General structure of DarkSide-20k on the left and its time projection chamber on the right. [73]

More details and description of the structure of DarkSide-20k can be found in [74] Furthermore, it should be emphasized that the introduction of Gd-doped acrylic was chosen In order to capture neutrons efficiently so that photons can be emitted with a total energy of 8 MeV. This enables an additional veto on neutron interactions. The overall structure of DarkSide-20k can be seen on the left in 2.11, while on the right, we have the TPC alone. The TPC is surrounded by PMMA, where the violet regions represent pure PMMA and the green regions are acrylics doped with Gd. TPB is used for the same reason as DarkSide-50, along with ESR (Enhanced Specular Reflector) films as reflectors [70]. Further technical details are in [5].

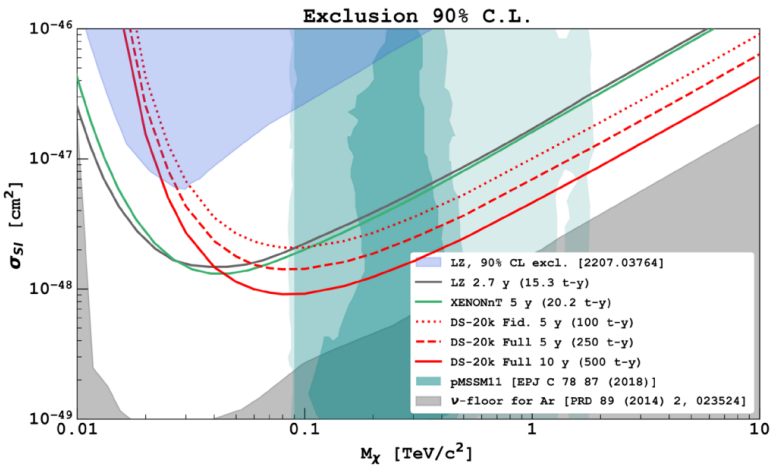

Figure 2.12: The graph illustrates, at a 90% confidence level, the spin-independent WIMP-nucleon interaction cross section as a function of the hypothesized WIMP mass. It compares three different scenarios for DarkSide-20k with competing experiments. The different colored areas indicate regions in parameter space where WIMPs are likely to stay according to specific models. [75]

The operation and underlying concepts of the measurements are derived from DarkSide-50, thus referring to the previous chapter for these details.

The projected sensitivity of DarkSide-20k is shown in the graph in 2.12, which was obtained using the profile likelihood ratio. The improved veto and pulse shape discrimination, compared to DarkSide-50, allow for a significant reduction in background[75]. The gray shaded area represents the neutrino floor, while the colored regions correspond to parameter space where WIMPs candidates are according to various models. Further details about these models can be found in [75]. Various scenarios have been considered, including 5 or 10 years of exposure and analysis of either the fiducial volume or the entire volume. It is worth noting that above approximately 100 GeV, all the cases are expected to provide results with lower limits than the competitor's experiments, specifically Xenon-based experiments. Overall, we expect less than 0.1 events of background in 5 years, while from neutrinos we expect approximately 1.7 events [75].

In summary, DarkSide-20k has been designed to mitigate the background contributions from the following components:

1. Nuclear recoil from neutrinos: Only atmospheric or supernova neutrinos can have energies high enough to escape Pulse Shape Discrimination, in the sense that they undergo coherent scattering with nuclei and produce a signal in the region of interest of dark matter. Other neutrinos, while having limited interaction capabilities, are indistinguishable from WIMPs and therefore contribute a small, but unavoidable, background (less than 2 events in 5 years, as mentioned earlier).

2. Nuclear recoil from neutrons: The presence of two external veto systems allows for a reduction in the expected number of neutron events to below 0.1 events in 100 ton-years of exposure. It is crucial to shield the detector from external sources and use materials that do not emit neutrons. The vessel is considered a potential source of neutrons, so it is essential to employ radiopure materials [5].

3. Regarding electron recoil, the effective reduction is achieved through data cuts (e.g., excluding interactions occurring too close to the detector edges) and pulse shape discrimination. The main concern remains the presence of ^{39}Ar, as mentioned earlier. However, it is believed that a reduction in concentration on the order of 10^{-19} relative to ^{40}Ar would sufficiently mitigate the background contribution from this isotope [5]. An even better reduction could be achieved by distilling underground argon with Aria, but it would require an impractical amount of time to produce as we will discuss in the next chapters.

Element	Maximum concentration allowed
CH_4	0.25 ppm
CO	0.1 ppm
CO_2	0.1 ppm
H_2	1 ppm
H_2O	1 ppm
N_2	1 ppm
O_2	1 ppm

Table 2.2: Maxiumum concentration allowed for the getter of DarkSide-20k.[5]

The removal of chemical impurities within the argon will be crucial for obtaining reliable data, particularly to avoid quenching effects between these impurities and argon. Further

details on the study of nitrogen effects on DarkSide-50 will be discussed in a dedicated chapter. The required purities for the getter of DarkSide-20k are specified in [5], and we will achieve them through the combined efforts of the Urania and Aria projects (Aria is believed to be particularly useful in resolving the challenging nitrogen issue).

The removal of the ^{39}Ar isotope from argon through cryogenic distillation, although not reachable by Aria in a reasonable amount of time for Darkside-20k (at least not with the currently under-construction Seruci-1 distillation column), is, however, possible to be produced for the DarkSide-LowMass project, which only requires one tonne of purified argon (Table7.23).

DarkSide Low-Mass is a project that is currently not yet approved and its effectiveness is still under discussion. Its goal is to investigate WIMPs with a mass below 10 GeV, hence the term "low-mass". The general structure would be similar to other DarkSide experiments; however, it would have a significantly lower mass of argon, leading to further reduction of the background due to the suppression of the ^{39}Ar isotope. This reduction may enable DarkSide Low-Mass to reach the solar-neutrino fog for GeV scale masses (more details about how this is possible are in [76]). However, some issues still need to be solved, particularly regarding spurious electrons, which could pose a significant and troublesome background.

2.4.4 Requirements for DarkSide-20k and getter.

In DarkSide-20k, the Liquid Argon Time Projection Chamber (LAr TPC) works as the central element and primary dark matter detector in the experiment. To meet the demanding physics requirements, the LAr TPC must fulfill the following specifications (all from [5]) :

1. It should offer a target mass of 20 tons after applying fiducial volume cuts.
2. Only radio-pure materials with well-documented performance in LAr, such as OFHC copper, acrylic, and low-radioactivity stainless steel should be used.
3. The LAr TPC must produce S1 light yield at least equivalent to 10 photoelectrons per keV. It is possible by employing large-area, dense arrays of photosensors.
4. It should allow stable application of a cathode voltage of -52 kV, essential for generating the drift field.
5. The TPC should enable tilt adjustment to level the anode plane.
6. Uniform drift, extraction, and electroluminescence fields, as well as gas pocket thickness uniformity. They can ensure the high resolution of S2 signals.
7. The x-y position resolution should be on the order of 10 mm or better than.
8. It should be designed to accommodate differential thermal contraction, even under thermal gradients during the cooling process.
9. Rapid deployment of ^{83m}Kr throughout the active TPC volume should be facilitated for calibration.
10. Efficient circulation of LAr should be possible to maintain purity.

One of the main topics of this thesis is going to be purification. In 2.2, the required purity level of DarkSide's getter is discussed, which works for the purpose mentioned earlier. A pump continuously recirculates the liquid argon through the getter, ensuring the system remains purified, i.e., maintaining the argon as pure as possible. However, for its proper functioning, acceptable starting concentrations are necessary, as indicated in Table 2.2, to significantly decrease them to values in the order of ppb or ppt [5].
To maintain and enhance purity, argon is extracted from the cryostat in its gaseous phase using a recirculation pump. The gaseous argon (GAr) then undergoes purification steps, starting with its passage through a hot SAES getter [77], followed by a cold charcoal radon trap, which is cooled by the GAr itself. Before entering the cold trap, the incoming GAr is cooled using outlet nitrogen gas from a liquid argon (LAr) condenser, employing a heat exchanger to minimize the required cooling power. In this design, the temperature of the cold trap is proportional to the flow rate of the GAr. For a more comprehensive description of the argon circulation system in DarkSide-20k, refer to [5]. It is identical to that of DarkSide-50, with the only distinction being its capacity to handle a much higher gas flow rate, up to 1000 L/min, in the case of DarkSide-20k.
It is interesting to observe that the purification system, which is analogous to that of DarkSide-50, was temporarily deactivated for approximately 5 days during its run, resulting in the stoppage of the continuous and constant purification process during that timeframe. In the upcoming chapter, we will be studying the effects of this interruption. Indeed, it has been observed that during this period, there was a significant increase in the number of events recorded by the TPC, in particular of a specific type of event, namely those with only S2 signals (without S1) and with a signal lower than that corresponding to 4 electrons. These particular events are referred to as Single Electrons. Among these, one of the most plausible theories concerns the presence of impurities at higher concentrations due to the malfunctioning of the getter. To confirm or refute the correlation between single electrons and impurities, we will retrospectively attempt to measure the oxygen and nitrogen impurities concentration (the primary suspects) through other means, specifically by studying the electron lifetime and the nitrogen scintillation triplet lifetime. All the specific details will be discussed in the next chapter.

2.4.5 Single Electron events

In summary, the main types of signals encountered in DarkSide-50 are as follows where S1 represents a prompt scintillation signal, and S2 is a delayed signal due to ionization electrons:

1. No Signal Events where noise is triggering the detection of an event: they include low-charge signals occurring near the edge of the TPC.

2. S1-Only Events: These events exhibit an S1 signal but lack an S2 signal. They could be related to Wall effects or Cherenkov effects, for example.

3. Standard Scatter Events: These events involve both S1 and S2 signals, representing typical scatter interactions.

4. Gamma Multiple Scatter Events: Characterized by the presence of multiple signals (more than one S1 and S2), these events involve gamma interactions with multiple scattering.

5. Multi-S2 Events: Events with multiple scattering but only S2 signals present.

6. Rarer Multi-S2 Events: Events with multiple scattering, but only multiple S2 signals present. They may be caused by multi-scatters with low enough drift time or sub-threshold S1.

7. S2-Only Events: Events showing only an S2 signal, without an initial S1 signal, or when the S1 signal is too small to be detected.

8. Low-Charge S2 Events: Events characterized by the presence of an S2 signal at a low charge, which are hypothesized to be Single Electron (SE) events, potentially attributed to various spurious electron measurements.

Below 92 PE (4 electrons) the charge is considered low, as defined in other DarkSide-50 analyses [78]. In addition to experiments like DarkSide-50, which seek direct evidence of WIMPs by detecting signals of types S1 and S2, others prefer to analyze only the S2 signal in DM-electron and DM-nucleus interactions, involving both xenon and argon as target materials (details and references to such experiments can be found in [78] and [79]). Each of these experiments has shown a significant number of events with only a low-charge S2 signal, sometimes referred to as single electrons (SE). This number cannot be caused by radioactive background sources [40], and the origin of these events remains unclear. For example, in the context of the DarkSide-50 S2-only analysis, event selection criteria required the presence of at least 4 ionized electrons, limiting the sensitivity to WIMP masses above 1.8 GeV/c^2. Consequently, comprehending the origin and characteristics of these events becomes paramount in enhancing the sensitivity of low-mass WIMP searches [40]. In picture 2.13 is the categorization of the Single Electron Candidates, more details about them are in [78] and [40].

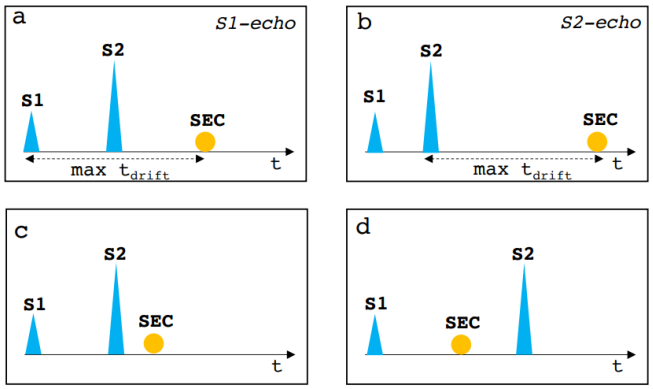

Figure 2.13: The categorization of events containing Single Electron Candidate signals in 3-pulse events is the following. Those signals found exactly after one maximum drift time following the S1 pulse are known as S1-echo. Single Electron candidates found exactly after one maximum drift time following the S2 pulse are referred to as S2-echo. SEC may be observed after both S1 and S2 pulses but before one maximum drift time or they might occur between S1 and S2. [40]

The temporal evolution of event rates for each distinct category is shown from the UAr filling date in 2015 in Figure 2.14. Except for SE and No Pulse event rates, the rates for the other categories exhibit relatively consistent behavior over the 900-day operational span, suggesting the stability of both the Time Projection Chamber (TPC) and cryogenic system. Temporal gaps in the data points are attributed to different experimental configurations like field runs and calibration source runs.

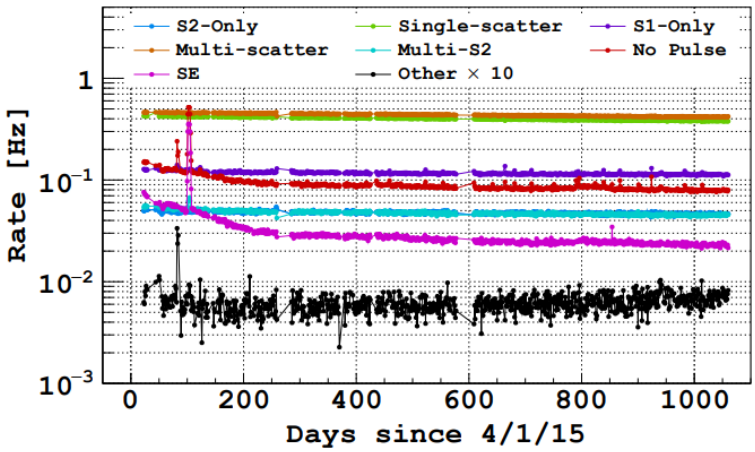

Fig. 2: Rate of each event type in data collected with UAr.

Figure 2.14: Picture from [40] and [80]. The event rate for each category is plotted as a function of the entire data acquisition period of DarkSide-50. The vertical dashed line denotes the time when the getter was reintroduced into the system.

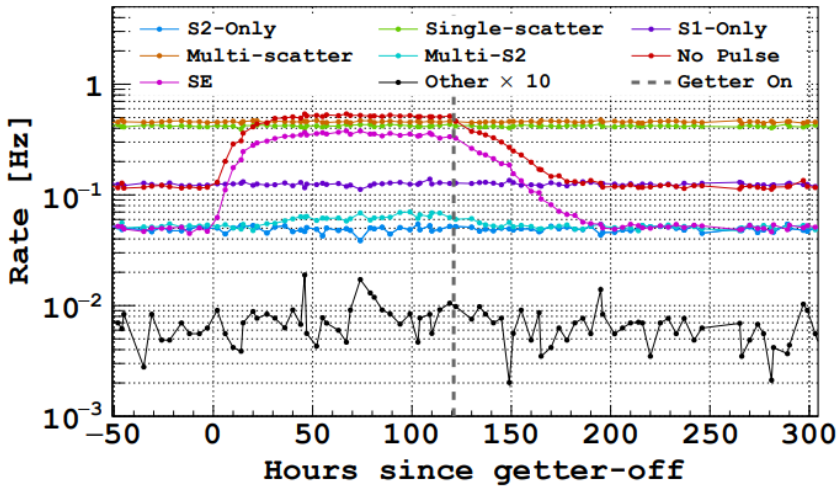

Figure 2.15: Picture from [40] and [80].The hourly rate variation for each category of events is shown from the moment the getter was removed from the system. The vertical dashed line denotes the time when the getter was reintroduced into the system.

Regarding the SE and No Pulse categories, their rates show two distinctive decreasing trends: one occurring up to the 200th day, characterized by a time constant of 65 days, and another phase with a time constant of 8 years. Notably, sharp spikes are observed in the other category around 80 days and in SE and No Pulse categories around 100 days. The former spike originated from an anomalously high rate in one of the PMTs, while the latter coincided with the "getter-off" period, during which the hot getter was temporarily removed from the gas circulation system for maintenance from day 99 to 108. During this interval, the absence of the hot getter resulted in a quick increase in event rates in the TPC. These additional events displayed short lifetimes, suggesting they were triggered right after the previous events and generated relatively lower light compared to the average light emitted by normal events.
Picture 2.14 displays the rates of each event category hours after the getter removal. The increases are observed exclusively in SE and no S1 Pulse categories, indicating that these events represent S2-like signals with a charge of < 4 e^-. Due to the radial dependency of the field within the gas pocket, SE events occurring near the inner radius of the TPC produce sufficient light to be detected by the detectors and hence are classified as SE events. Conversely, if an SE event occurs closer to the outer radius of the TPC, the amplification of the signal might not be sufficient to be detected as a pulse, leading to its categorization as a no-pulse event.
Furthermore, spatial correlations between preceding normal events and subsequent small-signal events were observed. Based on these findings, we can conclude that these additional events may arise due to an impurity that delays electron drifting, possibly nitrogen. The rate of these events experienced an exponential surge over two days and stabilized until the getter was reintegrated into the system. The rate decrease of the additional events exhibited a time constant of approximately 36 hours. The impurity introduced by the absence of the getter resulted in SE events, which were subsequently mitigated as well by the reintroduction of the getter [40].

2.4.6 Possible sources of single electrons

Different sources may contribute to isolated Single Electrons, as suggested by the following observations, which identify two distinct phenomenological classes: correlated SEs and uncorrelated SEs. Correlated SEs demonstrate a strong temporal correlation, characterized by an exponential time constant within the 1–1000 ms time scale, as well as an evident spatial correlation, often reconstructing beneath the same Photomultiplier. Moreover, the likelihood of observing a correlated SE scales linearly with the size of the parent event's S2 signal and drift time (tdrift). In contrast, uncorrelated SEs lack an identified parent event. The rate of correlated SEs generally decreases over time, except for a spike observed during the period when the getter was deactivated, with additional smaller-scale fluctuations in their rate correlated with fluctuations in the temperature of the charcoal radon trap.

Several possible mechanisms may account for the production of SEs within both populations. Numerous hypotheses are considered given the aforementioned observations. Potential explanations for SEs with $Ne^- > 1e^-$, involving the capture of drifting electrons by impurity-formed metastable anions, delayed biexcitonic ionization of metastable argon atoms, delayed electron extraction, self-organized criticality of radical impurities, spontaneous grid emissions, and fluorescence-induced photoionization. They are explored and discussed in [80]. One of the most crucial hypotheses concerns the presence of impurities and I in particular focused my contribution on the correlation between SEs and nitrogen.

Electrons may capture on an impurity G and be reemitted:

$$e^- + G \rightarrow G^- \tag{2.13}$$

$$G^- \rightarrow G + e^- \tag{2.14}$$

$$G^- + \mathrm{Ar} \rightarrow G + \mathrm{Ar} + e^- \tag{2.15}$$

Electrons can be released from an anion G^- through auto detachment and vibrational relaxation or collisional detachment, resulting in Single Electron events characterized by an exponential decay of their parent events (more detailed explanations can be found in reference [80]). The presence of multiple species or detachment channels may account for the various observed components, and the distinct temporal variations in SE rates suggest the involvement of at least two different species.
To investigate the potential correlation between SEs and parent events, a detailed analysis of time coincidences is conducted. The time difference, denoted as dT, between each SE occurrence and all preceding parent candidates within a 10-second window, is computed. To estimate the contribution of random coincidences, dT values for parent events that succeed SEs in the same period are considered.

The dataset is organized into 35-day intervals, excluding runs where the getter was deactivated. Subsequently, the dT distribution is examined and found to be effectively represented by the combination of two exponential functions:

$$g(dT) = \frac{R_1}{\tau_1} e^{-dt/\tau_1} + \frac{R_2}{\tau_2} e^{-dt/\tau_2} + C \tag{2.16}$$

The analyzed dataset reveals that the dT distribution can be accurately characterized by the sum of two distinct components, each with its respective decay constants τ_1 and τ_2, where τ_1 is less than τ_2. These components denoted as R1 and R2, represent the rates of the respective decays. To account for random coincidences, a parameter C is introduced. Furthermore, it is observed that when considering data obtained during the period when the getter was deactivated, an additional component with an intermediate decay constant becomes necessary to comprehensively describe the observed dT distribution. Importantly, τ_1 remains unchanged in this scenario. They [80] obtained τ_1=5 ms, τ_2=40-80 ms, and τ_3=16 ms (the extra component they have during the getter-off period). Thus we can affirm that the SE rates exhibit at least three distinct time constants: a short decay of approximately 4 ms, a long decay of around 45 ms, and a third one observed during the getter-off runs with a time constant of approximately 13 ms. The fact that the electron lifetime, related to the presence of electronegative impurities causing electron delay across the TPC, remains unaffected during the getter-off runs suggests that the impurity causing SE events with a time constant of around 13 ms is distinct from the impurity responsible for the electron lifetime loss.

Based on the faster rate reduction (occurring over approximately 36 hours) after the getter is reinstalled 2.14, it is deduced that the impurity causing the SE events during the getter-off period predominantly exists in the gas phase at the liquid argon temperature. One potential candidate for this impurity is N_2, which has a boiling temperature of 77 K, making it present in the gas phase under the experimental conditions.

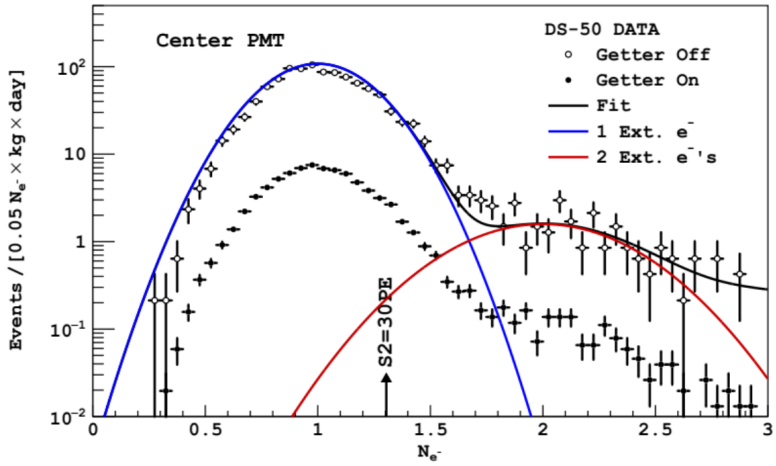

Figure 2.16: Event rate as a function of the number of electrons causing a signal during the getter-off and getter-on. This difference suggested the presence of a contaminant as explained in the text.

In 2.16 is the rate as a function of the number of electrons during getter-on and getter-off. We know how a single electron at the center of a PMT creates 23 ± 1 PE. The evidence about whether multi-electron SEs arise from single-electron ($1e^-$) pileup is not conclusive and yields mixed results. Although the SE pulse shapes may seem consistent with this explanation, when comparing the rates of $1e^-$ and $2e^-$ events, they do not align with this hypothesis [80].

The aim of the measurements and calculations of chapter 3 will be to verify or rule out the hypothesis that single electrons are associated with nitrogen impurities. Specifically, it is hypothesized that during the getter-off period, there might be a temporary increase in the concentrations of nitrogen and oxygen, subsequently affecting the auto-oscillation triplet lifetime of argon and thus leading to an increase in the number of single electrons.

2.5 LEGEND and neutrinoless double β decay

LEGEND-1000 is a large-scale scientific experiment focused on the investigation of Neutrinoless Double-Beta ($0\nu\beta\beta$) Decay in enriched Germanium detectors [81]. The experimental setup consists of 1000 kg of Germanium detectors, enriched to over 90% of the isotope of interest ^{76}Ge, operated within a liquid argon active shield.

The primary goal of LEGEND-1000 [81] is to explore the region of parameter space corresponding to neutrino mass. The experiment will be installed in Gran Sasso Laboratories. Neutrinos have played a pivotal role in particle physics discoveries, driving advancements in our understanding of weak interactions and quantum field theories. However, the question of whether neutrinos are Majorana particles, identical to their antiparticles, remains unanswered. This property is linked to the origin of their mass and is predicted by various extensions of the Standard Model, as well as by the leptogenesis theory, which may explain the asymmetry of matter and antimatter in the universe.

2.5.1 Neutrinoless double-beta decay

Neutrinoless double-beta ($0\nu\beta\beta$) decay is the only known reasonable probe for the Majorana nature of neutrinos, although it has not yet been observed. The discovery of this decay process would unequivocally confirm the existence of new physics that violates the lepton number. Numerous efforts have been dedicated to the search for $0\nu\beta\beta$ decay, with experiments using isotopes such as ^{76}Ge, ^{120}Te, and ^{136}Xe setting constraints. The lower limits on the half-life of this decay process currently exceed 10^{26} years. These limits the Majorana neutrino mass ($m\beta\beta$) in the range of 100 meV for minimal extensions of the Standard Model. [82]
Thus starting from a parent nucleus (A, Z) we can write a neutrinoless double-beta decay as follows:

$$(A, Z) \rightarrow (A, Z + 2) + 2e^{-} + E \tag{2.17}$$

where E is energy. In this decay, we notice how there is a violation of the lepton number conservation by two units.
It is interesting to explore events of this nature, as they could potentially lead to an advancement beyond the standard model. Currently, however, such events are estimated to have a half-life time greater than 10^{26} years. Furthermore, since this type of decay leads to overall mass production, it is believed to be responsible for the formation of luminous mass in the universe, thus representing a process of baryogenesis [82].
Now, since neutrino oscillations have been measured in the three flavors [83], this has confirmed the fact that neutrinos have mass (or at least two out of three flavors, given that the differences in squared masses are positive) and that lepton mixing is large. The fact that neutrinos have mass is already a step away from the standard model. In the three-Majorana-neutrino paradigm, the phenomena related to neutrinos can be summarized by the neutrino mass matrix, as follows:

$$m_{\nu} = U diag(m_1, m_2, m_3) U^T \tag{2.18}$$

where m_1, m_2, and m_3 are the real neutrino masses and U is the PMNS matrix [84]. The hierarchy of the masses is still under discussion. So the effective mass of neutrino in double beta is

$$\langle m_{\beta\beta} \rangle = |U_i^2 m_i| \tag{2.19}$$

which is described by seven parameters that can be measured in other ways, like direct neutrino cinematic or cosmology [82]. Finally, the lifetime or neutrinoless double beta-decay is the following

$$\tau_{1/2}^{0\nu} = (G \langle m_{\beta\beta} \rangle^2 |\mathcal{M}|)^{-1} \tag{2.20}$$

this equation is based on the fact that there is no other mechanism other than this responsible for leptonic number violation [82]. G is the space factor, depending on the energy E of the decay, it is in the order of $10^2 5 yr e V^2$, and $\mathcal{M}$ is the nuclear matrix (more details in [82]).

$$\tau_{1/2}^{0\nu} = 10^{27-28} (\frac{0.01eV}{\langle m_{\beta\beta} \rangle})^2 \text{years} \tag{2.21}$$

so the half lifetime goes like the inverse of the square of the mass $\langle m_{\beta\beta} \rangle$, and this explains why the lifetime for neutrinoless is much larger than the lifetime for standard beta decays. We also emphasize that such large lifetime values are the reason why we need detectors with many targets. Similarly, the current limit on the effective mass $\langle m_{\beta\beta} \rangle$ is 0.2 eV.

2.5.2 Double $0\nu\beta\beta$ detection

Looking for $0\nu\beta\beta$ decay, we study the kinematic of the two electrons emitted in the process. Usually, we need to measure the energy of the two-electron and we need to reconstruct the path of them to reject background events. The observed energy of the decay signal is shown peak, a single line corresponding to a specific energy value, as no antineutrinos are emitted during the decay process. Since we can measure the energy, the signal search can be focused within a small energy window centered around the peak, and the width of this region of interest is determined based on the energy resolution of the detector [82]. The number of candidate events N observed is assessed to evaluate the potential existence of $0\nu\beta\beta$ decay and to distinguish it from background events [82].

$$N = \ln 2 \frac{N_A}{W} \frac{a\epsilon Mt}{\tau_{1/2}^{0\nu}} \tag{2.22}$$

In this context, where N_A represents Avogadro's number, W denotes the molar mass of the source material, a represents the isotopic abundance of the parent isotope, stands for the detection efficiency of the signal within the region of interest, and t is the measurement time. The sensitivity to the half-life is influenced by the total number of counts observed, which includes both signal and background events [82]. The half-life time depends on the presence of the background. In the background free case, we have

$$\tau_{1/2}^{0\nu} \simeq a\epsilon Mt \tag{2.23}$$

otherwise, we write

$$\tau_{1/2}^{0\nu} \simeq a\epsilon\sqrt{\frac{Mt}{\beta\Delta E}} \tag{2.24}$$

where B is the background index (more details in [82]) and ΔE is energy resolution of the detector. We notice how the background-free experiment is better as it scales linearly with time, while in the other case, it goes like $\sqrt{t}$.

Using the aforementioned equation 2.24, we can make assumptions about the optimal material to use as a target and the general conditions for neutrinoless beta decay research. As stated earlier, it is imperative to have a minimal or highly suppressed background (thus, a small B). Additionally, a good detector resolution (ΔE small), an abundant presence of the isotope used in the interaction (large a), and the ability to produce substantial quantities of the chosen element, preferably on the order of tons (large M), are crucial factors.

An ideal target material does not exist, as each one has its advantages and disadvantages. Consequently, different experiments employ various target materials, some of which include:

1. ^{48}Ca by ELEGENT IV [85]
2. ^{76}Ge by GERDA [86] and LEGEND [81]
3. ^{82}Se, ^{96}Zr, and ^{100}Mo by NEMO-3 [87]
4. ^{116}Cd by Aurora [88]
5. ^{130}Te by CUORE [89]
6. ^{136}Xe by EXO-100 [90] and KamLAND-Zen [91]

The aspect that most significantly influences the choice of target material lies in the attempt to minimize background contributions. The signal-to-background ratio, as described in [82], can be expressed as follows:

$$S/B \simeq (\frac{E}{\Delta E})^6 \frac{\tau_{1/2}^{2\nu}}{\tau_{1/2}^{0\nu}} \tag{2.25}$$

This is because the background predominantly comprehends non-neutrinoless beta decay originating from isotopes present in the materials of various components of the detector. Therefore, selecting isotopes with very long half-lives for such interactions allows us to overcome these background signals and, consequently, improve the overall S/B ratio. Similarly, we can choose a target material with a large beta decay energy, aiming to overcome potential double-beta decay with background neutrinos. The detection efficiency of the 0-decay signal is improved by integrating the source as the detector medium [82]. This configuration allows for much shorter path lengths of the two signal electrons within the active medium, enabling good energy resolution. On the other hand, when the source material is external to the detector, the likelihood of at least one of the two electrons evading detection or degrading its energy increases. It is of course more convenient to have a high natural abundance of the desired isotope as the cost of isotope enrichment is typically contingent on the isotopic abundance of the starting material, with higher natural abundances leading to lower costs. In cases where the natural abundance is sufficiently high, isotope enrichment may be unnecessary [82].

Next generation of detector like LEGEND-1000 [81] aim at a half-life time for neutrinoless beta decay $\tau_{1/2}^{0\nu} \simeq 10^{28}$ years with a very low background < 0.1counts/year/tonne. Other sources of background and techniques to remove or reduce them include [82]:

1. Solar neutrinos: Their impact can be reduced by incorporating a high mass loading of the decaying isotope in the target medium, thereby improving the signal-to-background ratio, specifically reducing the interference from neutrino-electron elastic scattering.

2. Trace amounts of radioisotopes from the natural U and Th chains must be minimized in any materials near the active detector volume. Other pervasive natural radioactivities like ^{3}H, ^{40}K, and ^{14}X possess lower decay energies and do not significantly affect $0\nu\beta\beta$-decay searches.

3. Natural radioactivities originating far away from the active detector volume, including γ-rays from the primordial chains and neutrons from (α, n) reactions arising from the rock walls of the underground laboratory, can be blocked by passive shielding, such as clean Pb or Cu, water, or liquid cryogen. The latter two options may also allow the shielding material to function as an active veto to reject cosmic rays.

4. Cosmic-ray muons (μ). In deep underground laboratories, prompt muon interactions in the detectors are usually not problematic as these interactions deposit substantial energy and can be easily vetoed. The main concerns are the activation of long-lived isotopes and the production of secondary neutrons induced by muons through mechanisms like μ capture in nuclei, muon-nucleon quasi-elastic scattering, electromagnetic showers, and photo-neutron production via virtual photon exchange.

5. Backgrounds from cosmogenic production of radioisotopes during the experiment are challenging to identify, however, they can be significantly reduced by building the experiment deep underground

2.5.3 LEGEND-1000 experiment

LEGEND-1000 [81] has been designed to explore $0\nu\beta\beta$ decay with a discovery sensitivity at the 99.7% confidence level (CL), which corresponds to a 50% chance of having a 3σ significance signal of neutrinoless beta decay. Detecting signals at the Q value ($Q\beta\beta$) of $0\nu\beta\beta$ decay (2039 keV), they would be able to detect in the germanium detector a very specific and unique signal. The low-Z shielding and scintillating veto for background suppression from GERDA alongside ultrapure materials and components will be exploited to achieve a $\tau^{0\nu}_{1/2}$ discovery sensitivity of approximately 10^{28} years. In the initial phase, named LEGEND-1000, modifications of the GERDA experimental infrastructure at LNGS will allow the accommodation of approximately 1000 kg of ^{76}Ge-enriched detectors. The $\tau^{0\nu}_{1/2}$ discovery potential for LEGEND-1000 is projected to be approximately 1028 years, with a background index of 0.1 count/tonne/year leading to a reduction of approximately 30 times compared to that of GERDA [82]. In Figure 2.17, the schematic representation of

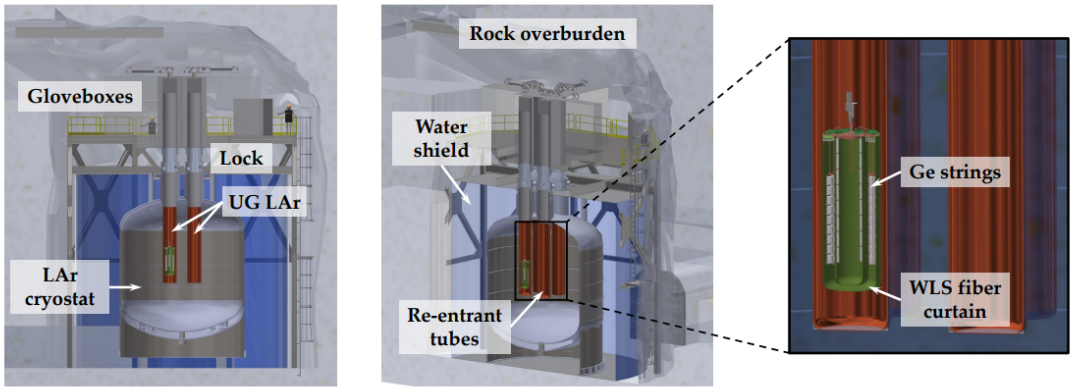

Figure 2.17: General structure of the LEGEND experiment from two perspectives [92]

LEGEND-1000's detector is depicted. The external part consists of a water tank used as a veto for the Cherenkov radiation. This might be caused by muons traversing the detector and the vito itself is a protection against environmental radioactivity. In the intermediate layer, there is a 25-ton liquid argon cryostat with a wavelength shifter and PMTs to read liquid argon scintillation signal. The cold argon also functions to cool the entire structure, particularly the high purity Germanium crystal detector located inside. Certain events, such as Compton scattering by γ rays, leave signals in both the internal detector and the liquid argon, and they can be rejected through a veto system. Regarding the internal part dedicated to neutrinoless beta decay detection, there will be around 200 to 300 Inverted Coaxial Point detectors with high-purity Germanium crystals, enriched with ^{76}Ge, reaching approximately one ton in weight, out of which approximately 150 kg will be transferred from the previous LEGEND-200 experiment, while the rest will be newly produced. Further details are available in [92], [93], [94].

As for the 25 tons of liquid argon required, the purification process will essentially follow what was discussed in previous chapters concerning the LAr needed for DarkSide-20k. Thus, a chemical purification process will be necessary to eliminate impurities like nitrogen, or even better, if production times are reasonable, reduce the presence of the ^{39}Ar isotope. Regarding LEGEND, it is imperative to consider the presence of the ^{42}Ar isotope as well. Analogously to ^{39}Ar, it undergoes β decay ($^{42}\mathrm{Ar} \rightarrow {}^{42}\mathrm{K}^{+} + \beta^{-} + \bar{\nu}_e$). The emitted electron's

energy is Q_β=0.599 MeV. Since the sought-after signal has an energy of $Q_{\beta\beta}$ = 2.039 MeV, and $Q_\beta < Q_{\beta\beta}$, this beta decay does not contribute to the background in the experiment's region of interest. However, the ^{42}K produced from this decay undergoes another beta decay as follows ($^{42}K^+ \rightarrow {}^{42}Ca^{++} + \beta^- + \bar{\nu}_e$), this time with an energy of 3.525 MeV, which can constitute background. It is estimated that 30% of LEGEND's background is caused by this isotope [95]. The formation of ^{42}Ar occurs through the interaction of cosmic alpha particles with ^{40}Ar in the following manner ($^{40}Ar + \alpha \rightarrow {}^{42}Ar + p + p$). Therefore, similar to ^{39}Ar, ^{42}Ar is suppressed by taking argon from underground sources, and hence LEGEND will employ UAr as well. Additionally, further suppression of this isotope is achievable through cryogenic distillation and it is theoretically more reasonable than the separation of ^{39}Ar, as the mass difference between ^{40}Ar and ^{42}Ar is greater than that between ^{40}Ar and ^{39}Ar.

It is noteworthy that the Aria project could potentially be connected to the future development of LEGEND in two ways: first, by producing high-purity Germanium with ^{76}Ge concentration of at least 87% (or higher). This can be achieved through liquefied germane GeH_4 at cryogenic temperatures, which can be separated via cryogenic distillation to isolate $^{76}GeH_4$, subsequently returning to the solid state as ^{76}Ge for use in LEGEND. On the other hand, this project could contribute to the production of chemically pure argon via cryogenic distillation in Seruci-1. In the upcoming chapters, specifically in section 7.4, we will decide through simulations the quantities and conditions required for the mentioned production processes.

Chapter 3

Liquid Argon Signal Shape Analysis in DarkSide-50

In this section of the thesis, the primary objective is to investigate potential correlations between single-electron events and nitrogen in DarkSide-50. To understand the consequences of the getter shutdown (discussed in detail in 2.4.4), if that caused the increase in single-electron signals in the TPC, and whether it is possible to establish a threshold for argon impurity concentration before it affects detection.

We will, therefore, proceed in the following order: First, we will discuss how impurities such as nitrogen and oxygen can influence argon scintillation 3.1; then, we will study the correlation between them and electron lifetime to rule out the hypothesis that significant oxygen concentrations were present during the getter-off period. Next, we will fit the DarkSide-50 waveforms to understand if there were significant variations in the argon triplet lifetime during the run 3.1.1 3.1.2. Lastly, we will analyze changes in the triplet lifetime before, after, and during the period when the getter was not operational, to determine if the significant increase in single-electron events was in fact caused by nitrogen or other factors 3.2.

3.1 Nitrogen contamination in DarkSide-50

In this chapter we will study the experimental data obtained from Darkide-50, the predecessor of the larger DarkSide-20k, which is currently under construction, to establish a threshold for nitrogen contamination in argon before its scintillation can be affected. This is closely related to the Aria project, as Seruci-1 will be responsible for the chemical purification of argon destined for DarkSide-20k. As we will discuss in the next chapter, specifically in , Seruci-1 should be capable of completely suppressing nitrogen in argon (theoretically down to 10^{-30}); however, there might be subsequent contaminations, such as residues in the pipelines or column malfunctions during the run, leading to a higher concentration of the contaminant than expected.
If this were the case, it becomes necessary to set a maximum value for the acceptable concentration of nitrogen in argon. Beyond this threshold, the argon sample should be discarded as it could potentially influence the argon's scintillation, particularly regarding the slow component, known as the triplet component. In this chapter, we will study the mechanisms by which nitrogen influences argon's scintillation. Subsequently, we will analyze the experimental results from DarkSide-50 to establish the aforementioned threshold.

Recalling what was mentioned in the chapter related to the DarkSide project, the operating and detection mechanism of both DarkSide-50 and DarkSide-20k remains the same. It involves the use of a time projection chamber for the detection of two signals: free electron charge and scintillation light, both produced by the ionization of liquid argon (LAr) caused by the passage of a particle. The scintillation process can be influenced by the presence of contaminants such as nitrogen and oxygen. Specifically, quenching processes (non-radiative processes) occurring during two-body collisions between impurity molecules and Ar_2 excimer states (which typically undergo radiative decay resulting in scintillation light emission) and the absorption of emitted ultraviolet photons by photosensitive impurities can occur, depending on the nature of the impurity and its concentration level, as discussed in 2.4.1. Argon generates both electron-hole (Ar^+) pairs and excited Ar atoms interacting with a crossing ionizing particle [61], with the Ar/Ar^+ ratio of produced excitons and ion pairs being 0.21. These excited Ar atoms undergo collisions with Ar atoms (self-trapping), leading to the formation of the Ar_2 low excited dimer. Also, Ar^+ ions also contribute to the formation of Ar_2 through various subsequent processes such as electron recombination 2.4.1.

In both cases, the excited dimer states formed in LAr are identified as the singlet $^1\Sigma_u$ and the triplet $^3\Sigma_u$ excimer state in the M-band, typical of the argon structure. The rise time for excimer formation and relaxation is rapid for both components: from 1 to 10 ps for self-trapping and around 100 ps for recombination. The de-excitation processes driving scintillation light emission, occur in the Vacuum Ultra-Violet (VUV) region and lead to the dissociative ground state $^1\Sigma_g$.

$$Ar_2 = \gamma + 2Ar \tag{3.1}$$

In the liquid phase, different recombination mechanisms may occur, and of course, they are expected to depend on the type of ionizing particle and its Linear Energy Transfer i.e., the specific energy loss along its trajectory. These mechanisms significantly influence both the number of excited dimers Ar^2 generated per unit of deposited energy and the relative populations of the singlet and triplet states [61].

Extensive studies have been conducted on the γ decay wavelength spectrum of both excimer states. The spectral profile is described by a Gaussian shape, peaking at a wavelength of approximately 128 nm, with a full width at half maximum of about 6 nm. However, the time dependence of photon emission from liquid-phase Ar is less precisely known. In literature, the values of excimer lifetimes and amplitudes are different from each other. As an initial approximation, all measurements demonstrate a scintillation light emission characterized by a double exponential decay pattern. This pattern comprehends two distinct components: a fast component, with a time constant τ_s (short), and a slow component, with a time constant τ_l (long). These components are associated with the lifetimes of the singlet $^1\Sigma_g$ and triplet $^3\Sigma_g$ states in LAr, respectively [61] [96] [97].

While the time constants remain relatively unchanged with variations in ionization density, the amplitude ratio (p_s/p_l) between the singlet and triplet states is profoundly influenced by this parameter. Notably, more $^1\Sigma_g$ states (fast component) are produced with at higher deposited energy densities. For instance, the relative amplitude of the fast and slow components for minimum ionizing particles is reported as $p_s/p_l = 0.3$ ($p_s = 23\%$, and $p_l = 77\%$, respectively). However, for heavily ionizing particles, such as α-particles and nuclear recoils, the intensity ratio increases significantly (e.g., $p_s/p_l = 1.3$ for α-particles and $p_s/p_l = 3$ for nuclear recoils, although higher values have been observed elsewhere). This wide separation in amplitude ratios is a crucial characteristic of scintillation signals in LAr, which allows for the establishment of efficient Pulse Shape Discrimination criteria, enabling effective particle identification [98] [61].

In summary for argon scintillation we must consider two states $^1\Sigma_g$ and $^3\Sigma_g$, with lifetime τ_s and τ_s and relative amplitudes p_s and p_l. Our next goal is to see how they are influenced by the presence of contaminants and quenching. As suggested in [61], scintillation processes are de-excitation and thus we expect an exponential decay rate

$$F(t, \tau_s, \tau_l, p_s) = \frac{p_s}{\tau_s} e^{-t/\tau_s} + \frac{1 - p_s}{\tau_l} e^{-t/\tau_l} \tag{3.2}$$

where if we do not consider the presence of other components (some sources like [61] suggest the presence of an intermediate component with lifetime $\tau_m = 30 - 40$ ns) then $p_l = 1 - p_s$. Residual concentrations at the ppm level of CO_2, CH_4, Kr, and O_2 contaminants, which are commonly found in commercially available argon, can significantly reduce the intensity of scintillation light. This reduction occurs due to two main processes: first, the quenching effect that impacts the excited molecular states of argon before photon emission during de-excitation, and second, the absorption of the emitted scintillation photons. In principle, other processes involving excited atomic states (Ar) before excimer formation, such as excitation transfer and non-radiative quenching to or by impurity molecules, could occur. However, these reactions, while observed in argon gas mixtures, have minimal influence on liquid argon [61]. Quenching of excited atomic states by N_2 molecules can occur, competing with exciton self-trapping processes that lead to the formation of (Ar_2) dimers and is described by the following expression.

$$Ar_2 + N_2 \rightarrow 2Ar + N_2 \tag{3.3}$$

This non-radiative collisional reaction competes with the de-excitation process that results in ultraviolet light emission. Consequently, the population of Ar_2 is depleted before light emission occurs, leading to a significant reduction in the scintillation light yield. In more detail, the quenching process leads to a reduction in the concentration of excimers Ar_2, while the contaminant concentration N_2 remains constant over time. Therefore, for this scenario, a first-order rate law can be approximately assumed, characterized by the Ar_2 quenching rate constant k_Q.
We can write the probability function similar to 3.2 but introduce an apostrophe to indicate that the parameters may be affected by the presence of nitrogen [61].

$$F(t, \tau_s', \tau_l', p_s') = \frac{p_s'}{\tau_s'} e^{-t/\tau_s'} + \frac{p_l'}{\tau_l'} e^{-t/\tau_l'} \tag{3.4}$$

where

$$\frac{1}{\tau_s'} = \frac{1}{\tau_s} + k_Q[N_2] \tag{3.5}$$

$$\frac{1}{\tau_l'} = \frac{1}{\tau_l} + k_Q[N_2] \tag{3.6}$$

$$p_s' = \frac{p_s}{1 + \tau_s k_Q}[N_2] \tag{3.7}$$

$$p_l' = \frac{p_l}{1 + \tau_l k_Q}[N_2] \tag{3.8}$$

where in this case $p_s' + p_l' \neq 1$ and $[N_2]$ is the nitrogen concentration. We can define the surviving factor Q_F such that

$$Q_F = p_s' + p_l' \tag{3.9}$$

That is always between 0 and 1: if it is equal to the unit there is no quenching, while if Q_F=0 the signal is 0 as it has all been quenched (limit case).

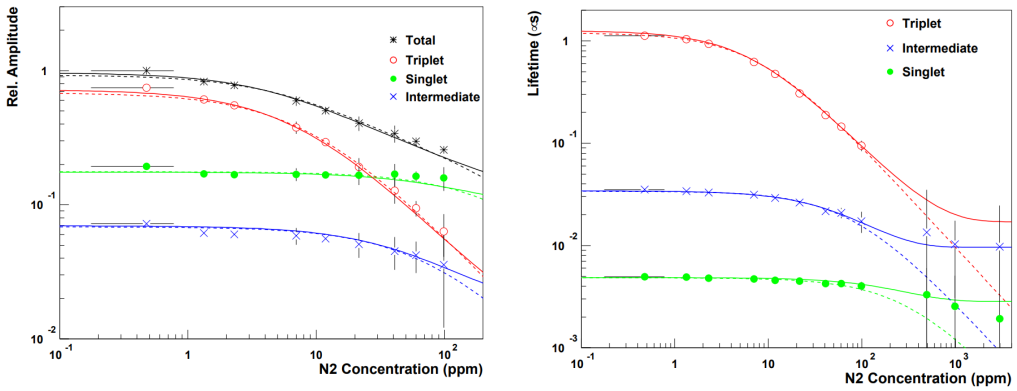

Figure 3.1: Effect of nitrogen contamination on argon lifetime (right) and relative amplitude (left) measured as part of WArP program. [61]

Such formulas, together with the detector's response function, were employed in [61] as part of the WArP project to fit the waveforms obtained from a specific detector having 1 kg of active liquid argon mass with controlled and chosen nitrogen contaminations. The scintillation signal was measured using PMTs, and the dimensions of the detector were 12 cm x 8.5 cm. Without delving into the technical details of that particular system, which is substantially different from the one we are studying (DarkSide-50), we show in the following figures (3.1) the fitting parameters they obtained for various nitrogen contaminations, specifically, how the lifetimes and relative amplitudes change.
In the presented data, below 1 ppm of nitrogen, there is no significant effect related to its presence. Moreover, the parameter most influenced by the presence of nitrogen, particularly at lower nitrogen concentrations, is the lifetime of the triplet component (τ_l).
It is clear how all parameters vary with the concentration of nitrogen and consequently with the quenching effect. Concerning the amplitudes concerning nitrogen concentration, the triplet amplitude p_l decreases more compared to the singlet amplitude p_s. Hence, another parameter of interest influenced by nitrogen is the ratio (p_s/p_l), which we anticipate will increase with higher quenching levels.
Based on these, we repeat a similar procedure concerning the DarkSide-50 results. However, we are uncertain about the nitrogen impurities during the run, so we will analyze the parameters most affected by the presence of nitrogen to estimate its concentration. Additionally, our objective is to validate the results and thresholds from the aforementioned study 3.1, including those related to DarkSide-50, which is considerably larger and fundamentally different from the detector used in [61]. Consequently, it will be necessary to define a distinct function to fit the waveforms from DarkSide-50, which we will delineate in the forthcoming paragraphs.

3.1.1 Waveform fit function

To define the total waveform fit function we need to define three different contributions.

1. Argon scintillation function, defined as in the previous case 3.2 $F(t, \tau_s, \tau_l, p_s)$

2. TPB remission contribution to the waveform. In both DarkSide-20k and DarkSide-50, a wavelength shifter called TPB changes the frequency of the scintillation photos to make them able to be detected by the PMTs. $H(t, \tau_1, \tau_2, p_{\text{TPB}}, p_{\text{TPB2}})$

3. The effect of the PMTs resolution is the convolution with a Gaussian function [99]. A delta-function signal would be detected by the PMTs as a Gaussian. $G(t, \sigma)$

The Gaussian response function of the PMTs is characterized by the center of the peak t_0 and σ which is the resolution of the PMT. In our case, it is centered in t_0=0.

$$G(t, \sigma) = \frac{e^{-t^2/2\sigma}}{\sqrt{2\pi\sigma^2}} \tag{3.10}$$

The PMT response according to [97] has one prompt component with amplitude p_0 and one or two slow components with amplitudes p_{TPB} and p_{TPB2}. Of course $p_0 + p_{\text{TPB}} + p_{\text{TPB2}} = 1$

$$H(t, \tau_1, \tau_2, p_{\text{TPB}}, p_{\text{TPB2}}) = (1 - p_{\text{TPB}} - p_{\text{TPB2}}) + \frac{p_{\text{TPB}}}{\tau_{\text{TPB}}} e^{\frac{t}{\tau_{TPB}}} + \frac{p_{\text{TPB2}}}{\tau_{\text{TPB2}}} e^{\frac{t}{\tau_{TPB2}}} \tag{3.11}$$

To consider all these contributions we need to perform the convolution $(*)$ among them

$$\begin{aligned} &R(t, \sigma, \tau_s, \tau_l, p_s, \tau_{\text{TPB}}, \tau_{\text{TPB2}}, p_{\text{TPB}}, p_{\text{TPB2}}) = G(t, \sigma) * F(t, \tau_s, \tau_l, p_s) * \\ &H(t, \tau_{\text{TPB}}, \tau_{\text{TPB2}}, p_{\text{TPB}}, p_{\text{TPB2}}) \end{aligned} \tag{3.12}$$

In [97] there are more details about the calculation of the convolution. The whole function is then shifted by a time t_0, multiplied by an amplitude A, and a constant additive term C was added to take care of the background. Doing so we get the following fit function R'

$$R'(t, \sigma, \tau_s, \tau_l, p_s, \tau_{\text{TPB}}, \tau_{\text{TPB2}}, p_{\text{TPB}}, p_{\text{TPB2}}) = A \cdot R(t, \sigma, \tau_s, \tau_l, p_s, \tau_{\text{TPB}}, \tau_{\text{TPB2}}, p_{\text{TPB}}, p_{\text{TPB2}}) + C \tag{3.13}$$

However, since the data we are managing are already background subtracted we considered the fit function R' with C=0 as well and compared the two cases. The value we obtained for C was found to be 3.20 ± 0.05 PE/μs, while the other parameters remained consistent within their respective uncertainties when compared to fits where C was constrained to be zero. No notable or significant differences were observed; therefore, we proceeded with the simplified assumption of $C = 0$. The fit parameters of R' are the following:

1. Amplitude and reference time A and t_0

2. Resolution of the PMTs σ.

3. Argon singlet scintillation fraction of probability p_s

4. Argon singlet and triplet scintillation lifetime τ_s and τ_l

5. TPB remission slow components fraction of probability p_{TPB}

6. TPB remission slow components lifetime τ_{TPB}

It is crucial to highlight that the literature does not reach a consensus regarding the appropriate function to use for fitting, accounting for both argon scintillation and TPB reemission. For instance, WArP [61] did not include the TPB contribution in the fit function, but rather employed three components to represent argon scintillation, introducing an

additional intermediate component (also exponential) in addition to the triplet and singlet components. Conversely, more recent papers such as Aris [97] incorporate the TPB contribution, which overlays the intermediate scintillation component of argon. Notably, this intermediate component, not represented as exponential in other literature, is reasonably presumed in WaRP to be a distortion resulting from TPB. On the other hand, [100] considers a more complex scenario, introducing both TPB and an argon scintillation component. However, the latter is not exponential; instead, it is given by the following expression:

$$F(t, \tau_s, \tau_l, \tau_I, p_s, p_l) = \frac{p_s}{\tau_s} e^{-t/\tau_s} + \frac{p_l}{\tau_l} e^{-t/\tau_l} + \frac{1 - p_s - p_l}{(1 + \frac{t}{\tau_I})^2 \tau_I} \tag{3.14}$$

With τ_I the lifetime of the intermediate component and $1 - p_s - p_l$ its relative amplitude. During our various attempts, we also employed this equation for argon scintillation, but unfortunately did not achieve significant results. Ultimately, we chose to adopt the function R', which coincides with the ARIS case, as it closely resembles the conditions in DarkSide-50 and provided the most effective fit (with the lowest chi-squared) compared to the attempts made.

3.1.2 DarkSide-50 waveforms and cuts

For the analysis and fitting of DarkSide-50 data, the waveforms measured by PMTs were considered after reconstruction and stripping. Therefore, the study of raw data and how they were cleaned and made easily accessible is beyond the scope of this thesis. We will, therefore, assume these steps as established and directly study the waveforms, such as the one shown in Figure 3.2, where the number of photoelectrons per microsecond is plotted against time during acquisition.

Another advantageous aspect of dealing with pre-processed data is that for each waveform, we already have various available data, allowing us to easily apply cuts, i.e., discard problematic data that should not be included in the analysis. Some of the data we have at our disposal include f_{90}, S1, and S2, which have been discussed in Section 2.4.1, as well as the drift time and additional signal numbers, such as S3, S4, etc.

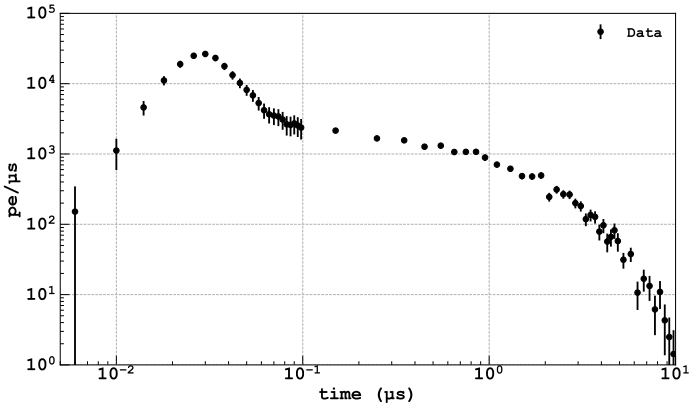

Figure 3.2: Example of a waveform measured by PMTs during DarkSide-50 experiment.

The following cuts were applied to select the correct waveforms to study:

1. 100>S1>20000 PE. Suggested by [97], to avoid saturation of the signal S1 (upper limit) and to avoid single electrons as they have a signal S1 below 4 electrons, that

correspond to 92 PE. Also as suggested in [101] a high signal S1 may be due to α particles.

2. Number of pulses Npulses=2 to select events with one S1 and one S2 signal. In this way, we reject the aforementioned multi-scattering of γ-particles in the detector.

3. Top-bottom asymmetry (signal S1 measured at top minus bottom, divided by the sum between top and bottom) $|S1_{tba}|<0.9$. To remove pathological cases.

4. $0.5>f_{90}>0.1$. To select electron recoil events [101] as the description of nuclear recoil is outside the goals of this thesis and already discussed in paper [102].

5. Drift time tdrift$>$ 20 μs. To avoid overlapping between S1 and S2 and to have S2 in the fit range

6. Time between the event and the previous one $\Delta t>0.02$ s to avoid SE events

7. $S1_{FWHM} < 100$ ns to avoid pile up in S1 and S2.

After the cuts, it was determined that the statistics could be enhanced by grouping the waveforms in sets of $5 \cdot 10^4$ and computing the average of each one. On each of them was performed a fit with an expected function including the Gaussian resolution of the PMTs, two scintillation components of liquid argon, one prompt and one or two delayed components of TPB re-emission, as suggested in [97] and [101]. Therefore, initially, we will perform the fit on an average of several waveforms, independently of the other parameters, provided they have survived the cut. Subsequently, we will group the signals based on the S1 signal to verify whether there are any correlations between the intensity of the primary signal and the fit parameters. The initially considered fit range extends from 0 to 10 µs since, for studying the argon scintillation, it is sufficient to consider the S1 signal.
In 3.3 is as an example the fit of a waveform with function R'. The gray line is the total

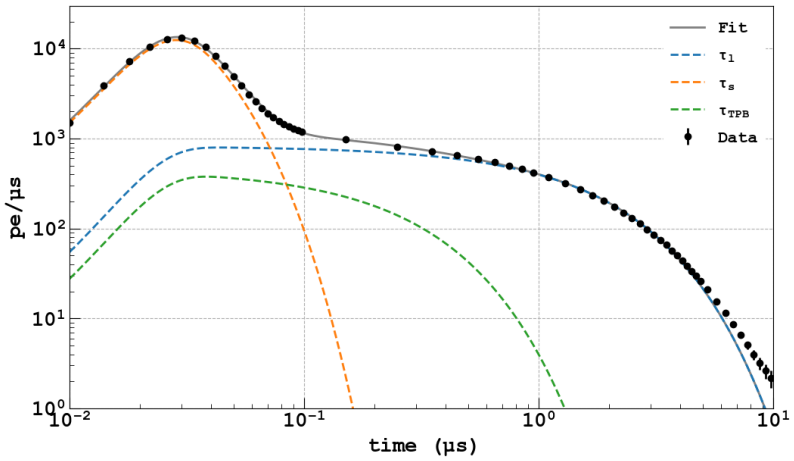

Figure 3.3: Group of 50000 waveforms averaged and fitted with the function R' as defined in this chapter. In the picture are shown the whole fit (gray) and its different components (dashed lines): singlet (orange) and triplet (blu) argon scintillation and TPB remission (green) convoluted with the Gaussian resolution.

fit function, while the dashed lines are the argon scintillation (singlet in orange and triplet

in blu), and the TPB response (green) convoluted with the Gaussian resolution. From this picture notice how there is a good overlap between the fit function and the data.

Parameters	Value
τ_l	1.375 ± 0.001 μs
p_l	0.6957 ± 0.0006
τ_s	13.65 ± 0.02 ns
p_s	0.3043 ± 0.0006
τ_{TPB}	209 ± 1 ns
p_{TPB}	0.282 ± 0.001
t_0	0.020895 ± 0.000006 μs
σ	7.4 ± 0.3 ns
A	1494.6 ± 0.4

Table 3.1: Results of the fit of groups of 50000 waveforms with function R' considering only one 1 TPB remission slow component. The results are mediated over the entire data acquisition period and across different runs in the DarkSide-50 experiment.

Finally, we provide a plot 3.4 of the evolution of the relative amplitude, p_l, and the lifetime, τ_l, of the argon scintillation triplet lifetime as a function of the DarkSide-50 run time, which spans a total of almost 3 years. Throughout this period, there are interruptions corresponding to experiment shutdowns or suspensions of operation.

It is important to underline that an increase in the triplet lifetime alone is consistent with a decrease in the concentration of impurities such as nitrogen. The same effect would instead be much smaller (and thus not visible) on the relative amplitudes or the singlet scintillation lifetime, as shown in 3.1. By using equation 3.5 and the values of τ_l at the beginning and the end of the run and with $k_Q = 0.11$ ppm^{-1} μs^{-1} [61] we obtain $N_2 = 0.031 \pm 0.009$ ppm. This might indicate that our results are consistent with a situation where there is 31 ppb of nitrogen at the start of the run which gradually decreases until its concentration is no longer appreciable.

The variation of τ_l might be also due to other impurities (mainly O_2). We know from [103] that contaminations of oxygen in liquid argon can have the following effects:

1. Absorption of scintillation photons
2. Quenching processes similar to those caused by N_2 in pure argon
3. Ionization attachment of electrons

Of particular interest is the last effect, as it allows us to estimate the concentration of O_2 by observing its impact on the electron lifetime. In this case, diatomic oxygen molecules can form with free electrons.

$$e^- + O_2 \rightarrow {O_2}^- \tag{3.15}$$

Such electron capture reduces the electron drift lifetime, which is the average time an electron in LAr exists before being captured. This effect is more pronounced with higher electronegativity of the impurity molecules that are being considered. The electron capture reduces the S2 signal, and thus, by observing an exponential decay of the S2 signal, it becomes possible to measure how the electron lifetime has changed over time during the

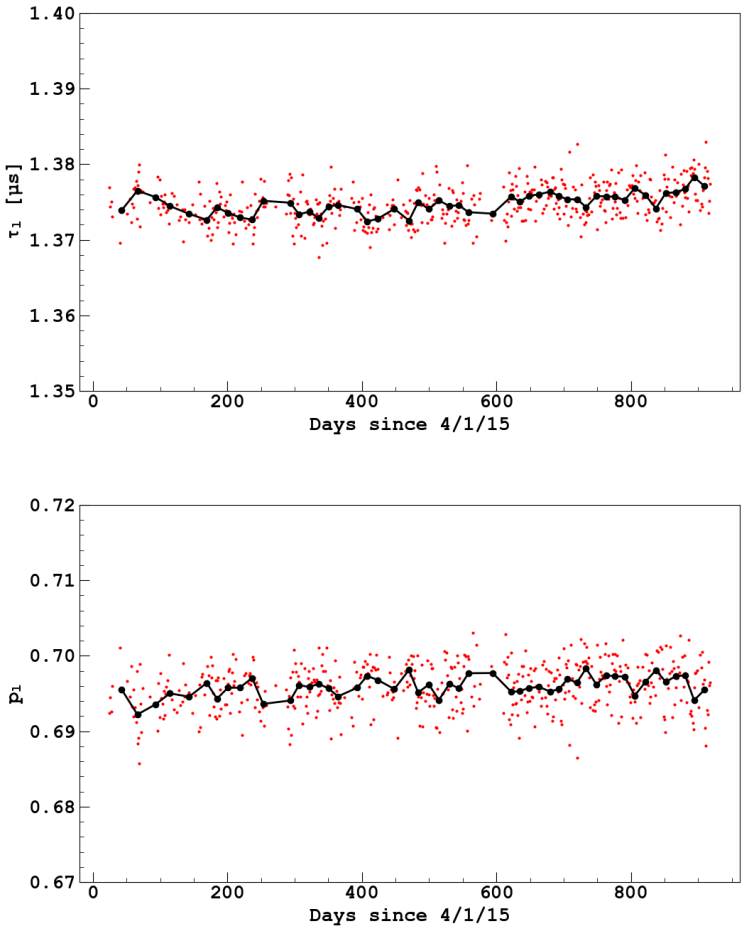

Figure 3.4: Relative amplitude p_l and lifetime τ_l of the argon scintillation triplet lifetime as a function of the DarkSide-50 run time, obtained fitting groups of 50000 waveformes. In black is the profile obtained averaging over groups of 10 values of p_l and τ_l to better show the general trend of the values.

DarkSide-50 run. Now, since the electron lifetime in DarkSide-50 is in the order of ms and ranges from 5 ms to 30 ms we can use the following formula to estimate the concentration of O_2 as suggested by [103] (the contribution of nitrogen to electron lifetime is negligible).

$$\frac{1}{\tau_e} = k_e[O_2] \tag{3.16}$$

Where τ_e is the electron lifetime as explained before, $[O_2]$ is the oxygen equivalent concentration (as it can be the concentration of oxygen or other electronegative molecules such as H_{20}) and k_e is a factor that depends on the drift field applied to the liquid argon and quantifies the capability of oxygen or oxygen-equivalent molecules to suppress the electron lifetime. It is similar to the previously defined k_Q which on the other hand was quantifying the capability of nitrogen to suppress argon triplet scintillation lifetime. k_e is in the order of 1 ppm^{-1} μs^{-1}, according to [103]. On the other side, the influence of oxygen on the triplet lifetime is given by

$$\frac{1}{\tau_l'} = \frac{1}{\tau_l} + k_O[O_2] \tag{3.17}$$

with $k_O = 0.54$ ppm^{-1} μs^{-1} So, we can compare the effect that nitrogen and oxygen have on the lifetimes; using 3.5 with the values of triplet lifetime at the beginning and at the end of the run and 3.17 with the max and min electron lifetime measured during the run 3.5, we get

$$k_O[O_2] \simeq 5 \cdot 10^{-5} \mu s^{-1} \tag{3.18}$$

$$k([O_2] + [N_2]) \simeq 2.5 \cdot 10^{-3} \mu s^{-1} \tag{3.19}$$

Therefore, it can be stated that the variation of the triplet lifetime is almost completely due

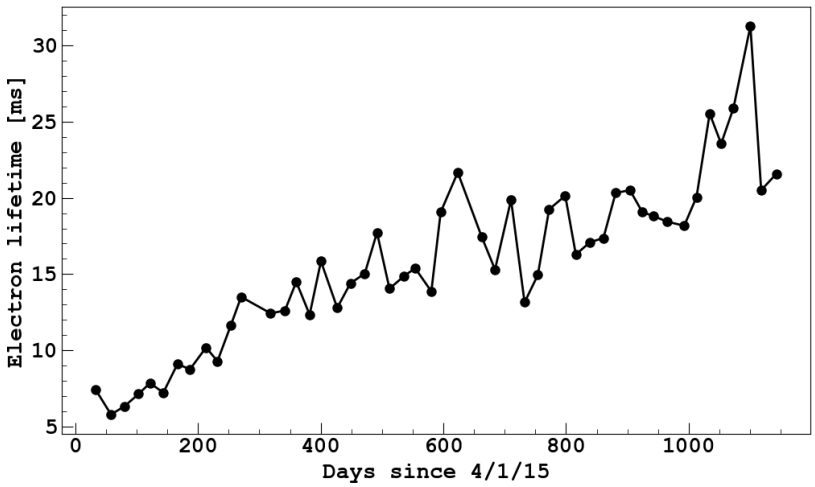

Figure 3.5: Plot from [80].Electron lifetime as a function of the time of the run of DarkSide-50. More details about how electron lifetime was calculated are in [80].

to nitrogen. In summary, we expect the triplet lifetime to be influenced similarly by oxygen and nitrogen, whereas only oxygen can significantly impact the electron lifetime. Referring to the previous calculations, we know that the variation in electron lifetime is not enough to justify the presence of significant amounts of oxygen in the detector. Consequently, small quantities of oxygen cannot influence the triplet lifetime, and thus, we are confident that

any variations might only be caused by nitrogen or other not electronegative molecules.

Such considerations still have some issues, particularly regarding the reliability and goodness of the fit performed. The reduced chi-squared (chi-squared divided by degrees of freedom) of the fit is around 12 for all the averages of groups of 50000 waveforms, although it might be overestimated because averaging multiple waveforms reduces the error on each group of waveforms, consequently inflating the chi-squared value. The correlation between parameters is strong and shown in Fig. 3.6.
In the example case shown in figure 3.3, the reduced chi-squared is 12.56, while the degrees of freedom correspond to the number of points used for the fit.

Figure 3.6: Correlation matrix of fit parameters of DarkSide-50 calculated while fitting groups of 50000 waveformes.

Furthermore, changing the fit range or introducing a second component to the slow TPB remission leads to different results. In Figure 3.4, we observe a constant trend for p_l and an increasing trend for τ_l. However, in the case with two TPB components (introducing two additional parameters, τ_{TPB2} and p_{TPB2}), the trends become opposite, with p_l increasing and τ_l decreasing, which is entirely inconsistent with the previous case. Attempts were made to fix some parameters to values measured by others in the literature, such as $\tau_s = 5$ ns, but acceptable results were not obtained.

Pulse shape fits of ionization signals in liquid argon were performed by a few experimental collaborations such as WArP [61], DEAP3600 [100], DUNE [72], and ARIS [97]. All three experiments used TPB as a wavelength-shifter of 128 nm scintillation light. The main finding of these collaborations is the presence of one or two additional components in the emitted light, on top of the well-known singlet and triplet liquid argon emission from dimers, that are attributed to TPB re-emission time constants. From table 3.2, it can be observed that the results obtained by us (indicated as DS50) are of the same order of magnitude as those from the aforementioned other sources, although the actual values are different. Not

	DEAP [100]	WARP [61]	ARIS(1TPB) [97]	DS50(1TPB)	ARIS(2TPB) [97]	DS50(2TPB)
τ_s	8.2 ns	4.9 ns		13.65 ns		12.2 ns
p_s	23 %	18.8 %		30.43 %		61 %
τ_l	1445 ns	1260 ns	1420 ns	1375 ns	1438 ns	1530 ns
p_l	71 %	73.8 %		69.57 %		39 %
τ_{TPB}	12 μs	34 μs	83 μs	209 μs	32 μs	81 μs
p_{TPB}	6 %	7.4 %	14.7 %	28.2 %	14.5 %	5.8 %
τ_{TPB2}	200 ns				171 ns	710 ns
p_{TPB2}	94 %				91 %	63 %

Table 3.2: Main waveform fit parameters measured by us with DarkSide-50 data and compared with other sources. In the first line is the name of the experiment (Our result is of course with DarkSide-50 as DS50) and the source is in the second one.

all sources provide error values, so they are omitted from the table. Additionally, when changing the fit range, even by a small margin, such as extending it to 15 μs and reducing it to 5 μs, due to the high correlation between parameters the values change from those presented in the table. Therefore, the values indicated in the table should be considered only as indicative. Nevertheless, the correct order of magnitude suggests the correctness of the function used for the fit. The issue probably lies in statistical aspects, and hence, we aim to solve it in the future.

Although concluding absolute nitrogen values based on the results obtained so far is challenging, we can still compare the behavior in different regions and underline their differences. For instance, in the so-called getter-off region, where the getter has been turned off and an increase in single electron measurements is observed, we can evaluate from the waveforms whether there is a nitrogen-related effect that distinguishes this region from others. This is precisely what we will do in the next section by examining correlations between single electrons and nitrogen.

3.2 Nitrogen and argon scintillation

We proceed by revisiting the fit conducted in the previous section and compare τ_l and p_l near the getter-off region with the number of single electrons. Regarding the event selection criteria for the scattering events used in the fit, they are the same as in the previous section. Refer to [80] for the discussion about single electrons. By doing so, we obtain the graph depicted in Figure 3.7.

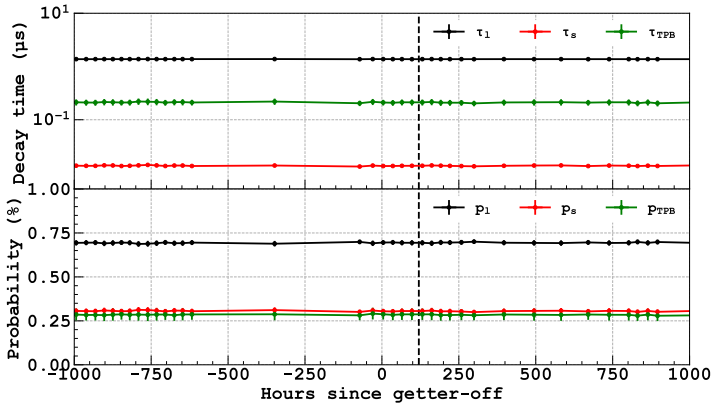

Figure 3.7: Triplet, singlet, and TPB lifetimes and amplitudes near the getter-off region as a function of time, were obtained as results of the fits of groups of DarkSide-50 waveforms. The dotted line corresponds to getter-on, that is when the number of single electron events starts decreasing.

By performing the weighted mean of these three parameters before, during, and after the Getter-off we obtain the following results 3.3.

	Before Getter-off	Getter-off	After Getter-off
SE Rate	0.0403 ± 0.0006 Hz	0.331 ± 0.001 Hz	0.0409 ± 0.0006 Hz
τ_l	1.375 ± 0.005 μs	1.375 ± 0.008 μs	1.375 ± 0.001 μs
p_l	0.694 ± 0.003	0.695 ± 0.005	0.6958 ± 0.0006
τ_s	0.01368 ± 0.00008 μs	0.0136 ± 0.0001 μs	0.01367 ± 0.00002 μs
p_s	0.306 ± 0.003	0.305 ± 0.005	0.3042 ± 0.0006
τ_{TPB}	213 ± 5 ns	212 ± 9 ns	209 ± 1 ns
p_{TPB}	0.285 ± 0.006	0.29 ± 0.01	0.282 ± 0.001

Table 3.3: Average of the fit parameters before, during, and after the getter-off region calculated from figure 3.7.

Furthermore, the fact that both τ_l and p_l do not change in correspondence with the Getter-off is also confirmed using different restrictions on S1, and different fit ranges. The following results are reported:

1. 20000>S1>5000 SE
2. 5000>S1>3000 SE
3. 3000>S1>1000 SE

4. 1000>S1>100 SE

Despite having different values of τ_l and p_l no significant difference is present about the Getter-off, the results are in graphs 3.8, and the weighted average of the fit parameters before, during, and after the getter-off region is in tabular 3.4, 3.5, 3.6, and 3.7.

Parameters	Before	During	After
τ_l	1.31 ± 0.01 μs	1.31 ± 0.02 μs	1.310 ± 0.002 μs
p_l	0.712 ± 0.006	0.71 ± 0.01	0.712± 0.002
τ_s	0.0148 ± 0.0002 μs	0.0148 ± 0.0003 μs	0.01473 ± 0.00004 μs
p_s	0.288 ± 0.007	0.29 ± 0.01	0.288± 0.002
τ_{TPB}	180 ± 20 ns	180 ± 30 ns	175 ± 3 ns
p_{TPB}	0.21 ± 0.02	0.21 ± 0.03	0.211 ± 0.004

Table 3.4: Same as 3.3 with 10000>S1>5000 PE

Parameters	Before	During	After
τ_l	1.33 ± 0.01 μs	1.33 ± 0.02 μs	1.334 ± 0.002 μs
p_l	0.691 ± 0.006	0.69 ± 0.01	0.692± 0.001
τ_s	0.0142 ± 0.0001 μs	0.0142 ± 0.0002 μs	0.01421 ± 0.00003 μs
p_s	0.309 ± 0.006	0.31 ± 0.01	0.307± 0.001
τ_{TPB}	210 ± 10 ns	210 ± 20 ns	208 ± 3 ns
p_{TPB}	0.27 ± 0.01	0.27 ± 0.02	0.267 ± 0.003

Table 3.5: Same as 3.3 with 5000>S1>3000

Parameters	Before	During	After
τ_l	1.35 ± 0.01 μs	1.35 ± 0.02 μs	1.352 ± 0.002 μs
p_l	0.701 ± 0.005	0.70 ± 0.01	0.703± 0.001
τ_s	0.0139 ± 0.0001 μs	0.0138 ± 0.0003 μs	0.01382 ± 0.00003 μs
p_s	0.299 ± 0.005	0.30 ± 0.01	0.297 ± 0.001
τ_{TPB}	190 ± 10 ns	190 ± 20 ns	187 ± 2 ns
p_{TPB}	0.26 ± 0.01	0.26 ± 0.02	0.257± 0.003

Table 3.6: Same as 3.3 with 3000>S1>1000

Then we tried to change the fit range, always making sure to avoid overlapping with S2, so we considered back S1 between 100 and 20000 PE and changed the fit range. In the previous case, it was from 0 μs to 10μs, then we tried in 3.9 to repeat the same calculations from 0 μs to 5μs and from 0 μs to 15μs. The weighted average of the fit parameters is in the tabular 3.9, and 3.8

This underlines how, although the measured fit parameters may lack reliability due to the reasons explained in the previous section, there are no significant differences observed in waveform characteristics before, during, and after the getter-off period. Regardless of the effectiveness of the fit, any substantial increases in nitrogen concentration during the getter-off period would have been expected to manifest as differences in the S1 waveform, particularly in the component related to the argon scintillation triplet, which, however, has not been observed. Hence, it is reasonable to deduce that neither nitrogen nor oxygen (due

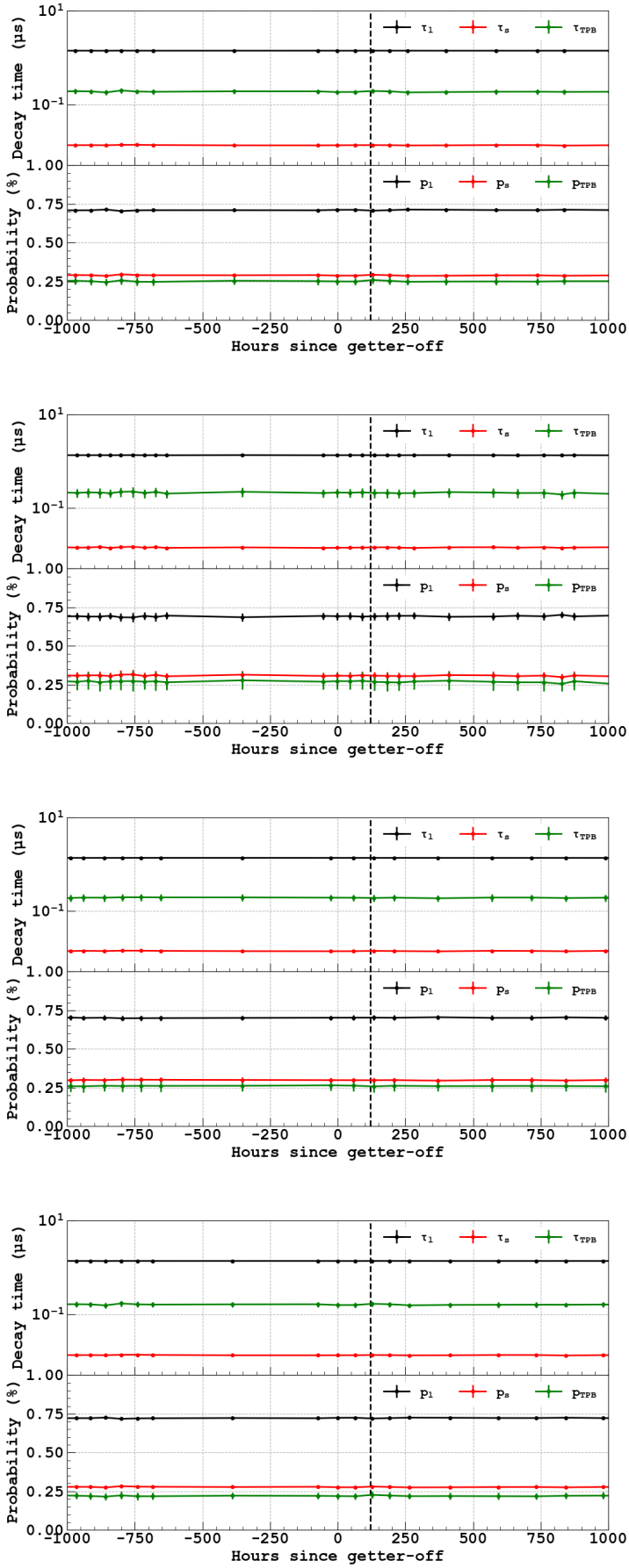

Figure 3.8: The same as in 3.7. From top to bottom. 20000>S1>5000 PE, groups of 5000 waveforms; 5000>S1>3000 PE, groups of 5000 waveforms; 3000>S1>1000 PE, groups of 50000 waveforms; 1000>S1>100 PE, groups of 50000 waveforms.

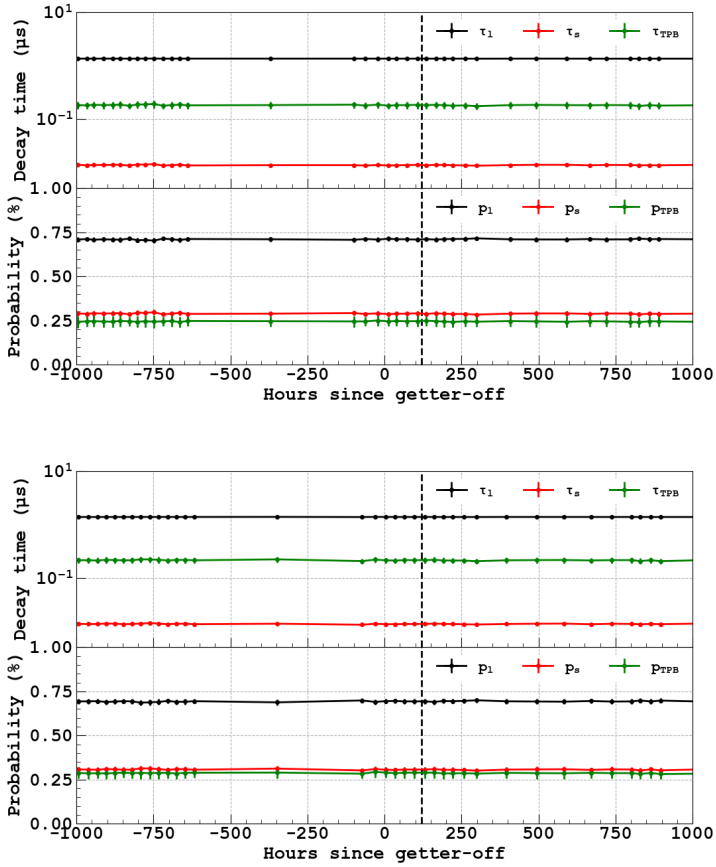

Figure 3.9: The same as in 3.7. Top: fit range from 0 to 5 μs, Bottom: fit range from 0 to 15 μs

Parameters	Before	During	After
τ_l	1.358 ± 0.006 μs	1.36 ± 0.01 μs	1.359 ± 0.001 μs
p_l	0.722 ± 0.003	0.723 ± 0.004	0.7224± 0.0006
τ_s	0.01337 ± 0.00009 μs	0.0133 ± 0.0002 μs	0.01336 ± 0.00002 μs
p_s	0.278 ± 0.003	0.277± 0.004	0.2776 ± 0.0006
τ_{TPB}	161 ± 6 ns	160 ± 10 ns	16± 1 ns
p_{TPB}	0.220 ± 0.007	0.22± 0.01	0.220 ± 0.001

Table 3.7: Same as 3.3 with 1000>S1>100

Parameters	Before	During	After
τ_l	1.338 ± 0.005 μs	1.337 ± 0.008 μs	1.339 ± 0.001 μs
p_l	0.710 ± 0.003	0.711 ± 0.004	0.7116± 0.0006
τ_s	0.01361 ± 0.00007 μs	0.0136 ± 0.0001 μs	0.01358 ± 0.00002 μs
p_s	0.290 ± 0.003	0.289 ± 0.004	0.2884 ± 0.0006
τ_{TPB}	181 ± 5 ns	179 ± 9 ns	178 ± 1 ns
p_{TPB}	0.245 ± 0.006	0.25 ± 0.01	0.243 ± 0.001

Table 3.8: Same as 3.3 with fit range from 0 to 5 μs

to electron lifetime analysis) is present in significant quantities during the getter-off period, leading us to dismiss the hypothesis that single electrons are caused by the presence of such impurities, following the findings in [61] and the graphs presented in Figure 3.1.

Considering the aforementioned discussions and the findings, we can state that the observed rise in the single electron rate during the getter-off period is not causally related to an increase in nitrogen contamination of the liquid argon beyond 1 ppm level. Nevertheless, based on this analysis alone, we cannot definitively reject the possibility of a correlation between the single electron rate and nitrogen contamination below this threshold.

Parameters	Before	During	After
τ_l	1.377 ± 0.005 μs	1.376 ± 0.008 μs	1.376 ± 0.001 μs
p_l	0.693 ± 0.003	0.694 ± 0.005	0.6950± 0.0006
τ_s	0.01368 ± 0.00006 μs	0.0136 ± 0.0001μs	0.01365 ± 0.00002 μs
p_s	0.307 ± 0.003	0.306 ± 0.005	0.3050 ± 0.0006
τ_{TPB}	215 ± 5 ns	213 ± 8 ns	210 ± 1 ns
p_{TPB}	0.287 ± 0.006	0.29 ± 0.01	0.284 ± 0.001

Table 3.9: Same as 3.3 with fit range from 0 to 15 μs

Chapter 4

The Aria project and the cryogenic distillation

In this chapter, we will delve into the principles of cryogenic distillation and distillation columns 4.1. Subsequently, we will introduce various equilibrium concepts 4.1.1, leading to the equations that describe distillation columns 4.3 using rigorous and short-cut methods 4.3.1, 4.3.5. Furthermore, we will discuss the Seruci-0 and Seruci-1 distillation columns of the Aria project 4.4, along with the instruments we will use in the following chapters to conduct simulations 4.5.

4.1 Criogenic distillation

Distillation is an ancient process involving the separation of different elements by exploiting the fact that they have different boiling temperatures. Specifically, by reaching a temperature typically intermediate between the boiling temperatures of the two materials under consideration (T_1 and T_2), or more precisely, being at a temperature denoted as T^* such that $T_1 > T^* > T_2$, we expect that the vapor formed will have a higher concentration of the material with the lower boiling temperature, referred to as material 2. The movement of the vapor and liquid leads to a separation between materials 1 and 2. Often, this process needs to be repeated, requiring the use of a condenser above the distillation column and a reboiler below it. This ensures that the vapor, after condensing back to a liquid state, returns to the column, while the denser liquid transforms into vapor, moves upwards, and repeats the process. This results in extracting a significantly higher concentration of the lighter material (or more accurately, the one with a higher boiling point) from the top of the column, while the other material is extracted from the bottom. The situation becomes more complex when dealing with more than two components to be separated; however, the principle remains the same. In this case, it is referred to as multicomponent distillation.

To effectively quantify the separation capability of our distillation instrument, which we will refer to as the column, it is necessary to define a fundamental quantity, separation, which is the ratio between the concentration of the lighter material extracted from above and the concentration of the heavier material extracted from below. If the separation factor, denoted as S, is equal to 1, then the column is not effectively separating the components. As S increases, the separation capacity of the column also increases accordingly. Therefore, it is an extremely useful quantity for comparing different techniques and instruments in the

field of distillation. More formally, we define the separation as follows [104]:

$$S = \frac{x_{2,D}}{x_{1,D}} \cdot \frac{x_{2,B}}{x_{1,B}} \tag{4.1}$$

Where $x_{i,D-B}$ indicates the molar concentration of element i in (number of moles of element i divided by the total number of moles) of the gas extracted from the top T or bottom B) In the case of only two elements, we can refer always to the lighter elements when defining the concentration (as the concentration of the other element is $1 - x_i$), thus the separation becomes [104]

$$S = \frac{x_D}{1 - x_D} \cdot \frac{1 - x_B}{x_B} \tag{4.2}$$

We expect that, in general, the separation depends on both the operational conditions of the column (which contains various factors that we will discuss in detail later, including column dimensions, operating pressure, amount extracted, etc.) and, of course, the materials to be separated. Generally, the closer the boiling temperatures, the more challenging to separate two materials it is, resulting in a lower separation at the same operating conditions. For example, as we will see in more detail in the upcoming chapters, separating ^{39}Ar from ^{40}Ar is significantly easier compared to separating ^{38}Ar or even ^{39}Ar. In other words, the separation, under the same column conditions, is greater for ^{36}Ar compared to the other cases [105]. This occurs because, in the case of isotopes, the greater difference in mass translates into a larger difference in boiling temperature, thus providing a greater capacity for separation through distillation. This aspect is fundamental in the design of the column. To overcome the challenge of a small temperature difference in boiling points, one can design a taller column or implement other modifications to enhance the distillation process. The parameter that effectively quantifies the "easiness" with which two elements can be separated by distillation is called *volatility*. It is equal to 1 in the limiting case of two completely identical materials that are not separable and increases as the elements become easier to separate [104].

4.1.1 Vapor-Liquid equilibrium

First, we define the K-value K_i of gas as the ratio between the mole fraction of the i component in the liquid and gas phases. In general, the K-value depends on temperature, pressure, and composition *volatility*. The higher the value of K, the more the component tends to exist in the vapor phase. If K is less than one, it tends to stay more in the liquid phase. On the other hand, if K is equal to 1, it should be equally distributed between the vapor and liquid phases. Starting from K_i and K_j respectively of elements i and j in the mixture we define the relative volatility between them as follows:

$$\alpha_{i,j} = \frac{K_i}{K_j} \tag{4.3}$$

By definition, the component i (in the numerator of the previous equation) represents the most volatile element, that is the one for which the vapor phase is significantly favored and, consequently, the one with a higher value of K. It follows that the relative volatility cannot be less than 1. In the case of only two elements we expect:

$$K_i = \frac{y_i}{x_i} \tag{4.4}$$

and

$$K_j = \frac{1 - y_i}{1 - x_i} \tag{4.5}$$

where x_i and y_i are the molar fractions of element i in the liquid and gas phases respectively. By using 4.3, 4.4 and 7.4 we find

$$\alpha_{i,j} = \frac{y_i(1 - x_i)}{x_i(1 - y_i)} \tag{4.6}$$

where i can be omitted. From this, we derive

$$\boxed{y_i = \frac{\alpha_{i,j} x_i}{1 + (\alpha_{i,j} - 1)x_i}} \tag{4.7}$$

This equation (4.7) is fundamental as it represents the vapor-liquid equilibrium in a mixture

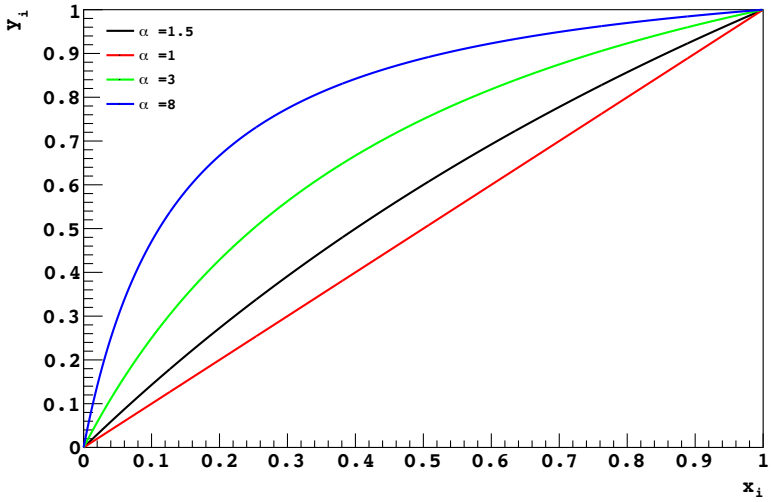

Figure 4.1: Vapor-liquid equilibrium plot used as an example (no real case). Different curves correspond to different values of the relative volatility. [106]

and is plotted as an example for different values of the relative volatility in 4.1. Here, the curves represent the correspondence between the liquid and gas phase molar fractions at the liquid-vapor equilibrium, specifically for the lighter component of the two present in the mixture. The fact that for $\alpha > 1$, there exists a vapor molar fraction, y_i, corresponding to a liquid molar fraction, x_i, such that $y_i > x_i$, indicates that the use of distillation to convert the lighter component from liquid to gas results in an increase in its concentration from x_i to y_i. This increase is greater for higher values of alpha, indicating a higher separation capacity between the two components. Conversely, the operation is reversed for the heavier material, which accumulates during the transition from the gas phase to the liquid phase. For example if $\alpha = 1.2$ to $x_i = 0.5$ correspond $y_i = 0.54$, while we get $y_i = 0.75$ if $\alpha = 3$. What has been discussed so far refers to simpler cases where interactions among the components of the mixture are neglected (an excellent approximation for noble gases). However, in other cases, the curves are not as regular but exhibit a more complex shape. Nonetheless, the study of liquid-vapor equilibrium curves remains crucial even in these cases.

4.2 Relative volatility estimation

In this chapter, we will proceed to estimate this parameter as a function of the column pressure that exists among the various isotopes of argon. This estimation will be achieved through a comparative analysis of various sources and will be useful for understanding the experimental results obtained for the Seruci-0 distillation column and for conducting simulations. As the first step, we will study the most important parameter for characterizing the ability to separate two isotopes, that is the previously mentioned relative volatility. Equations 4.3 and 4.4 define relative volatility as the ratio of the k-values associated with the two components or isotopes under consideration. However, in addition to this definition, volatility can also be defined as the ratio of the logarithms of the liquid f_{liq} and f_{gas} gas phases.

$$\alpha_{i,j} = \ln \frac{f_{liq}}{f_{gas}} \tag{4.8}$$

As defined in [107] and [108]. And they strongly depend on the pressure (and temperature). This happens in an ideal system where the gas follows the ideal gas law, while the liquid obeys Raoult's law [104].
Thus if we consider the partial pressure associated with element i p_i and the total pressure P we would have

$$p_i = y_i P \tag{4.9}$$

Known as Dalton's law, where y_i is always the mole fraction in vapor. For the liquid we consider Raoult's law

$$p_i = x_i p_i^* \tag{4.10}$$

as explained in detail in [104]. p_i^* is the vapor pressure of the pure component. From these equations and the definition of the K-value we find

$$K_i = \frac{y_i}{x_y} = \frac{p_i^*}{P} \tag{4.11}$$

This holds true for ideal systems. For non-ideal cases, we use the partition functions instead of the partial pressures. From these, we derive the general equation for the K-value ([104]).

$$K_i = \frac{y_i}{x_i} = \frac{\Phi_i^L}{\Phi_i^V} \gamma_i \frac{p_i^*}{P} \Psi_i \tag{4.12}$$

Φ_i^L and Φ_i^V are the liquid and vapor fugacity coefficients representing the non-ideality of the fluid considered. Ψ_i is the Poynting factor representing the effect of pressure on liquid fugacity. γ_i is the liquid activity coefficient that is a correction factor for the chemical compositions.

If this holds true for two elements i and j, by using the definition of the relative volatility

$$\alpha_{i,j} = \frac{K_i}{K_j} \simeq \frac{p_i^*}{p_j^*} \tag{4.13}$$

since in a simplified case, we can neglect all the other components.

Therefore, the K-factor depends on the ratio of partial pressures. In turn, the equilibrium vapor pressures depend on temperature, and thus the volatility depends on the system's temperature. In Cox charts [109] it is shown how the vapor pressure of the less

volatile component increases with temperature faster than the other [104]. Therefore, we expect that as the temperature increases, the relative volatility will progressively decrease towards unity. On the other side, if we decrease the temperature, the volatility will increase, alongside our ability to separate the components.

As explained in [104], as the saturation temperature increases, so does the pressure. Therefore, it can be considered that both pressure and temperature affect relative volatility in the same manner. In general, the following relationship holds between the two:

$$T \simeq P^q \tag{4.14}$$

where q is a factor usually from 0.08 to 0.11.

Another important parameter that affects relative volatility is composition. Therefore, for example, when studying nitrogen and oxygen, the ratio between the two components changes the relative volatility even at the same temperature and pressure. In particular, the terms that we have neglected so far in equation 4.12 come into play, specifically γ_i, as there are cases where the system requires heat input to effectively mix the two elements. This effect is not present when considering different isotopes of the same element, as dealing with the distillation of argon isotopes.

An effective method for estimating partial pressures involves the use of the Antoine equation [110]. This equation is an approximation for chemically pure fluids and is derived from the Clapeyron equation. It is particularly useful for determining partial pressures based on temperature and for examining how volatility changes with the temperature of the column. It is particularly useful as it is used by simulation software programs such as Hysys to calculate relative volatility.

$$\ln P[kPa] = a + \frac{b}{T[K] + c} + d \ln T[K] + eT[K]^f \tag{4.15}$$

Square brackets indicate the unit of measurement to be used, the empirical parameters a, b, c, d, and e are employed according to the nomenclature specified by Hysys.

In scientific literature, the relative volatility between two isotopes of a given element (often the most common or those frequently targeted for separation) is often known, while the relative volatilities between all other isotopes may not be available. Therefore, it becomes essential to develop a method to calculate, for instance, α_{38-40} or α_{39-40} from α_{36-40} when dealing with argon. To solve this issue, researchers in [1], [2], and [107] have all used the theoretical equation described in [111].

$$\ln \alpha_{i,j} = \ln \left(\frac{f_{liq}}{f_{gas}}\right)' = \frac{24}{\hbar^2} \epsilon \sigma^2 \frac{m \cdot m'}{\Delta m} \ln \left(\frac{f_{liq}}{f_{gas}}\right) \tag{4.16}$$

Where σ and ϵ are the Lennard-Jones parameters [112] and $\hbar$ is the Plank constant. m and m' are the masses of the two particles we are considering. In [111] they applied a reduced variable fit for the relative volatility as a function of the pressure

$$T' \ln \left(\frac{f_{liq}}{f_{gas}}\right)' = \frac{A}{T'} + B + CT' \tag{4.17}$$

with A=$1.04 \cdot 10^3$, B=$-1.58 \cdot 10^2$, and C=$-2.71 \cdot 10^2$ and T' is a dimension-less normalized temperature. We can find then

$$\ln \alpha_{i,j} = \frac{24}{\hbar^2} \epsilon \sigma^2 \frac{m \cdot m'}{\Delta m} \left(\frac{A}{T'^2} + \frac{B}{T'} + C\right) \tag{4.18}$$

and in [111] it has been experimentally confirmed for isotopes of noble gasses such as ^{20}Ne/^{22}Ne, ^{36}Ar/^{40}Ar, and ^{80}Kr/^{84}Kr.

Thus if we consider the relative volatilities α_{A-B} and α_{C-B} we can write them as

$$\ln \alpha_{A-B} \simeq \frac{m_A m_B}{m_B - m_A} \tag{4.19}$$

and

$$\ln \alpha_{C-B} = \simeq \frac{m_C m_B}{m_B - m_C} \tag{4.20}$$

By performing the ratio we obtain

$$\frac{\ln \alpha_{A-B}}{\ln \alpha_{C-B}} = \frac{m_A}{m_C} \frac{m_B - m_C}{m_B - m_A} \tag{4.21}$$

Where we consider $m_B > m_A$ and $m_B > m_C$.

We can finally demonstrate the expression we used in the previous chapters for argon 5.8. By using 4.21 we can write

$$\frac{\ln \alpha_{38-40}}{\ln \alpha_{36-40}} = \frac{38}{36} \frac{40 - 36}{40 - 38} = \frac{19}{9} \tag{4.22}$$

Regarding the true value of the volatility between isotopes 36 and 40 (from which we start

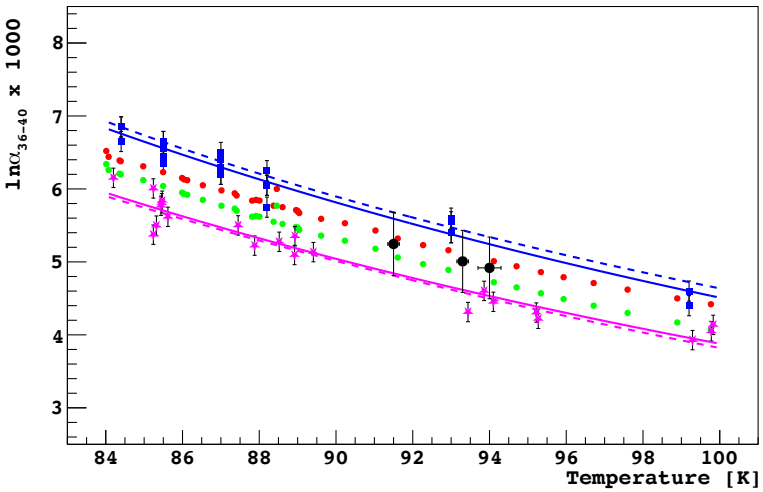

Figure 4.2: Relative volatility α_{36-40} as a function of the temperature. Blue point refers to [113], purple to [114], and green to [115]. The dotted line corresponds to the interval of accepted volatility as a function of the pressure chosen for our calculations. [2]

the calculation of the others), there are several sources, each of which provides a slightly different result. Therefore, an intermediate value has been chosen, along with an error band that comprehends the results from each source.
Other values of alpha found in this thesis are from the following sources [116], [117], and [118]. According to [119] we expect the relative volatility to follow the next formula

$$\ln \alpha_{36-40} = \frac{A}{T^2} + B \tag{4.23}$$

which is a simplified version of the one we saw in the previous lines by [111]. In 4.2 is the data from different sources. Between the dotted line is the acceptance range of the values of α_{36-40} we have chosen to include all the different sources.

From this, we found in region A for T=93.3 K $\ln \alpha_{36-40} = (5.1 \pm 0.4)10^{-3}$, in region B for T=91.5 K $\ln \alpha_{36-40} = (5.2 \pm 0.4)10^{-3}$, and in C for T=94.0 K $\ln \alpha_{36-40} = (4.9 \pm 0.4)10^{-3}$ and multiplying each by 9/19 we get the values for $\ln \alpha_{38-40}$ as written in the previous chapters.

4.3 Equations of a distillation column

To continue studying the operation of distillation columns, it is necessary to introduce the concept of an ideal stage. Summarizing what is described in [104], the conditions for a stage (which represents a component of a distillation column and functions as a single distillation column itself) to be defined as ideal are as follows:

1. It must operate in a steady state and produce both liquid and vapor.
2. The vapor leaving the stage must be in equilibrium (as described previously) with the liquid doing the same.
3. The vapor and liquid entering a stage must mix perfectly.

Distillation columns can be made of multiple stages, essentially multiple columns stacked on top of each other. However, modern columns, are instead continuous and contain a material called packing, which aims to increase the contact surface area between the fluids entering for distillation and characterize the column itself. The packing essentially allows the column to behave as if it were composed of numerous theoretical ideal stages (since they do not exist), the number of which depends on the column's dimensions and the chosen packing. Therefore, the parameter known as HETP (Height of Theoretical Plate) is crucial, representing the height of a theoretical stage in the column. It is related to the column height, h, as follows:

$$\text{HETP} = h/N \tag{4.24}$$

Where N is the number of theoretical stages of the column. In general, stages in a distillation column can be either stripping or rectifying. For each stage, there is enriched vapor leaving from the top and depleted liquid leaving from the bottom. If the compressive balance favors the vapor, it is a rectifying stage; otherwise, it is a stripping stage. The liquid that circulates inside the column is referred to as reflux. In the common case of a column with a single feed, where the input mixture is introduced at a single point, the stages above the feed zone are rectifying stages, while those below are stripping stages. Generally, if the primary objective is to isolate the lighter component through distillation, the feed is preferentially placed towards the bottom of the column to have more rectifying stages available for purification. Conversely, if the aim is to enrich the heavier component, the feed is placed towards the top. A schematic representation of a stage is shown in 4.3.
Where V_n is the vapor mass flow (typically expressed in kg/h) leaving the n-th stage (V_{n+} is leaving the n-th+1 stage to reach the n-th), L_n is the liquid mass flow. If we are inserting the mixture in this stage we also have F_n as the inlet mass flow. For each of these stages, we can apply the equations of mass conservation 4.25, mole number conservation 4.26, energy conservation 4.27, and the liquid-vapor equilibrium relationship 4.28 as explained in [104].

$$F_n + V_{n+1} + L_{n-1} = V_n + L_n \tag{4.25}$$

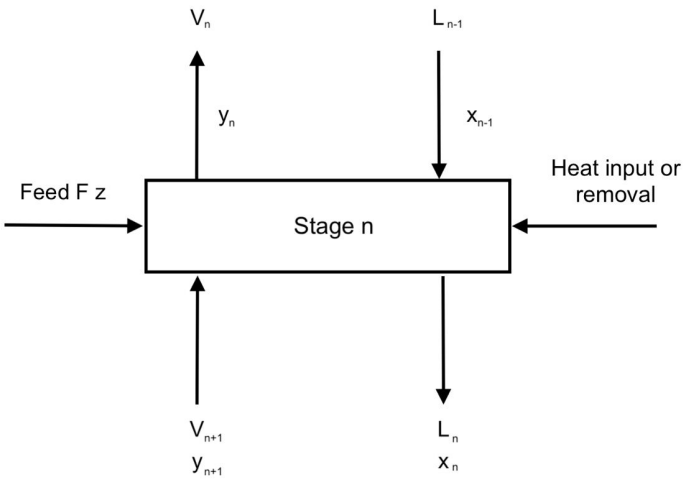

Figure 4.3: Schematic representation of a theoretical stage of a generic column. [104]

$$F_n z_n + V_{n+1} y_{n+1} + L_{n-1} x_{n-1} = V_n y_n + L_n x_n \tag{4.26}$$

$$\Delta H_n + F_n H_{f,n} + V_{n+1} H_{V,n+1} + L_{n-1} H_{L,n-1} = V_n H_{V,n} + L_n H_{L,n} \tag{4.27}$$

$$y_n = K x_n \tag{4.28}$$

That set of equations is true for every stage of the column.

From the top we extract the mass flow D and from the bottom, we extract B (called W in some references). By convention, the stages of a column are counted from the top. In particular, the vapor, denoted as V_1, leaving the first stage at the top of the column, is partially reinserted into the column after passing through a condenser, becoming the liquid L_0 reentering the first stage of the column. Another portion is instead distilled and referred to as D. Similarly, the liquid L_{N+1} partially returns to the bottom stage in the form of vapor after passing through the reboiler, and another portion is extracted to form B. The fraction of liquid and vapor reintroduced into the column determines its reflux.

$$R = \frac{L_0}{D} \tag{4.29}$$

$$S = \frac{V_{N+1}}{B} \tag{4.30}$$

Here, R represents the reflux for rectifying, and S for stripping. When nothing is extracted (or when what is extracted is significantly less than the flow in the column), it is said to be in a condition of total reflux. A general scheme of a distillation column is in 4.4. Solving the behavior of a column means solving the system of equations mentioned earlier for each stage of the column. Therefore, in the simplified case of only two components separate, a system of $4 \cdot N$ equations must be solved for an equal number of unknown factors (N being the number of stages in the column). Using specific software such as Aspen HYSYS® [121], it is easy to solve these equations when the number of stages is relatively low. However, beyond 2000 stages (equivalent to 8000 equations in 8000 unknowns), Aspen HYSYS® significantly slows down, and beyond 5000 stages, it becomes impossible to use this program for distillation simulations. It is therefore essential to seek alternative solutions that can:

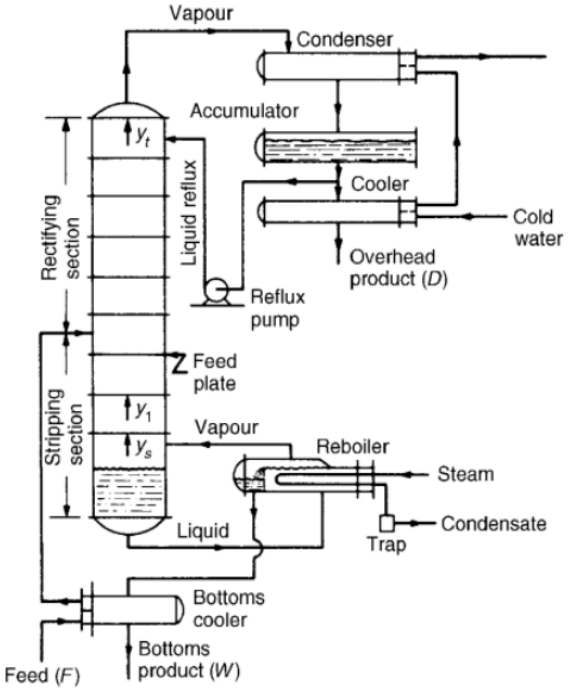

Figure 4.4: Schematic representation of a distillation column. Note that here the bottom product is indicated as W instead of B. It should be noted that the argon circuit may vary since the first idea was to transport the argon in liquid form. However, it was later decided to use gas skids for transporting argon in gaseous form. [120]

1. Avoid considering more than two component elements simultaneously. This is because otherwise, we would be dealing with the so-called multicomponent distillation, which heavily impacts simulation software. The conditions under which only specific components can be studied while essentially ignoring the others will be discussed in the next chapters.

2. Simplify the equations by treating multiple stages as a single block. Under certain conditions, this is possible and forms the basis of some shortcut methods.

4.3.1 Short-cut methods

The most important assumption that needs to be made is the *Constant Molar Overflow*. It is relevant to various shortcut methods we will discuss in this chapter, such as McCabe-Thiele (MCT) [122] and Fenske-Underwood-Gilliland (FUG) [124]. This assumption is based on the fact that the material inside the column has a constant heat of vaporization and that other sources of heat, such as those due to vapor-liquid mixing, have negligible effects. As emphasized by [104], this assumption is particularly effective when the materials being mixed have similar masses (as is the case with different isotopes of the same element). Other important assumptions for shortcut methods include the separation occurring at constant pressure, and the input mixture mixing with the fluid inside the column before undergoing separation. Furthermore, to simplify the equations describing the column, it is assumed that there are only two extraction points (above and below the column) and a single feed entry point.

As described by [104] the constant molar overflow allows us to say that the liquid flux inside the column is the same for every stage of the column

$$L_0 = L_1 = ... = L_N \tag{4.31}$$

$$V_0 = V_1 = ... = V_N \tag{4.32}$$

We will denote L and V for the rectifying section and L' and V' for the stripping section. 4.25 and 4.26 can be simplified as follows

$$V = L + D \tag{4.33}$$

$$Vy_n = Lx_n + Dx_D \tag{4.34}$$

Where x_D is the concentration of the lighter element getting distilled from the top.

$$V' = L' - B \tag{4.35}$$

$$V'y_n = L'x_n - Bx_B \tag{4.36}$$

Where x_D is the concentration of the lighter element extracted and distilled from the bottom.
4.34 and 4.36 are the basis for the MCT method. The total mass balance equation is

$$F = B + D \tag{4.37}$$

That together with 4.33 and 4.35 gives us

$$V' - V = (L' - L) - F \tag{4.38}$$

while reflux become

$$R = \frac{L}{D} \tag{4.39}$$

$$S = \frac{V'}{B} \tag{4.40}$$

for rectifying and stripping the region

4.3.2 McCabe-Thiele method

MCT (McCabe-Thiele) is a graphical method used to describe, simulate, and make predictions about the behavior of a distillation column. It is based on the representation of a series of curves, as in 4.5. Further details are in [104].

1. Equilibrium curve: A curve that represents the vapor-liquid equilibrium and, as previously discussed, is essential for achieving separation by continuously transitioning between equilibrium states. It is described by the equation 4.7 in ideal cases.

2. Diagonal $x_n = y_{n+1}$: A diagonal line at a 45-degree angle, used for graphical purposes.

3. Component balance lines: Equations 4.34 and 4.36 can be written as follows:

$$y_{n+1} = \frac{L}{V}x_n + \frac{D}{V}x_D \tag{4.41}$$

$$y_n = \frac{L'}{V}x_{n-1} - \frac{B}{V'}x_B \tag{4.42}$$

and represent the points where component balance equations are fulfilled in rectifying and stripping sections. From equations 4.33 and 4.35 and since by definition B and D are always positive we expect L<V and L'>V'. Thus the slope of the rectifying section is always smaller than 1 while it is always bigger than 1 for the stripping.

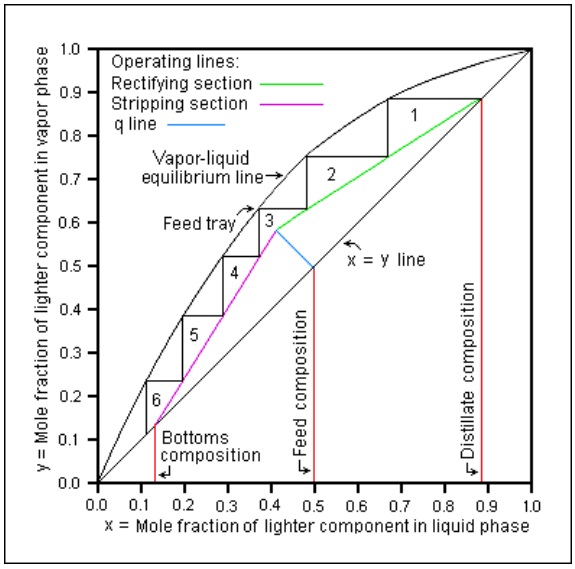

Figure 4.5: Copyright (C) 2000,2001,2002 Free Software Foundation, Inc. 51 Franklin St, Fifth Floor, Boston, MA 02110-1301 USA. [125]. MCT example.

4. We look for the intersection between the 45-degree diagonal and 4.41 and 4.42. The component balance for rectifying the section becomes

$$x_n = \frac{L}{V}x_n + \frac{D}{V}x_D \tag{4.43}$$

$$x_n = \frac{D}{V-L}x_D \tag{4.44}$$

Adding 4.33 we finally get

$$x_n = y_{n+1} = x_D \tag{4.45}$$

For the stripping section, we can repeat the same procedure and obtain

$$x_{n+1} = y_n = x_B \tag{4.46}$$

Thus we obtain both for vapor and liquid the concentration extracted from the top and the bottom of the column.

5. We then look for the intersection between the two component equilibrium lines. Putting 4.34, 4.36, and the equation of the overall component balance together

$$Fz = Dx_D + Bx_B \tag{4.47}$$

where z is the concentration of the lighter element in the feed. We get the following:

$$(V - V')y_i = (L - L')x_i + Fz \tag{4.48}$$

Then we define another important parameter q such that

$$q = \frac{L' - L}{F} \tag{4.49}$$

together with 4.38 we can write is also as

$$q = \frac{V' - V}{F} + 1 \tag{4.50}$$

From 4.48 and the last two equations, we can easily obtain the following expression

$$y_i = \frac{q}{q-1}x_i - \frac{z}{q-1} \tag{4.51}$$

Where is $x_i = z$ we can get $y_i = z$. Thus it is a line going from the point where stripping and rectifying component balance lines are intercepting to the point (z,z) that is the feed composition 4.5.

6. To understand the physical idea behind q we look at the slope of the q-line. $q/(q-1)$ can be rewritten using equations 4.49 and 4.50 and we get

$$qF = L' - L \tag{4.52}$$

L'-L is the difference between liquid flow in stripping and rectifying sections, that is, due to mass conservation, the liquid mass flow that comes from the feed. If F is the total feed mass flow, it follows that q is the fraction of the feed mass flow that is liquid. 1-q on the other hand will be the fraction of the feed that is vapor. So if q is equal to 1 (the q-line on the plot will be a line parallel to the y-axis) we have only liquid coming from the feed. If q=0 (the q-line is parallel to the x-axis) we have only vapor.

One stage of a distillation column, as mentioned earlier, uses the transition from the liquid to the gas phase to enrich the lighter component exploiting the liquid-vapor equilibrium. Therefore, from a graphical perspective, the operation performed by a stage of a column can be represented by two lines: one horizontal and one vertical. These lines connect the component equilibrium lines to the pressure-vapor equilibrium line and vice versa. A vertical line represents an increase in the fraction of the lighter component in the vapor while keeping its concentration in the liquid constant, while a horizontal line represents an increase in the concentration of that component in the liquid without changing its concentration in the gas. These two effects together represent the behavior of a stage in the column. As shown in 4.5, the column's ability to achieve separation by passing through multiple theoretical stages is represented by this series of horizontal and vertical lines. The McCabe-Thiele graphical method involves starting from the concentration extracted from the bottom, x_B, and drawing a series of vertical and horizontal lines equal to the number of stages in the column. This allows us to determine the concentration extracted from the top, x_D. Alternatively, if x_B and x_D are known, the number of stages in the column can be determined. Stages whose lines are represented below the q-line constitute the stripping stages, while those above it represent the rectifying stages. Of course, since these are theoretical stages, they can also be not integers, as shown in the example figure.

4.3.3 Reflux and total reflux condition

Often, computer-based techniques for studying distillation columns use the equations of equilibrium lines by incorporating the reflux ratio, R. Specifically, by employing equations 4.39 and 4.40 and applying them to the equilibrium lines of the components in the rectifying and stripping sections, the following results can be obtained.

$$y_{n+1} = \frac{R}{R+1}x_n + \frac{x_D}{R+1} \tag{4.53}$$

$$y_{n+1} = \frac{1+S}{S}x_{n-1} - \frac{x_B}{S} \tag{4.54}$$

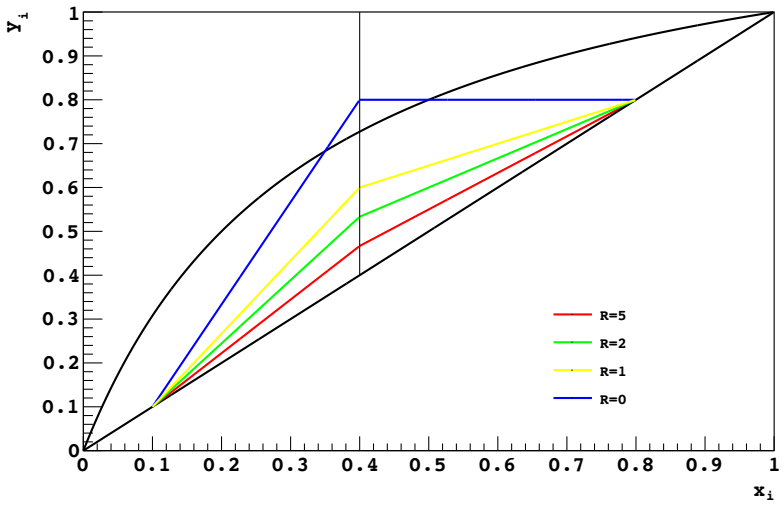

Figure 4.6: Example of the MCT scheme for different reflux ratios ranging from 0 to 5.

As the reflux ratio increases, as seen in 4.6, the component balance line gradually flattens and approaches the 45-degree line (as R tends to infinity). The number of stages required for separation will strongly depend on R: in general, decreasing R will increase the number of stages needed. The lines representing the stages using MCT are formed only in the region below the vapor-liquid equilibrium line and above the component balance lines. Therefore, if (as in the case shown in the figure for R=0) one goes outside the area bounded by the vapor-liquid equilibrium curve, separation is no longer possible. Thus, there exists a minimum value of reflux ratio, denoted as R_{min}, below which separation is only possible with an infinite number of stages. At the minimum reflux condition, the feed occurs on the xy plane at the intersection between the q-line and the two-component balance lines for stripping and rectifying. Graphically, R_{min} can be easily determined by extending the q-line until it intersects the vapor-liquid equilibrium curve. At this point, the line connecting the intersection to the upper extraction point (x_d,x_d) can be found. The slope of this line will be $R_{min}/(R_{min}+1)$. The minimum reflux condition is unfavorable because even approaching it significantly increases the number of stages required to operate the column. In contrast, there is the total reflux condition, where the reflux tends to infinity. This occurs when very little is extracted compared to the flow that returns to the column. An example of this is the runs we conducted with Seruci-0 for the distillation of nitrogen and argon isotopes. In these cases, the objective was not to produce large quantities but rather to extract enough to measure their chemical composition and determine whether separation had occurred or not. In this case, as mentioned earlier, the stripping and rectifying lines will be indistinguishable from the diagonal line x=y. Therefore, in the MCT method, we will only build stages between the equilibrium curves and the 45-degree line. It is evident that in this case, the number of stages required to distill from concentrations x_d to x_b from below is minimized 4.7. The number of stages $N = N_{min}$ when we are in the total reflux condition. As we choose to extract larger flows (thus moving away from the total reflux condition), the number of stages required for a given separation increases. Since the number of stages in an actual column is fixed, the usual choice to be made is whether to move towards the total reflux condition, maximize the separation capacity of the column, or increase production in kg/h, separating less efficiently the different components.

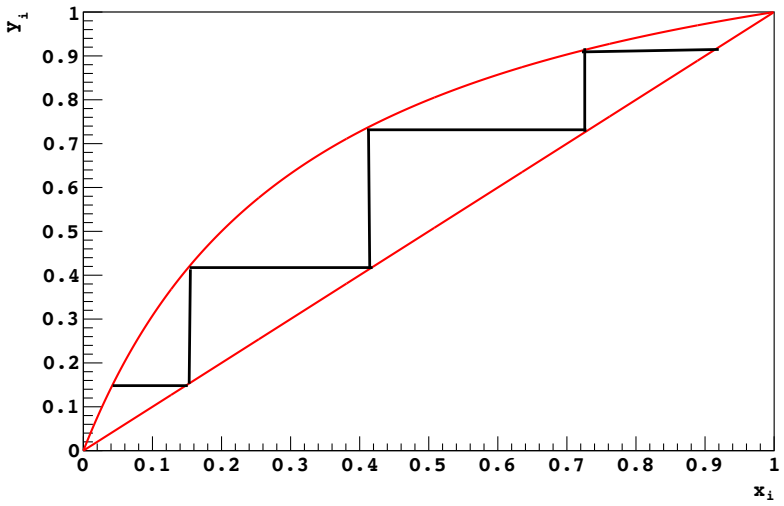

Figure 4.7: Example total reflux with MCT stages.

4.3.4 Fenske Equation

So far, we have established, through the study of MCT graphs, that having a greater number of stages allows us to connect x_D and x_B at greater distances from each other, which means we can achieve a greater separation (referring back to equation 4.2). At the same time, if the relative volatility of the substances we want to separate increases, the size of the vapor-liquid equilibrium curve also increases. This results in larger "jumps" made by the column at each stage, and therefore, with the same number of stages, we expect that an increase in α will also increase the separation capacity of the column. Both of these concepts are quantified by the Fenske equation.

$$\boxed{S = \alpha^{N_{min}}} \tag{4.55}$$

In other terms using 4.2

$$N_{min} = \frac{\ln \frac{x_D}{1-x_D} \cdot \frac{1-x_B}{x_B}}{\ln \alpha} \tag{4.56}$$

Where, of course, the case of total reflux is particularly convenient, as we expect the number of stages to coincide with the minimum number of stages. This equation holds when dealing with only two components, while in the case of multicomponent systems, it should be indicated as follows.

$$N_{min} = \frac{\ln \frac{x_{2,D}}{x_{1,D}} \cdot \frac{x_{2,B}}{x_{1,B}}}{\ln \alpha} \tag{4.57}$$

Where 2 is the lightest and 1 is the heaviest among the elements we want to separate.

4.3.5 FUG method

Another commonly used shortcut method for the description and study of distillation columns is the FUG method. This method involves the use of three equations:

1. The first equation is the Fenske equation described in the previous subsection.

2. The second equation is the Underwood equation, which allows for the calculation of the minimum reflux required for distillation to occur.

$$R_{min} = \frac{\frac{x_D}{z} - \alpha\frac{1-x_D}{1-z}}{\alpha - 1} \tag{4.58}$$

3. The empirical Gilliland equation, which relates the minimum values of R and N to the actual values.

$$\frac{N - N_{min}}{N+1} = 1 - exp(\frac{1+54.4X}{11+117.2X}\frac{X-1}{\sqrt{X}}) \tag{4.59}$$

Where

$$X = \frac{R - R_{min}}{R+1} \tag{4.60}$$

Considering all these 3 equation we have N, N_{min}, R, R_{min}, x_D, x_B, α, z as parameters. Therefore, if we know 5 out of these 8 parameters, we can determine the remaining 3 by using the available 3 equations. Typically, the feed composition (z) and the relative volatility between the components we want to separate are known. In addition to these, assumptions are often made regarding the ratio between reflux and minimum reflux, such as in the case of [107], and an estimation of the number of stages in the column based on the packing and operative conditions is also available. At this point, the conditions are sought for extracting from above or below with a certain concentration (x_D or x_B). This is where the FUG method comes into play, as there are only 3 parameters left to determine: the non-assumed one between x_D and x_B, N_{min}, and R (with the known ratio R_{min}).

4.4 Aria distillation columns: Seruci-0 and Seruci-1

In 4.8, the schematic representation of the Aria plant is shown. The gray area corresponds to a cold box, which is maintained at low temperatures and has limited heat exchange with the surroundings. It is also vacuum-tight. We can identify the column itself, heat exchangers, and cryogenic tanks within this area as well. There are two separate circuits to be considered: one for argon and the other for nitrogen (the latter is for cooling purposes). Specifically, the green pipes are for argon (dark for the liquid phase and light for the gas phase), while the blue pipes are for nitrogen (dark for the liquid phase and light for the gas phase).

Within the column, we can identify two separate processes. The first one is related to distilling argon, including its introduction and removal. The second process involves nitrogen and is aimed at cooling the column and the argon. The nitrogen circuit is the one consuming more energy, so the system was designed to minimize this energy consumption.

The column structure consists of 28 identical modules, each 12 meters tall, weighing 3 tons, and with a diameter of 71 cm. Overall, the column will reach a height of approximately 350 meters. To reuse a decommissioned mining site and to avoid the complications of having such a tall structure above ground, it was decided to construct it underground in the Nuraxi Figus mine, located in Sardinia, Italy. The final module will be only 4 meters tall and will house the reboiler, while the top module will be 9.5 meters tall and will contain the condenser. The aforementioned description regards the under-construction column Seruci-1, whereas the prototype Seruci-0 is made by only 3 modules (including the reboiler and condenser) that will later used for Seruci-1 when the prototype is decommissioned.

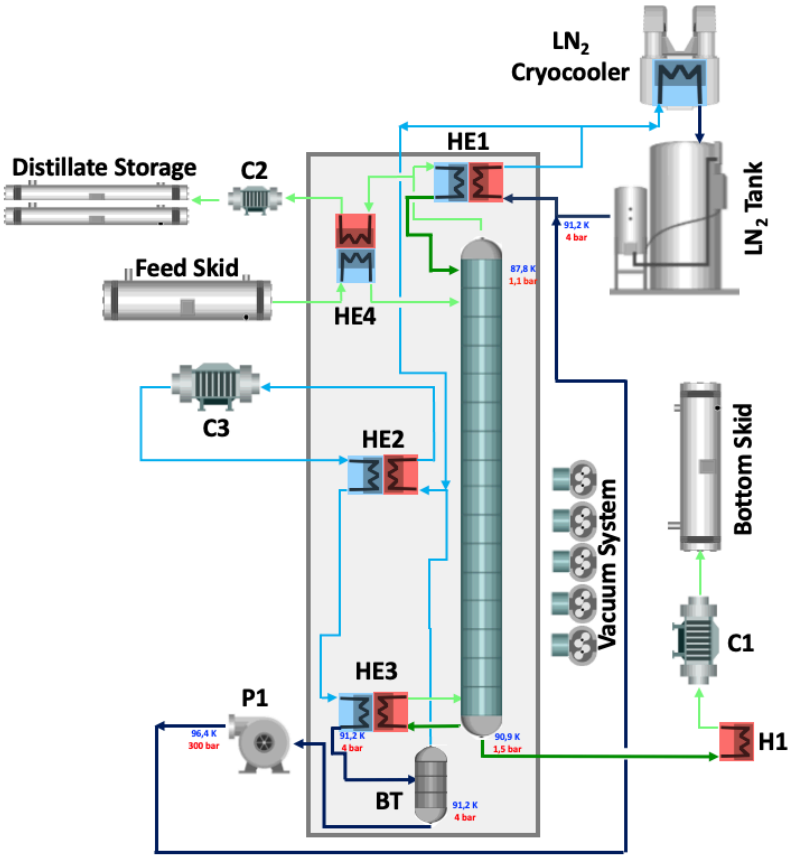

Figure 4.8: Structure and components of the Aria plant [1]. It should be noted that the argon circuit may vary since.

The packing material chosen for Aria, as described in previous chapters, is stainless steel of the Sulzer CY gauze type [126]. According to the manufacturer's specifications, the maximum allowed column flow rate should be around 500 kg/h, considering the density of argon. However, recent measurements in [2] have shown that even with flow rates exceeding 600 kg/h, the column separation has not been compromised. Further details regarding the structure surrounding the column and the successful leak tests conducted on various components can be found in [1].

Another important aspect of the packing material is its correlation with other col-

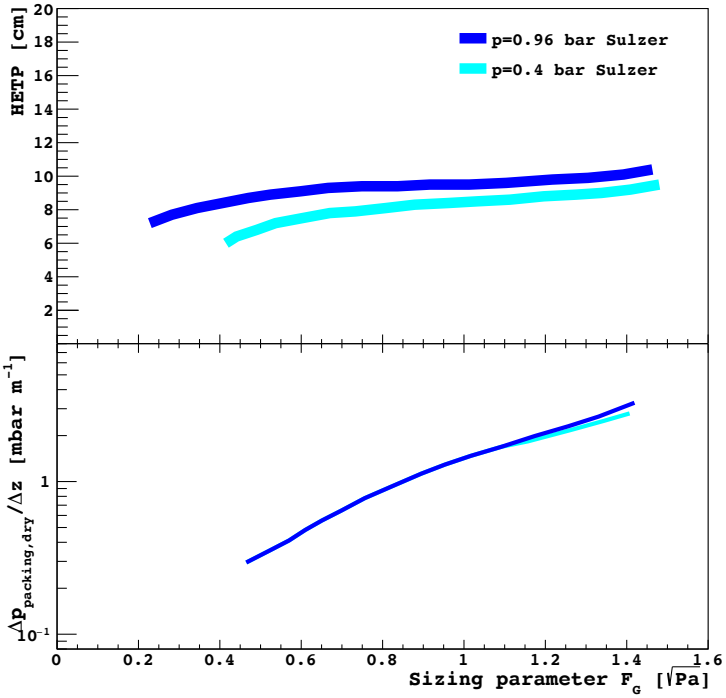

Figure 4.9: HETP and pressure drop as a function of the sizing parameter (related to the flow inside the column). [2]

umn quantities such as HETP and, consequently, with the number of stages. The curves in [1] and [1] (4.9) depict the behavior of pressure drop and HETP as a function of the sizing parameter, which is in turn related to the column flow rate and the density of the gas being distilled. The curves suggest that the HETP is primarily influenced not by the column flow rate (at least within the considered range) but by the pressure. Decreasing the pressure would result in a lower HETP, which, given the same column height, would mean having a greater number of stages and thus enhancing the separation (the previous runs with Seruci-0 were conducted under total reflux conditions, where the number of stages coincided with the minimum number of stages in the Fenske equation). Therefore, it would be advantageous to always operate at lower pressures, increasing both the relative volatility, which depends on pressure and the number of stages. Both terms in the Fenske equation, N_{min} and α, would increase, leading to a significant improvement in separation.
However, in [2] we obtained a different outcome. Three measurements conducted at increasing sizing parameters and different pressures ranging from approximately 1.5 bar to

1.9 bar all yielded the same HETP within the statistical error, indicating no significant difference. This made us question the effectiveness of the curves depicted in 4.9, as these curves were calculated by the Sulzer company using a specific chlorobenzene/ethylbenzene mixture at non-cryogenic temperatures. Furthermore, this result means we don't need to significantly reduce the pressure to improve the separation, which would introduce additional complications such as maintaining the column at a pressure lower than atmospheric pressure.

The sizing parameters are defined as $F_G = \frac{V}{S} * \sqrt{\rho_V}$, where V is the flux inside the column, S is the surface of a section of the packing, and ρ_V is the density of the gas in the vapor phase (argon in our case)

The pressure drop in the column (per unit of packing) is also influenced by the packing material itself. In this case, an analogous trend has been observed, namely an increase in pressure drop with an increase in column flow rate.

4.5 Simulation Software

We used the Aspen HYSYS software [121], developed by Aspen Technology Inc., to conduct comprehensive simulations of our distillation plant. HYSYS is a robust computational tool that enables rigorous calculations for distillation processes. It solves equations about mass, component, energy, and equilibrium balances for each stage of the column. Additionally, HYSYS supports the simulation of multi-component distillation processes, involving three or more components simultaneously. It is important to note, however, that the default HYSYS library does not include isotopes. To overcome this limitation, we incorporated the relevant argon isotopes into the HYSYS library, along with their molecular weights and Antoine equation parameters, Furthermore, we employed the SulcolTM 3.5 software package developed by Sulzer to design structured and random packing. This software facilitated the modeling of hydraulic parameters specific to the distillation column. By providing input properties such as gas and liquid phase density, viscosity, surface tension, as well as the mass flow rates of gas and liquid within the column, Sulcol calculated other column parameters, including pressure drop per unit length and liquid hold-up [1].

Hysys offers the flexibility to choose between shortcut simulation methods (such as the FUG method) or solving systems of numerous equations to rigorously describe the column. In the case of Seruci-0 simulations, dealing with approximately 100 stages, the use of rigorous methods has never been a problem. However, with Seruci-1 (2000-3000 stages) the simulation time has increased drastically.

Additionally, we have considered other cases with highly efficient packings (i.e., with a significantly smaller HETP and, therefore, a higher number of stages for a given column height). In these cases, the number of stages can reach 10-20 thousand, which is too high for performing rigorous simulations with Hysys. To solve this issue, we have either employed shortcut methods or adjusted the value of the alpha parameter, as will be discussed in the chapter dedicated to CO and NO distillation.

Chapter 5

Seruci-0 runs for isotopic distillation

In this chapter, following the description of the operation of a Universal Gas Analyzer 5.1, we will provide a detailed description of the Seruci-0 run 5.2, which allowed us to experimentally separate argon isotopes. Additionally, we will discuss the sampling system that connects the distillation column with the UGA 5.2.1, and discuss the preliminary results of separation, multicomponent 5.2.3 behavior, and asymmetry 5.2.4. Lastly, we will also describe the Seruci-0 run for the distillation of nitrogen isotopes 5.3.

5.1 Mass spectroscopy with the Universal Gas Analyzer

A UGA is an instrument designed to distinguish the various components present in a gas sample. Its primary component is the residual gas analyzer (RGA), which functions as a quadrupole mass spectrometer. The remaining structure of the UGA is designed to ensure that the gas reaches the RGA at the required pressure of approximately 10^{-7} mbar.
The RGA ionizes the gas and separates the ions based on their charge-to-mass ratio (e/m). For each value of e/m, a current signal proportional to the number of ions is generated. This produces a signal as a function of the mass number (spectrum). Calibrating a UGA involves establishing the relationship between the current and the partial pressure of the gas. Once calibrated, the y-axis of the UGA display will indicate pressure in mbar instead of current.
Before reaching the UGA, the sampling gas passes through two capillaries with different inner diameters (1 m and 19 cm). The gas enters the UGA with an inlet flow rate of 20 ml/min and a pressure of approximately 1 atm at the beginning of the second capillary, which is the required pressure by the instrument. Inside the UGA, the bypass valve and turbo pump activate to significantly reduce the gas pressure to the order of 10^{-7} mbar required by the RGA.
Once the gas molecules enter the RGA, they pass through an ionization region. Electron emission from a hot cathode (filament) causes ionization of the molecules, resulting in the production of ions with specific e/m ratios. These ions are then accelerated by an electrostatic lens and directed into a quadrupole. The quadrupole separates the different gases according to their e/m ratios, allowing only particles whose trajectory has a certain radius to reach the next detector. An electrical signal proportional to the number of particles with a specific e/m ratio is recorded. This selection process is made possible by a lens system known as V-Lens^{TM} [127]. The procedure is repeated for different e/m ratios, resulting in the reconstruction of the entire spectrum. Detection is facilitated by a Faraday cup and a Multiplier, which detects and amplifies the charge of the ions.
The UGA also incorporates an internal oven to maintain a constant and stable high

temperature (80°C - 100°C), which ensures accurate gas detection.
In the spectra presented in 5.1, the reciprocal of the e/m ratio is plotted on the x-axis, assuming e = 1. This means that in the case of double ionization, there will be an additional peak for a specific gas. For example, ^{40}Ar exhibits a peak at m = 40 for single ionization and m = 20 for double ionization. Before proceeding with calibration, it is necessary to tune the instrument. The tuning process involves identifying the exact position of each peak in order to account for any offset between the real mass and the peak position. The peaks are then adjusted to align them to the desired mass.
Optimization of several values is required during tuning:

1. Emission current: The current of electrons emitted by the filament, which is directly related to the filament temperature.

2. Electron energy: The accelerating voltage between the filament and the ion source. It determines the energy of the electrons in the ion source.

3. Ion energy: The energy voltage of the ion source and the energy of the emitted ions.

4. Extraction voltage: The voltage for ion extraction in the ion source.

Tuning parameter	Range	Value chosen
Emission	0-5 mA	1 mA
Electron Energy	0-100 eV	40 eV
Ion Energy	0-10 eV	10 eV
Extract	0-130 V	20 V

Table 5.1: UGA tuning parameters. The table also displays the allowed range for each parameter as specified by the UGA we used, along with the values selected to optimize the distinction of the ^{36}Ar, ^{38}Ar, and ^{40}Ar peaks.

The tuning parameters used in our experiment are listed in the table 5.1. Calibration of the instrument involves determining the appropriate value for the Electronic Gain (mbar/mA), which allows the conversion of mA to mbar on the y-axis. We calibrated the UGA by sampling free air and observing the nitrogen peak. The Electronic Gain was adjusted so that the peak settled at a pressure of 780 mbar (i.e., the atmospheric pressure multiplied by the percentage of nitrogen in the air). Since the capillary system ensures that the pressure reaching the UGA is consistently close to atmospheric pressure, the measured partial pressure values in the graphs are expected to be reliable. However, the response of the device, that is the recorded current for charged particles with a specific e/m ratio, may vary. Thus, calibration is performed for individual peaks rather than the entire spectrum. This explains why the total pressure in the previous graphs appears significantly higher than atmospheric pressure. This discrepancy may affect the measurement of the relationship between ^{36}Ar and ^{40}Ar but not $S_{T-B} = (^{36}\mathrm{Ar}/^{40}\mathrm{Ar})_T/(^{36}\mathrm{Ar}/^{40}\mathrm{Ar})_B$. The separation is determined by the concentration ratio, and any multiplying factors simplify and cancel each other out. Here, B and T refer to the fluid distilled from the bottom (B) and the top (T) of the column, respectively.

More details about the UGA used and V-Lens technology are in [127].

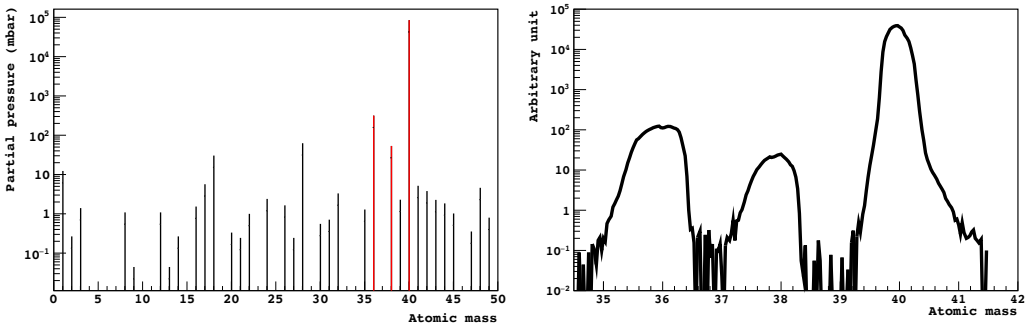

Figure 5.1: Example of the spectrum obtained by UGA during the run in histogram mode (left) and spectrum mode (right). Pressure in mbar in log scale as a function of the atomic mass. Left: histogram where the pressure corresponding to each mass m has been calculated by taking the maximum value between m-0.2 and m+0.2. In red are highlighted 36, 38, and 40, which are the peaks of argon isotopes. Right: Closeup of all the values near the argon peaks. [2]

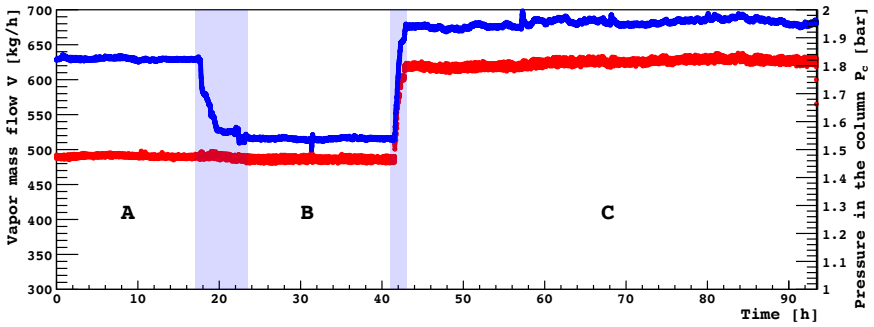

Figure 5.2: Argon vapor mass flow inside the column (in red) and pressure (in blue) in the three regions of interest A, B, and C.

5.2 Argon isotopic distillation

The second run of Seruci 0 lasted for 18 days, from Wednesday, November 17, 2021, to December 4, 2021. The plant was initially planned to be started on November 15, but due to several electrical issues, the start had to be delayed. The objectives set before the run were to gain more confidence in process management, determine the thermodynamic parameters of the system using argon, and validate the results of calculations and simulations.

The graph 5.2 illustrates the behavior of p (column pressure) and V (argon mass flow rate) during the operation of the plant, divided into specific operational phases. The initial and final phases, which have been not represented in the graph, correspond to the initial product loading phase and the shutdown phase and were excluded from the analysis. Phase 0, carried out between November 17 and November 26, involved the start-up and setup operations. These operations included an additional loading phase of argon into the column, resulting in approximately V=245 kg. This operation led to variations in internal column pressures (p) and in other operational values. Therefore, this phase is not considered for a detailed analysis of the separation process.
From November 26 to November 29, the plant operated for the first time in semi-automatic mode (approximately 60%) with a p variability ranging from 150-200 mbar.
Given the variability of process parameters during the setup operations, this report focuses only on the period corresponding to the tests conducted from November 30 to December 4. It should be noted that the approximately 24-hour period between November 29 and November 30 cannot be analyzed in terms of separation due to data acquisition issues. For this reason, the tests denoted as A, B, and C, as shown 5.4, are the only ones that will be described. Specifically, the three aforementioned tests were conducted under the operating conditions of 5.2 : In 5.2 are specified the pressure inside the column p, the maximum

	p (bar)	δ_p (bar)	V_N (kg h^{-1})	T (K)	V (kg h^{-1})	Q (kW)
A	1.824 ± 0.001	± 0.02	491 ± 1	93.3 ± 0.1	543 ± 1	23.0 ± 0.1
B	1.544 ± 0.001	± 0.02	487 ± 1	91.5 ± 0.1	544 ± 1	23.8 ± 0.1
C	1.953 ± 0.001	± 0.04	624 ± 1	94.0 ± 0.1	689 ± 1	29.7 ± 0.1

Table 5.2: Operational parameters of the run for 3 different periods A, B, and C.

pressure variation during the run δ_p to quantify stability, vapor mass flow of Nitrogen in the auxiliary system, vapor mass flow of argon in the column V, average temperature in it T and thermal power of the process Q. Regions A, B, and C refer to the regions mentioned in 4.9 and correspond to the three data points taken at different pressures. The operational parameters of the column are schematically depicted in the following figure 5.3: the pressure difference is highlighted in red, while the other parameters are always intended as the mean alongside the column. The smaller blue column, on the other hand, represents the auxiliary system, with V_N being the flow within this circuit.

Before the start of operations, the column and all process lines were evacuated using a scroll pump. Subsequently, the column was filled with approximately 250 kg of argon in the gas phase. The operational procedure was similar to our previous nitrogen run [1]. Significant automation was implemented throughout the system. It took approximately 12 days of operation to achieve plant stabilization and to start with the distillation measurements presented below. As in the previous run, nitrogen was employed as the refrigerant fluid.

The distillation process was conducted under total reflux conditions. A gas sample extraction rate of approximately 1 L/h was maintained, resulting in an overall loss of $< 0.1\%$

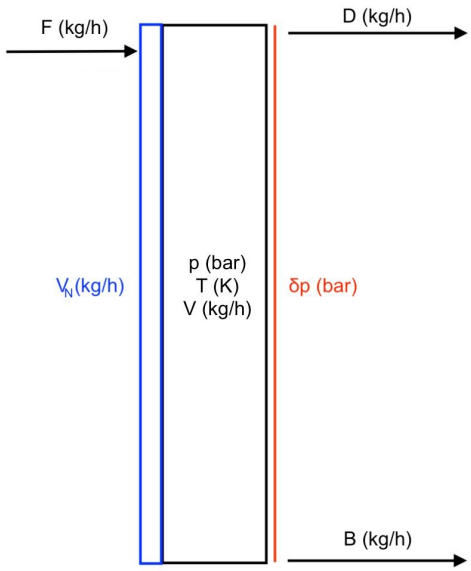

Figure 5.3: The operative parameters of the column of table 5.2 are schematically represented. More details in the text.

of the initial loaded argon mass throughout the run. 5.4 provides detailed information on the flow rate and column pressure for the specific regions of interest.

5.2.1 Description of the sampling system

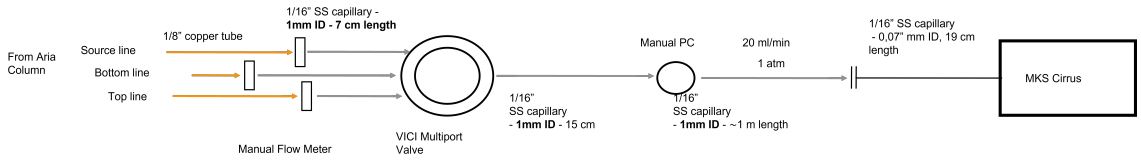

Figure 5.4: Sampling system structure as used for the argon run of Seruci-0 [2]

Throughout the run, the UGA remained operational, making possible the measurement of gas spectra from various sources within the distillation column. Specifically, measurements were taken from the top of the column (Top), the bottom (Bottom), and the feed bottles (Feed). To establish the connection between the distillation column and the UGA for data acquisition, the following setup was employed 5.4. The gas from the Top, Bottom, and Feed (argon cylinder) passed through copper pipes of varying lengths before reaching the final segment of the setup. Mass-flow meters were used to measure and regulate the flow within each capillary. The gas, going through 7 cm capillaries, ultimately reached the multi-inlet valve. This instrument enabled the periodic or manual selection of which inlet to activate, determining which gas would reach the UGA. For this experiment, the inlet valve was automatically changed every hour.

Subsequently, the selected gas passed through a 15 cm capillary and reached a manual pressure regulator. This regulator ensured that the gas pressure stabilized at 1 atm before

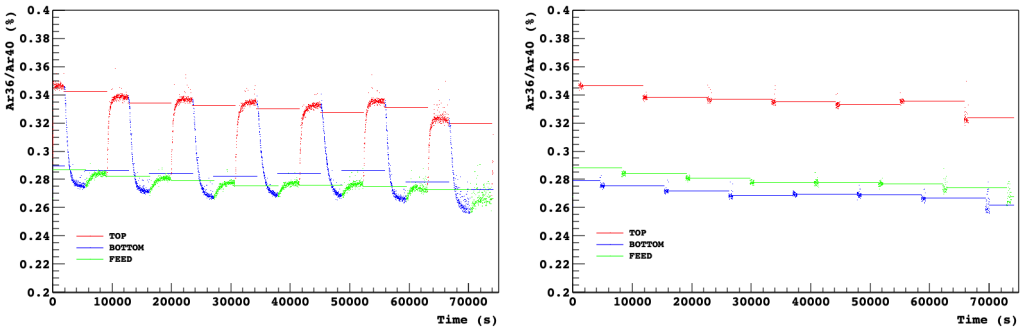

Figure 5.5: $^{36}Ar/^{40}Ar$ as function of time. Every hour the valve is switched from Top (red) to Bottom (blue) and Feed (green). Right: Only the last 15 min before changing the valve again is taken into account.

entering the UGA. Its purpose was to guarantee the desired pressure (1 atm) for the UGA and maintain approximately equal pressures for all gas sources (Top, Bottom, and Feed). Additionally, if the pressure inside the column exceeded certain limits before stabilizing, the pressure regulator would control and restrict the pressure variation reaching the UGA to safeguard the instrument from potential damage. Finally, the gas passed through two additional capillaries, measuring 1 m and 19 cm respectively, before reaching the instrument. The UGA consistently absorbed a flow of around 20 mL/min.

Before the run, the same setup was employed to analyze an argon cylinder with a pressure slightly above atmospheric. Subsequently, the cylinder was switched from argon to nitrogen, and the time it took for the UGA to detect the new gas and stabilize its signal was observed. It was noted that the spectrum obtained from the UGA changed after approximately 10 minutes and stabilized after 40-45 minutes. The transition from the old gas to the new gas was delayed due to the internal volume of the pressure regulator, resulting in an intermediate state where both the old and new gases were detected by the UGA. To ensure accurate measurements of the Top, Bottom, and Feed spectra, we wanted to avoid measuring mixed gasses. Consequently, it was decided to change the valve every hour and consider only the last 15 minutes of data. The first graph 5.5 illustrates the overall trend of the $^{36}Ar/^{40}Ar$ ratio over time, while the second graph exclusively includes data from the last 15 minutes before switching to the next valve. The first graph exhibits the transitions between different valves, while the second graph eliminates such transitions. This approach effectively eliminates cases where the Top, Feed, and Bottom gases are mixed. Finally, the Top/Bottom, Top/Feed, and Bottom/Feed separations were calculated by comparing the ratio between a data group and the median of the previous group.

5.2.2 Separation measurement

In the graphs presented in the previous chapter 5.5, our focus was on measuring the isotopic ratios of argon, specifically ^{40}Ar, ^{36}Ar, and ^{38}Ar. These isotopes are of particular interest as their masses enable efficient detection by the UGA or any mass spectrometer in general. The UGA used in this study is estimated to have a sensitivity of around 15 ppm [127] with three-sigma baseline noise. Therefore, there are no concerns regarding the detection of ^{36}Ar (which is at approximately $3.36 \cdot 10^{-3}$ in the atmosphere) and ^{38}Ar (630 ppm). It should be noted that, due to their similar masses, it is important that the peaks

corresponding to masses 38 and 40 do not overlap 5.1. On the other hand, the important isotope ^{39}Ar is orders of magnitude below the minimum sensitivity of a mass spectrometer. For the measurement of ^{39}Ar, alternative methods for concentration determination and detection, such as the Dart project, which relies on decay and detection of decay products [128].

Since we want to quantify the ability of the distillation column Seruci-0 to separate, our main goal is to measure the separation. Recalling its equation 4.2 in our case it becomes

$$S_{36-40} = (\frac{^{36}\text{Ar}}{^{40}\text{Ar}})_T / (\frac{^{36}\text{Ar}}{^{40}\text{Ar}})_B \tag{5.1}$$

and

$$S_{38-40} = (\frac{^{38}\text{Ar}}{^{40}\text{Ar}})_T / (\frac{^{38}\text{Ar}}{^{40}\text{Ar}})_B \tag{5.2}$$

For simplicity, when referring to the isotopes 36, 38, and 40, we are referring to the molar concentration of the components extracted from above column (D) and below (B). This concentration can be measured by examining the peaks in 5.1, which correspond to different masses. In reality, the spectrum measured by the UGA represents the partial pressure within the ionization chamber on the y-axis corresponding to a specific atomic mass. However, according to the theory of mass spectrometry [129], there is an expected proportionality between this pressure and the number of moles. By minimizing background contributions through practical procedures (such as backing) and statistical methods (subtracting the spectrum obtained with valves closed), we do not expect significant contributions from other substances to the peaks. Therefore, although the value of the partial pressure associated with a peak does not provide direct information, unless precise (and highly situational) calibrations are performed, the ratio between two peaks provides a good (though not perfect and still requiring calibration, as we will see later) estimate of the isotopic ratio. Another issue to consider is the second ionization of molecules. In the section dedicated to the operation of a UGA, we discussed how atoms are ionized inside the mass spectrometer after being bombarded with electrons. The percentage of electrons that undergo ionization is not a fixed value but depends on the tuning parameters we have chosen. Additionally, there is a chance of double ionization occurring on the targeted atom, which contributes to a peak different from the true atomic mass. This happens because the mass spectrometer effectively measures the ratio e/m, so doubling the charge will contribute to a peak with a mass that is half the true mass. For example, the peak of the second ionization of ^{40}Ar appears at m=20. This could introduce distortions since our analysis has focused on mass 40, neglecting the consideration of second ionization peaks. However, this is not a problem since the probability of having second ionization (compared to single ionization) does not depend on the tuning parameters chosen and, in particular, does not vary between isotopes of the same atom (except for cases of particular instability) [129]. Therefore, if we denote this probability as k_{Ar}, we would have:

$$\frac{^{36}\text{Ar} + ^{18}\text{Ar}}{^{40}\text{Ar} + ^{20}\text{Ar}} = \frac{^{36}\text{Ar} + ^{36}\text{Ar} \cdot k_{Ar}}{^{40}\text{Ar} + ^{40}\text{Ar} \cdot k_{Ar}} = \frac{^{36}\text{Ar}(1+k)}{^{36}\text{Ar}(1+k)} = \frac{^{36}\text{Ar}}{^{40}\text{Ar}} \tag{5.3}$$

Therefore, when dealing with isotopes of the same atom, we can only use the peaks corresponding to the first ionization. Another issue with this type of mass spectrometer lies in the response of the current (and therefore the signal we observe) to the partial pressure. Specifically, this response can depend on the spectral region we are in and, consequently, on the atomic mass, as also specified in the UGA manuals. In other words, if we had the same partial pressure for two different masses, we might not have two identical peaks

corresponding to those masses.

One way to overcome this problem is by calibrating for specific masses: we create a situation where we know the partial pressures of the gases (for example, using a cylinder with a known pressure or introducing atmospheric gas) and apply a multiplicative factor to correct the pressure observed in the graph (such as the one in 5.1) to match the expected pressure. However, this presents two problems: first, this multiplicative factor changes depending on the mass, so it should not be the same for the entire graph but different for each mass to be studied (thus requiring a known sample for each of them); second, for certain types of UGA, this factor can change over time (due to environmental temperature changes, for example). In fact, in [105], drift was observed as values of the isotopic ratio (in this case of nitrogen) measured over time from the same cylinder exhibited variations.

Naturally, to achieve maximum accuracy, the concentration in the feed should be measured simultaneously with the others (as the response can indeed change over time). However, due to having only one UGA available, it was not possible to do so. Nonetheless, such changes occur slowly, and therefore, making a measurement every 3 hours is acceptable.

Another method instead involves performing periodic calibrations by also measuring the feed, which is the content of cylinders at constant pressure. Every three hours, we measure the ratio between the 36, 38, and 40 isotopes of argon in the feed and use the results to correct our measurements of the gas coming from the column. Since the composition of the feed is known (it is atmospheric), we can correct the isotopic ratio in the feed and bottom each time.

$$(\frac{^{36}\text{Ar}}{^{40}\text{Ar}})^*_B = (\frac{^{36}\text{Ar}}{^{40}\text{Ar}})_B \cdot (\frac{^{36}\text{Ar}}{^{40}\text{Ar}})^{-1}_F \cdot \frac{0.00336}{0.996} \tag{5.4}$$

$$(\frac{^{38}\text{Ar}}{^{40}\text{Ar}})^*_B = (\frac{^{38}\text{Ar}}{^{40}\text{Ar}})_B \cdot (\frac{^{38}\text{Ar}}{^{40}\text{Ar}})^{-1}_F \cdot \frac{0.00063}{0.996} \tag{5.5}$$

Where 0.00336, 0.00063, and 0.996 are the abundances of ^{36}Ar, ^{38}Ar, and ^{40}Ar respectively. In reality, this correction becomes unnecessary when referring to the overall column separation. By simply using the same formula 5.4 for D (the distillate from above the column) and dividing it by the corresponding value for B (the bottom product), we obtain the separation as described in 5.1 and 5.2, with the correction terms canceling out. Despite this simplification, continuous calibration with the feed is useful both for estimating the true values of the concentrations extracted from the top and bottom and for monitoring the stability of the UGA's response. In fact, without the measurement of the feed, as seen in the previous run [105], we would not have noticed the drift. Furthermore, it should be noted that the data in 5.5 are used as an example before calculating the ratios and, therefore, before applying the correction explained above.

We studied the peaks of the spectrum obtained with the UGA to calculate the separation using 5.1 and 5.2. The concentration expressed as ^{36}Ar, ^{38}Ar, and ^{40}Ar in this equation could be calculated in three different ways:

1. By taking the exact value corresponding to the required mass, that are 36 amu, 38 amu, and 49 amu

2. By taking the maximum on the y-axis on a certain mass range, that is for example from m-0.5 amu to m+0.5 amu or by looking at the shape of the peak on the spectrum

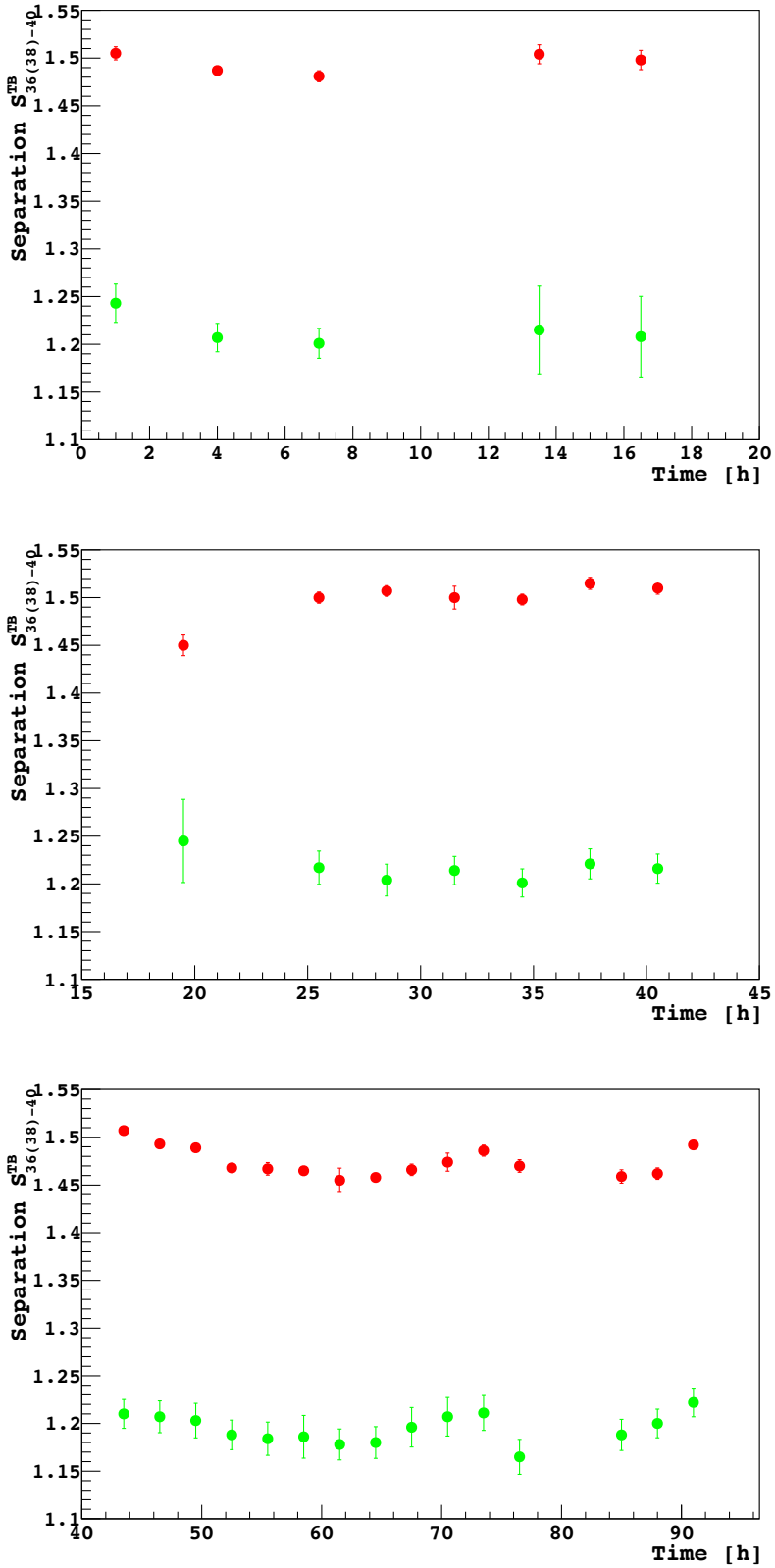

Figure 5.6: Separation S_{3640} (red) and S_{3840} (green) as function of the cumulative time (hrs). From top to bottom: A, B, C intervals

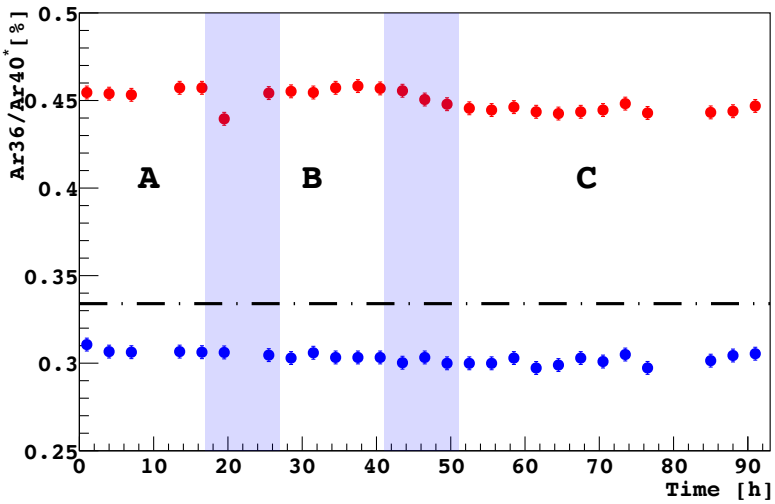

Figure 5.7: From [2]. Corrected expression for the isotopic ratios $(\frac{^{36}\mathrm{Ar}}{^{40}\mathrm{Ar}})^*_D$ and $(\frac{^{36}\mathrm{Ar}}{^{40}\mathrm{Ar}})^*_B$ as in 5.4.

	S_{36-40}	$\ln \alpha_{36-40}$	N	HETP (cm)
A	1.49 ± 0.03	$(5.1 \pm 0.4) \cdot 10^{-3}$	80 ± 7	13 ± 1
B	1.51 ± 0.03	$(5.2 \pm 0.4) \cdot 10^{-3}$	79 ± 7	13 ± 1
C	1.48 ± 0.03	$(4.9 \pm 0.4) \cdot 10^{-3}$	80 ± 8	13 ± 1

Table 5.3: Separation between top and bottom of the column, relative volatility (that changes accordingly to the pressure), Number of stages, and HETP. The average has been calculated in each interval. Data from [2]

3. By calculating the integral under the peaks, that is the sum of the values corresponding to all the masses within a certain range

As explained in [2] and as calculated, the discrepancy between the latter two cases (the first is the least precise since a wrong tuning may strongly affect our results) is smaller than 2% if we consider the concentrations and rises to 5% if propagated to the number of stages and the HETP. In any case, it is smaller than the statistic error so it is irrelevant whether to choose the maximum or integral method.
The tables and are based on equations 5.1 and 5.2 to get the separations for the two isotopes, on the Fenske equation 4.55 to estimate the number of stages and finally on 4.24 to get the HETP. The only parameter missing to apply the aforementioned formulas is the relative volatility, specifically the one between ^{36}Ar and ^{38}Ar, from which the results expressed in [111], [107], and [1] can be used to calculate the relative volatility between ^{38}Ar and ^{40}Ar as well.

The depicted graph (5.8) illustrates the HETP measurements along with their respective errors as a function of the gas factor in the three intervals and is an expansion of 4.9 by taking into account also the results of [1]. The three HETP values are consistent within the margins of error, indicating no significant variation with changes in column pressure. The error on the relative volatility has a bigger impact on the HETP error compared to the error on the separation. Both the pressure difference between the top and bottom of the column and the HETP align with the data from the previous nitrogen run. It is observed

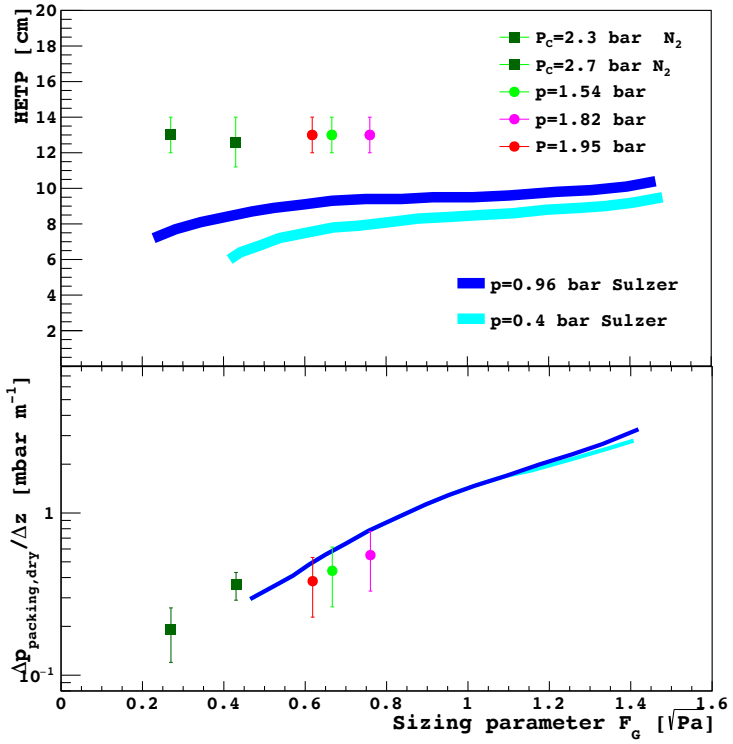

Figure 5.8: Expansion of the fig 4.9. HETP and pressure drop as a function of the sizing parameter (related to the flow inside the column). We put in the same plot data from [2] and [1].

	S_{38-40}	$\ln \alpha_{38-40}$	N	HETP (cm)
A	1.20 ± 0.04	$(2.4 \pm 0.3) \cdot 10^{-3}$	76 ± 17	14 ± 3
B	1.21 ± 0.03	$(2.5 \pm 0.3) \cdot 10^{-3}$	76 ± 13	14 ± 2
C	1.20 ± 0.03	$(2.3 \pm 0.3) \cdot 10^{-3}$	79 ± 15	13 ± 2

Table 5.4: Separation between top and bottom of the column, relative volatility (that changes accordingly to the pressure), Number of stages, and HETP. The average has been calculated in each interval. Data from [2]

that the HETP value associated with the highest pressure (C interval) does not significantly differ from the others. This discrepancy may arise due to the simultaneous influence of two opposing effects that offset each other.

1. The C region encompasses two days, while the other regions (B and A) comprehend only one day each. Consequently, the column had more time to stabilize at the new pressure and facilitate the separation of different components. This suggests that in the B and A regions, the separation process and, consequently, the number of stages may have been underestimated. Thus, the extended duration in the C region may have caused a decrease in HETP.

2. As depicted by the blue data points (provided by Sulzer) in Figure 7, an increase in pressure results in an increase in HETP.

To investigate the influence of the two effects on the HETP of the C interval, it will be crucial to maintain column stability for more time in future experiments. No significant differences were observed when altering the flow rate in column L. Despite having similar pressures (1.82 and 1.95 bar) but different column flows, the A and C intervals exhibit comparable separations, with HETP values within the margin of error. To validate these results, we suggest repeating the measurements over a longer duration, varying the flows while keeping the pressure constant.

It is important to note that the determination of the number of stages is an approximation, specifically establishing the minimum number of stages (denoted as N_{min}, which is equivalent to N only under total reflux conditions as explained in previous chapters). Consequently, the HETP value represents the maximum HETP, and lower values could potentially be achieved.

However, it is worth highlighting that the deviation from total reflux conditions should be minimal, considering that throughout the entire run, less than 0.1% of the total 250 kg inside the column was lost. Thus, the approximation of total reflux conditions is highly accurate [2].

Furthermore, it is important to note that the HETP values obtained in the first run with nitrogen and the second run with argon are statistically compatible with the margin of error.

Figure 5.8 illustrates the pressure drop per meter of column for the dry packing material. It is noteworthy that this value increases linearly on a logarithmic scale with the gas factor (and consequently, the liquid flow rate in the column), consistent with Sulzer's specifications (blue lines) and the previous experimental results obtained with nitrogen (green points). The displacement among the three lines (nitrogen, argon, and Sulzer) can be attributed to the use of different materials.

5.2.3 Multicomponent study of the results of nitrogen run.

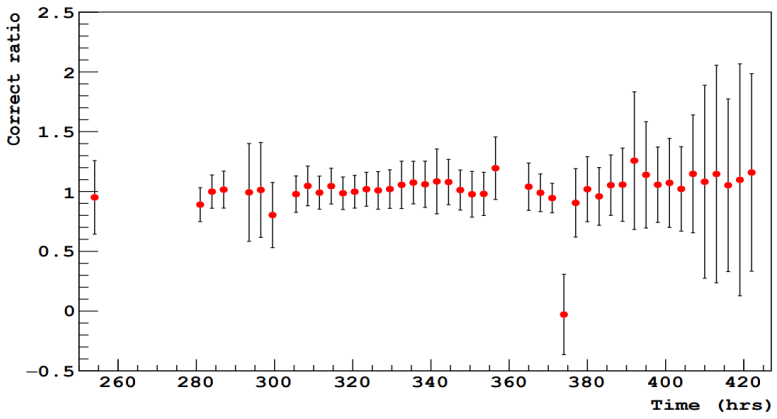

Figure 5.9: It represents 5.9 equation as function of time of the run. We can notice how every data but one is compatible with the expected result within their error. This holds not only for the regions A, B, and C studied in the previous chapters but for the whole run.

By measuring the concentrations of ^{36}Ar and ^{38}Ar, we can calculate the number of stages for both components. If the number of stages is the same, it indicates that the separations of ^{36}Ar and ^{38}Ar are largely independent. This holds true in total reflux conditions only if the two components can be studied separately, without the need for a multicomponent approach. Additionally, the HETPs ($HETP_{36}$ and $HETP_{38}$) depend on the operating conditions of the column and the gas being analyzed. However, since each measurement of ^{36}Ar and ^{38}Ar is taken simultaneously, we do not expect any operational differences. Moreover, as argon gas is used consistently and the two isotopes are chemically identical, we expect them to have the same HETP ($N_{36} = N_{38}$).

$$S_{36-40} = \alpha_{36-40}^{N_{36}} = \alpha_{36-40}^{\frac{h}{HETP_{36}}} \tag{5.6}$$

$$S_{38-40} = \alpha_{38-40}^{N_{38}} = \alpha_{38-40}^{\frac{h}{HETP_{38}}} \tag{5.7}$$

In the next sections, we are going to obtain the formula for calculating the volatility of ^{38}Ar from ^{36}Ar (both with respect to ^{40}Ar). For now, we can say that according to the procedure explained in [111] and given the atomic mass of these isotopes, we can assume that the relationship between α_{36-40} and α_{38-40} is the following.

$$\ln \alpha_{36-40} = \ln \alpha_{38-40} \cdot \frac{19}{9} \tag{5.8}$$

Thus from 5.8, and we can write the following

$$\frac{\ln S_{36-40}}{\ln S_{38-40}} \cdot \frac{19}{9} = 1 \tag{5.9}$$

Therefore, if this expression holds true given the separation measurements and their respective errors, we can conclude that the multi-component approach is unnecessary for the given concentrations of ^{38}Ar and ^{36}Ar. Figure 5.9 illustrates the ratio of the ^{36}Ar and ^{38}Ar separations multiplied by the correction factor of 19/9. It is noteworthy that all data points align within the error range with the line representing a value of 1, except for the data point corresponding to the system shutdown, which is unreliable. The mean of these

values is 0.998 ± 0.030. This demonstrates good agreement between our results and the equation 5.9, confirming that the multi-component approach is unnecessary to simulate argon distillation under these conditions. This experimental evidence establishes that, given the significantly lower concentrations of ^{36}Ar and ^{38}Ar compared to ^{40}Ar, a multicomponent study of the column is not required, and therefore, separate simulation of ^{36}Ar and ^{38}Ar can be performed without affecting the results.

5.2.4 Distillation asymmetry and simulation

Recalling the formula of the separation used for this run (5.1), we now will refer to it as the total separation or top-bottom separation S_{T-B} as it is obtained by dividing the concentration of ^{36}Ar (or ^{38}Ar) over ^{40}Ar distilled from the top to the one distilled from the bottom. However, to quantify the ability of the column to partially separate from feed to top and from feed to bottom, we define the following partial separations.

$$S_{T-F,36-40} = (\frac{^{36}\text{Ar}}{^{40}\text{Ar}})_T / (\frac{^{36}\text{Ar}}{^{40}\text{Ar}})_F \tag{5.10}$$

and

$$S_{F-B,36-40} = (\frac{^{36}\text{Ar}}{^{40}\text{Ar}})_F / (\frac{^{36}\text{Ar}}{^{40}\text{Ar}})_B \tag{5.11}$$

and similary for ^{38}Ar. Where the concentration of argon at the feed is expected to correspond to the natural abundance. However, due to the variation of pressure that occurred during the run, the measure of the ^{36}Ar/^{40}Ar performed with the UGA is not reliable and only the ratio of this quantity at two different conditions (for instance at top and bottom of the column) could be taken into account.

$$S_{36-40,T-B} = S_{36-40,T-F} \cdot S_{36-40,F-B} \tag{5.12}$$

We, therefore, note how the overall separation is caused by two components, one concerning the enrichment of the light element in the upper part of the column and the other which instead quantifies its decrease in the lower part. It is thus possible that the separation made by the column is asymmetrical concerning the top or bottom or that one of the two aforementioned separations has a greater effect than the other on the overall separation.

Moreover, confirmation of the previous statement can be obtained through simulation using Hysys [121]. By setting conditions similar to the experimental setup, we compared the results obtained by considering only ^{36}Ar and ^{40}Ar with those obtained using the multi-component approach. Various input parameters were specified for the simulation, including column parameters (such as HETP, pressure P, and temperature T), feed-bottom separation $S_{F-B,36-40}$, and liquid flow rate L in the column 7.27. $(^{36}\text{Ar})_F$, $(^{38}\text{Ar})_F$, and $(^{40}\text{Ar})_F$ are the isotopic fraction in the feed (natural atmospheric abundances). It is emphasized that such nomenclature is used solely for these simulations since we are dealing with only three isotopes and we need to explicitly specify the simulation formulas. However, since in the subsequent chapters we will face more isotopes, they will be denoted $x_{F,36}$, $x_{F,38}$, and $x_{F,40}$ respectively. The remaining separations, reflux, and heat output were considered as output for comparison. Subsequently, the simulation was repeated using only two components, namely ^{36}Ar and ^{40}Ar, employing the MCT method instead of a rigorous approach. Finally, the experimental outputs (exp), outputs with two components (rig 2.), outputs with three

Input	Value
$(^{36}\mathrm{Ar})_F$	0.0034
$(^{38}\mathrm{Ar})_F$	0.0006
$(^{40}\mathrm{Ar})_F$	0.9960
L	544 kg/h
$S_{F-B,36-40}$	1.096
T	91.5 K
HETP	13 cm
N	79
P	1.54 bar

Table 5.5: Input parameters used for the simulations of Seruci-0 to mimic the conditions in region B. All the parameters are described in the text

Output	Exp.	Rig. 2	Rig. 3	MCT
$S_{T-B,36-40}$	1.51 ± 0.03	1.5 ± 0.1	1.5 ± 0.1	1.5 ± 0.1
$S_{T-F,36-40}$	1.36 ± 0.02	1.4 ± 0.1	1.4 ± 0.1	1.3 ± 0.1
$S_{T-B,38-40}$	1.21 ± 0.03		1.20 ± 0.04	

Table 5.6: Comparison of the results (shortcut, 2 components), with Hysys (rigorous, 2 components and rigorous multicomponent) and MCT method.

components (rig 3.), and MCT outputs (MCT) were compared in the following table 5.6. It is noteworthy that the experimental results and simulations align within the error range. Furthermore, the difference between two-component and three-component distillation is negligible, confirming the compatibility between two-component and multi-component distillation through Hysys simulations. Additional details regarding the MCT simulation can be found in the reference [130].

Regarding the estimation of the error, a standard propagation of the statistical error was performed for the experimental results. However, for the simulations, an estimation was made by varying each time the number of stages within the range of the experimentally determined error. Specifically, since the number of stages was found to be 79 ± 8, the simulation was repeated for N=79, N=87 (upper limit), and N=71 (lower limit). The discrepancy in the separation obtained for these three cases gave us an estimation of the error. On the other hand, the error in the relative volatility was not considered, as its value was assumed to be accurate. This is because the uncertainty in the number of stages was obtained by propagating, among other factors, the error in the volatility. Therefore, we can assume that the error on the relative volatility is already comprehended within the uncertainty of N.

In 5.10, we can observe the trend of the partial separations between the top and feed and between the feed and bottom as a function of the total run time (including all regions, not just A, B, and C analyzed). It is immediately noticeable that the separation between the top and feed is consistently greater than the separation between the feed and bottom. This indicates a significant asymmetry of the column, making it much more efficient in enriching the lighter isotope, 36, in the upper part compared to depleting it in the portion extracted from beneath the column. This asymmetry persists under all conditions, including during

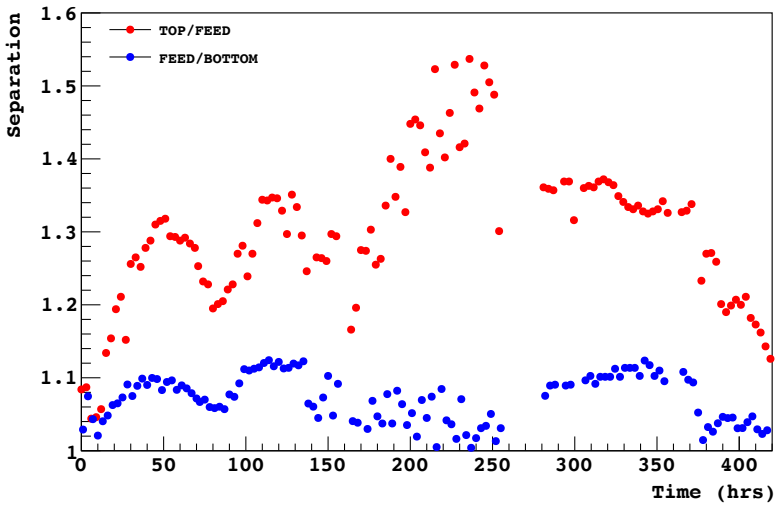

Figure 5.10: Partial separations defined as in equations 5.10 and 5.11 over time during the whole run.

column startup and shutdown. Such asymmetry is a well-known effect in distillation, simply implying that, in the given conditions, the column operates more effectively for extracting a specific component.

Regarding the simulations, it is important to emphasize how the predicted asymmetry significantly influences the operating conditions of the column. For this reason, as seen in 7.27, it was necessary to impose the separation between the feed and bottom as one of the inputs to obtain effective simulations able to replicate the real case. The simulations highlight that even though only small quantities are extracted from the column compared to the column's flow (total reflux condition), the ratio between the quantities extracted from above and below greatly influences the asymmetry. In general, if we extract more from the top, the asymmetry favors separation from the bottom, and vice versa [104]. This phenomenon can be attributed to the conservation of mass. Despite the significantly larger flow in column L compared to the extracted quantities B and D, the formulas for component and mass conservation between the feed and the extracted quantities still hold true, as discussed in previous chapters: $F = B + D$.

In reality, the extraction does not occur in the same manner all the time. Taking into account the sampling system described in the previous paragraphs, there is a flow rate that is consistently extracted from both above and below the column, as indicated by the flow meters (ranging from 5 to 30 mL/min). Additionally, 20 mL/min is extracted by the UGA through the valve that is selected by the multi-inlet valve at a specific moment. Therefore, the 20 mL/min is alternately added to the quantity extracted from the feed, top, and bottom, changing every hour. As a result, in our case, the amount of argon in the column is not exactly constant but decreases due to the irregular extraction between above and below. Despite the extracted quantity being small compared to the total amount in the column, and therefore not significant enough to influence its behavior, from a simulation perspective, the equation $F = D + B$ no longer holds since $F = 0$ while D and B are both small but nonzero. This scenario is referred to as batch distillation, as described in [104], and it requires specific simulation programs to accurately and effectively simulate

distillation and the extracted quantity. Hence, one of the future objectives is certainly to improve the accuracy and precision of simulations by incorporating batch cases. As for future goals, it is desired to operate the Seruci-1 column under conditions that yield large quantities of argon. Consequently, neither total reflux nor batch conditions will apply, as a significant input flow will be introduced. Therefore, the Hysys simulations considered so far are sufficient to describe such situations.

5.3 Nitrogen isotopic distillation

Briefly, we can summarize the main experimental results of the first run of Seruci-0 [1]. Most of the technical characteristics of the column and data analysis have already been explained about the argon run [2], which we have prioritized as it provides the most recent and relevant results since it involved argon, the gas that will be used in the Seruci-1 run. The most important difference concerning the first run lies in the intention to separate different nitrogen isotopes, specifically the molecules $^{14}N^{14}N$ and $^{15}N^{14}N$. On the other hand, it was decided to neglect the $^{15}N^{15}N$ molecule due to its significantly lower concentration, which should be around 13.4 ppm.
Another important difference is about the sampling system, as it does not involve pressure regulation systems that cause delays, as it was for the argon run. Additionally, an EXTREL^{TM} [131] UGA is used for sampling. This allowed data to be collected at a higher frequency compared to the second run. It was decided to distinguish two different phases of the run, which will be referred to as run A and run B. We will refer to $^{14}N^{14}N$ as ^{28}N and to $^{14}N^{15}N$ as ^{29}N from now on. The starting concentrations in the feed are 0.7 % for ^{29}N and 99.3 % for the other one.

The operational parameters for these runs are in the following table 5.7

	P (bar)	δ_P (bar)	V_N (kg h^{-1})	T (K)
Run A	2.7 ± 0.7	12.9 ± 5.4	412 ± 30	87 ± 7
Run B	2.3 ± 0.3	6.9 ± 2.7	247 ± 30	85 ± 3

Table 5.7: Operational parameters of the nitrogen run for 2 different periods, run A and run B

Here we can observe that all the errors are consistently higher by an order of magnitude compared to the second argon run 5.2. This discrepancy is not primarily due to the use of different substances but rather to the operators' increased experience in managing the plant during the run. In other words, they were able to maintain the plant much more stable over time compared to the nitrogen run. This overall stability makes the data from [2] more precise than those from [1], which is why they were analyzed first.
Furthermore, it is worth noting that the errors in run B are approximately half of those in run A. Again, this improvement is a result of the increased stability achieved by significantly reducing the nitrogen flow in the auxiliary circuit from 412 kg/h to 247 kg/h.
The last consideration regarding Table 5.7 regards the pressure. As discussed before, lowering the column pressure also reduces the saturation temperature, thus increasing volatility. Therefore, it is more efficient to work at lower pressures to achieve better separation. Unfortunately, during the nitrogen run, it was not possible to work at lower pressures.

However, during the argon run [2], thanks to the operators' increased experience, this was achieved.

In the following table 5.8 are the final measurements for run A and run B.

	S_{28-29}	$\ln \alpha_{28-29}$	N	HETP (cm)
Run A	1.23 ± 0.03	$(2.60 \pm 0.02) \cdot 10^{-3}$	81 ± 9	12.6 ± 1.4
Run B	1.28 ± 0.03	$(2.83 \pm 0.02) \cdot 10^{-3}$	88 ± 9	11.6 ± 1.2

Table 5.8: Relative volatility, separation, number of stages and HETP in the two runs A and B for nitrogen distillation [1]

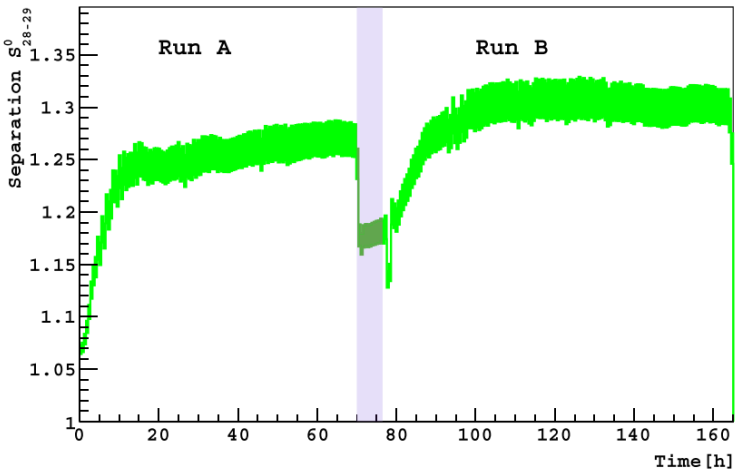

Figure 5.11: Separation for run A and run B and as a function of time of the run [1]

The separation was calculated similarly to the previous chapter, using UGA measurements corrected by the feed, and applying equation 5.1, replacing argon with nitrogen. The idea behind the selection of relative volatility values is shown in the appendix of [1], where measurements from different sources were compared to estimate α_{28-29}, which is different for the two runs due to its temperature dependence. Finally, N and HETP were calculated based on the separation and volatility using equations 4.55 and 4.24. Here, we can use the Fenske equation to calculate the minimum number of stages, and the total number of stages, as we are within the conditions of total reflux. This is because the quantity extracted for measurement purposes is much smaller than the nitrogen content in the column [1]. Contrary to the case of argon, for the nitrogen run we had more data over time, thus the separation was first calculated as a function of the run time, as shown in the graph in Figure 5.11. Subsequently, a linear fit was performed to estimate the HETP within the two intervals. The initial portion of the data, where oscillations were observed, was omitted as the column was still stabilizing 5.12.

In Figure 5.8, the HETP as a function of the gas factor was already shown for both argon and the recently described nitrogen run. Here, we notice how the results are compatible withing their error. It is noteworthy that despite the greater stability of measurements during the argon run, the error on HETP is lower for nitrogen. This can be caused by a higher impact of the error on relative volatility when comparing the tables 5.12 and 7.26. Specifically, the error on α for argon isotopes is greater compared to that for nitrogen isotopes due to larger discrepancies in literature measurements of this value for argon [119].

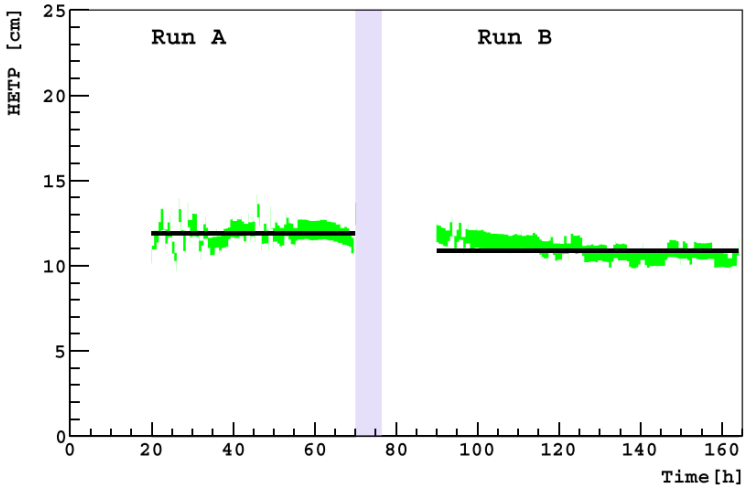

Figure 5.12: HETP for run A and run B and as a function of time. The black lines are the linear fit performed to measure the HETP in the two regions, the results are in 5.8. [1]

In contrast, the available data for nitrogen is more precise and exhibits greater similarity among each other.

In conclusion, the nitrogen run allowed operators to gain experience with the distillation column and its instrumentation and provided an initial estimation of the HETP. It is important to note that this parameter can vary depending on the element or molecule being distilled, as emphasized in [104]. Therefore, to predict the distillation of argon in Seruci-1, a second run with argon was necessary. Both results from papers [1] and [2] are also significant because they represent some of the first cryogenic isotopic distillations and are important milestones for the development of this technique.

Chapter 6

Simulations for cryogenic distillation of argon with Aria

Given the concept of relative volatility explained in the previous chapter, we will face the problem of distilling more than two components 6.1. The Aria project was initially conceived to separate the ^{39}Ar isotope to meet the demands of argon in the TPC for DarkSide-20k. However, subsequent experimental results ([1] and [2]) demonstrated the difficulty of achieving this within reasonable timeframes and with the required level of purity. Therefore, the primary objective of Aria is to purify argon from chemical contaminants. In this chapter, we will revisit the initial concept and the simulations that led to the initial purpose of Aria, which are now being adjusted based on experimental results 6.2. Subsequently, we will delve into the secondary goal related to chemical purification through cryogenic distillation 6.3.
It is essential to emphasize that these simulations represent Aria's short-term capabilities. Therefore, we preferred to employ results and conditions that are well-known and experimentally obtained from the Seruci-0 prototype runs. In the subsequent chapters, we will investigate the future beyond the argon distillation of the Aria project, considering conditions and components that have not yet been experimentally obtained.

6.1 Multi-component approach

In the chapter dedicated to nitrogen distillation, extensive reference was made to the results presented in the article [1]. In addition to discussing the experimental discoveries, several considerations were made regarding the distillation capabilities of the Seruci-1 column for argon, with specific emphasis on isotope 39. These measurements will be updated in the upcoming section taking care of the experimental results of isotope ^{36}Ar and ^{38}Ar distillation of argon. In this paragraph, our focus will be on studying and placing ourselves under the same conditions as those described in said paper. Doing so, we will compare the simulation results obtained using the MCT method with other systems, in particular comparing them with Hysys in the case of multicomponent distillation and two-component distillation.

Let's review the results mentioned in the article, which assumed a binary distillation hypothesis. This assumption states that isotopes other than ^{39}Ar and ^{40}Ar in the gas do not affect the calculations. It's important to note that argon contains significant isotopic fractions of ^{36}Ar (0.33%) and 38Ar (0.06%), while their fractions in UAr are lower. Despite this, considering a binary mixture is reasonable for two main reasons. First, the additional

isotopes are mostly found in the distillate stream because they have higher volatility compared to ^{40}Ar. Therefore, we don't expect a notable difference in the composition of the bottom stream [132]. Second, the isotopic fractions of ^{36}Ar and ^{38}Ar in both the distillate and bottom flow are expected to change only slightly, in fact for each isotope i if we have

$$\frac{Bx_{B,i}}{Fx_{F,i}} < 1 \tag{6.1}$$

$$\frac{Dx_{D,i}}{Fx_{F,i}} < 1 \tag{6.2}$$

Where B D is what we extract from the bottom and the top of the column and x is the mass fraction of the given isotopes. Both are fulfilled in the case of [1] so we did the simulation for ^{39}Ar and ^{40}Ar without considering the other elements. However, as we now have access to tools that enable us to perform simulations with multiple components and different techniques (such as Aspen Hysys), we aim to validate the assumptions made in that article. Therefore, we will replicate the same simulation under identical conditions using Hysys. Initially, we will conduct the simulation with two components, and subsequently with four components, to compare the results.

The inputs used in [1] for the simulation are in table 6.1. It is further emphasized that uncertainties are not included in this table. This is because simulation software does not allow for the input or output of uncertainties. Additionally, the values presented in the table are relative estimates of the column's separation capabilities. Therefore, unless a comparison with other data is necessary, it is preferred not to provide an estimate of the error, as it would be imprecise. The nomenclature chosen here is similar to the one used in the articles. As a reminder, F is the inlet mass flow, and B and D are what we extract from the bottom and the top of the column. L is the liquid flow inside the column, and N is the number of stages. α_{39-40} is the relative volatility in these conditions and $x_{F-B-D,i}$ is the concentration in feed, bottom, or top of isotope i. R is the reflux and Nr is the input feed stage.

Input	Value
$x_{F,39}$	$6\ 10^{-19}$
$x_{B,39}$	$6\ 10^{-20}$
α_{39-40}	1.00133
L	550 kg/h
T	89.5 K
P	1.3 bar
N	2870
B/F	50 %

Table 6.1: Input parameters used in [1] for argon purification from isotope ^{39}Ar

Outputs are in 6.2 where $R_{D,39}$ is a new parameter defined as the ratio of ^{39}Ar getting extracted from the top of the column.

$$R_{D,39} = \frac{x_{D,39}}{x_{F,39}} \tag{6.3}$$

Since the inputs required by MCT and Hysys distillation software are different we write in the following tabular 6.3 the inputs we have used for Hysys. Of course, $x_{F-B-D,36-38}$ are used only for the multicomponent distillation.

Output	Value
B	0.2804 kg/h
D	0.2804 kg/h
F	0.5608 kg/h
R	1995
$x_{D,39}$	$1.10\ 10^{-18}$
$R_{D,39}$	0.9124

Table 6.2: Output parameters used in [1] for argon purification from isotope ^{39}Ar

Input	Value
F	0.5608 kg/h
$x_{F,39}$	$6\ 10^{-19}$
$x_{F,38}$	$6\ 10^{-4}$
$x_{F,36}$	$3.3\ 10^{-3}$
$x_{B,39}$	$6\ 10^{-20}$
α_{39-40}	1.00133
L	550 kg/h
T	89.5 K
P	1.3 bar
N	2870

Table 6.3: Input parameters used in Hysys for argon purification from isotope ^{39}Ar. They are the same for both multicomponent and two-component distillation, apart from $x_{F-B-D,36-38}$ which are excluded from two components distillation.

In the next two tables 6.4 and 6.5 are the main results of the Hysys simulation obtained considering respectively only two and all the isotopes of argon.

Finally, we can compare the results of these three cases in 6.6.

Output	Value
B	0.2657 kg/h
D	0.2963 kg/h
R	1864
$R_{D,39}$	0.9525
$x_{D,39}$	$1.09\ 10^{-18}$

Table 6.4: Results of Hysys simulation with only two components.

Furthermore, we emphasize that it was not possible to estimate the error in the simulation presented in [1], as the inputs used were free of uncertainty. Additionally, Hysys simulations are considered a black box, making it challenging, if not impossible, to determine the error in the results. However, we can estimate a percentage discrepancy between the two outcomes, which is represented in the following table 6.7.

We can observe that all discrepancies are below 5%, indicating good compatibility between the results presented in the paper and the simulations conducted using Hysys.

Output	Value
B	0.264 kg/h
D	0.2941 kg/h
R	1874
$R_{D,39}$	0.9527
$x_{D,39}$	$1.09\ 10^{-18}$
$x_{D,38}$	0.001195
$x_{D,36}$	0.006378
$x_{B,38}$	$1.380\ 10^{-6}$
$x_{B,36}$	$2.452\ 10^{-9}$

Table 6.5: Results of Hysys simulation for multicomponent.

Output	Paper (MCT)	Hysys multi-	Hysys two-
D	0.2804 kg/h	0.2941 kg/h	0.2926 kg/h
D	6.73 kg/day	7.06 kg/day	7.02 kg/day
B	0.2804 kg/h	0.2642 kg/h	0.2657 kg/h
B	6.73 kg/day	6.34 kg/day	6.38 kg/day
$x_{D,39}$	$1.10\ 10^{-18}$	$1.09\ 10^{-18}$	$1.09\ 10^{-18}$
$R_{D,39}$	0.9124	0.9527	0.9524
R	1995	1874	1864

Table 6.6: Comparison between results of MCT in [1], two components and multi-component distillation performed with Hysys

Additionally, focusing on the last column of the table, it is noteworthy that the discrepancy between the two Hysys simulations is consistently below 1%. This suggests that the main cause of the larger discrepancies lies in the difference between the methods employed (MCT as described in the paper and the rigorous approach used in Hysys), rather than the use of a multi-component or two-component approach. Therefore, considering the concentrations involved in this case, we can affirm that there is no difference between multicomponent and two-component distillation, thus confirming the hypotheses and results presented in the article. Furthermore, a good compatibility between the short-cut and rigorous approaches is demonstrated.

Output	Paper(MCT)-Hysys	Hysys multi-two disc.
D	4.6 %	0.51 %
B	4.6 %	0.57 %
$x_{D,39}$	0.91 %	0 %
$R_{D,39}$	4.4 %	0.03 %
R	6.3 %	0.53 %

Table 6.7: Comparison between results of MCT in [1], two components and multi-component distillation performed with Hysys. The discrepancy is defined as the normalized difference between the results.

This result confirms the findings stated in [1] regarding ^{39}Ar and corroborates the results

from previous chapters, where it was demonstrated, based on the experimental outcomes of Seruci-0, that within the error margin, the multi-component approach was not necessary for simulation with argon isotopes. Overall, we can confidently assert that, for typical isotopic concentrations of atmospheric or underground argon, the multi-component approach is never required. Instead, individual isotopes can be freely studied in pairs, providing a reasonably accurate description of the overall behavior. This holds true for ^{36}Ar, ^{38}Ar, ^{39}Ar, and ^{40}Ar.

6.2 ^{39}Ar distillation in Seruci-1

Now we proceed to recalibrate the Seruci-1 simulations presented in the article [1] based on the experimental results from [2]. Therefore, we will consider the conditions of the Seruci-0 run B described in the previous chapter. This will allow us to work under temperatures and pressure that we know can be achieved experimentally. Moreover, these conditions will provide us with the HETP value, which determines the number of stages in the column.
In particular, the measured HETP turned out to be larger than the expected value, resulting in a significant decrease in the number of stages of the Seruci-1 column. Instead of the originally leading to 2800 stages, we now expect to have around 2000 stages once the column is constructed. As we know from equation 4.2, a lower number of stages implies a reduced capability of the column to effectively separate different elements or isotopes.
Therefore, it is necessary to repeat the simulations presented in the paper [1] according to the new conditions. We suggested that we may have to compromise either the purity of the isotope, which was initially assumed to be reduced by a factor of 10 from $6 \cdot 10^{-19}$ to $6 \cdot 10^{-20}$, or the production rate, which was 6.73 kg/day.
We define the ratio $R_{B,39}$ between the ^{39}Ar purity in feed and bottom to quantify the ability of our column to eliminate this impurity

$$R_{B,39} = \frac{x_{F,39}}{x_{B,39}} \tag{6.4}$$

which was expected to be $R_{B,39}$=10 in [1]. In 6.8 are the input parameters used for the

Parameters	Value
P	1.54 bar
T	91.5 K
F	0.5583 kg/h
L	544 kg/h
$x_{B,39}$	6 10^{-20}
α_{39-40}	$(1.418 \pm 0.03) \cdot 10^{-3}$
N	2000
Nr	400

Table 6.8: Input parameters for Hysys simulation for ^{39}Ar suppression. We require to extract from the bottom argon where the isotope ^{39}Ar has been reduced by a factor of 10.

first Hysys simulation resembling the hypothesis of [1] for ^{39}Ar suppression. In the first case, we require $R_{B,39}$=10 and we see what is the production rate we can obtain. The relative volatility between ^{39}Ar and ^{40}Ar is based on α_{36-40} of argon Seruci-0 run in region B applying equation 4.21. The results of the simulation are in table 6.9

Doing so we can extract 2.564 kg/day of argon from the bottom of the column, where the isotope 39 has been suppressed as initially intended by a factor of 10. The production rate is less than half of the value calculated in [1], and it is significantly lower than what is needed to produce the required amount of argon for DarkSide-20k in a reasonable timeframe. In fact, at this rate, it would take a little over a year to produce 1 ton of argon, and thus more than 20 years of operation to produce the amount required by DarkSide-20k's TPC. However, it would still be possible to produce the amount needed for DarkSide-LowMass, which requires only one ton, in case the project is confirmed. In this case, one year of operation would be sufficient. Nevertheless, maintaining the column at its maximum

Output steam mass flows			
	F (kg/h)	D (kg/h)	B (kg/h)
	0.5583	0.4560	0.1017
Compositions			
	F	D	B
^{36}Ar	0.0034	0.004108	$2.935\ 10^{-7}$
^{38}Ar	0.0006	0.0007690	$5.346\ 10^{-6}$
^{39}Ar	$6\ 10^{-19}$	$7.2\ 10^{-19}$	$6\ 10^{-20}$
^{40}Ar	0.9900	0.9951	1.000

Table 6.9: Output parameters for Hysys simulation for ^{39}Ar suppression of a factor 10.

potential for a year is complex and expensive.

Alternatively, if we were to request a production rate equal to that hypothesized in the simulations from [1], the results would be as shown in Table 6.10.

Output steam mass flows			
	F (kg/h)	D (kg/h)	B (kg/h)
	0.5583	0.27915	0.27915
Compositions			
	F	D	B
^{36}Ar	0.0034	0.006719	$5.733\ 10^{-7}$
^{38}Ar	0.0006	0.001248	$1.153\ 10^{-6}$
^{39}Ar	$6\ 10^{-19}$	$1.088\ 10^{-18}$	$1.12\ 10^{-19}$
^{40}Ar	0.9900	0.9920	1.000

Table 6.10: Output parameters for Hysys simulation for ^{39}Ar suppression, requiring the extraction of the same flow from the top and bottom of the column.

In this case, we are trading off the higher production rate for a significant decrease in purity. Specifically, the suppression factor of ^{39}Ar, denoted as $R_{B,39}$, becomes 5.35, which is nearly half of the originally desired value. Consequently, the production rate would remain around 6.73 kg/h, allowing us to produce 1 ton in just under six months. However, this timeframe is still too long to achieve the desired 20 tons in a reasonable amount of time (as it would still require almost 10 years of continuous operation at full power).
Alternatively, even under these conditions, it could be considered reasonable to produce the tons required for LowMass, requiring less time compared to the previous conditions described in Table 6.9.

In general, the experimental results from [2] inevitably reinforce what was hypothesized in [1], that is that the main limitation of Seruci-1 at the moment lies not in its ability to separate isotopes (which is linked to the column height), but rather in the low extraction rate that hinders the production of the required quantities within the desired time frame. This limitation also extends to other characteristics, such as the column flow rate, which is in turn related to the diameter of the column. A larger diameter would allow for more fluid circulation in the column and, consequently, a higher production rate, as suggested in [104]. For this reason as well, one of the upcoming chapters will focus on simulations for potential beyond argon projects involving Aria, sometimes considering alternative columns

with different packing materials and diameters.

For now, Seruci-1 confirms its effectiveness in chemical separation, which is crucial for purifying argon from other impurities such as nitrogen. This aspect will be explained and simulated in detail in the next chapter.

6.3 Chemical purification via distillation with Seruci-1 for DarkSide-20k

The purpose of this paragraph is to illustrate the potential of the Seruci-1 distillation column in chemically purifying argon from Urania by removing various impurities, the most significant of which is nitrogen. The purified argon is crucial as it will be sent to the Gran Sasso Underground Laboratory to be used in the DarkSide-20k TPC (Time Projection Chamber). Nitrogen is particularly troublesome because it can be present in large quantities or at higher concentrations compared to other chemical impurities [6]. Furthermore, its presence, as we will see in later chapters, also affects the measurements that will be conducted in DarkSide. Specifically, nitrogen is known to significantly influence the argon scintillation above certain quantities, in particular suppressing the triplet signal [61]. Additionally, one hypothesis is that the presence of contaminants in argon may cause an increase in single-electron signals. Currently, the primary hypotheses concern distillation in either one or two steps: the former involves removing only nitrogen from argon, while the latter aims to significantly reduce all contaminants. Simulations will be conducted for both scenarios using both Seruci-1 and the prototype Seruci-0 to assess whether the latter may already be adequate for the purpose. Right now, the most plausible hypothesis is to eliminate only nitrogen from argon through a single distillation pass. Recent simulations (yet to be confirmed and therefore not included in the thesis) suggest that Seruci-0 might be sufficient to reduce nitrogen in argon below the ppb level. However, these hypotheses require confirmation, and we expect greater insights during the upcoming run of Seruci-0, where a chemical distillation of argon will be performed. Another important premise regarding the simulations in this section is that optimization will be performed based on the conditions we were able to recreate during the study of the Seruci-0 prototype. For example, despite the previous chapters indicating that reducing pressure significantly lowers the temperature in the column, thereby increasing relative volatility and the column's separation capacity, we will only consider the lowest pressure obtained during the run to ensure realistic scenarios. The same approach will be followed in the next chapters about oxygen production. Conversely, in the chapter about the separation of CO and NO isotopes, we will consider future projects beyond argon that involve the use of Seruci-1 even after it has fulfilled its initial purpose.

6.3.1 Chemical purification via distillation with Seruci-1

Using Seruci-1 under conditions similar to those used in the November-December 2021 run, it is possible, according to Hysys simulations, to efficiently separate argon from other impurities. The report will present two cases: in the first case, a single distillation can completely reduce the concentration of N_2 (10^{-32}), while the other impurities remain unchanged; in the second case, through two consecutive distillations, nitrogen can be reduced to 10^{-31}, while the other impurities are completely suppressed 10^{-30} and lower).

This chapter will provide a summary of the Hysys simulations demonstrating and showing the chemical purification potential of the Seruci-1 column for argon. The following

substances are considered as impurities:

1. Nitrogen (N_2)
2. Carbon dioxide (CO_2)
3. Methane (CH_4)
4. Krypton (Kr)
5. Oxygen (O_2)

The objective of the simulations is to demonstrate through which steps and under what conditions each impurity can be reduced to 10^{-6} or lower of the argon concentration.

Given the need to distill a mixture composed almost entirely of argon, the same conditions of pressure, temperature, and column flow used during the previous Seruci-0 run (November and December 2021) were adopted. In particular, the column pressure considered for the simulations is the lowest stable pressure reached during the run (1.54 bar) corresponding to an argon saturation temperature of 91.47 K. Finally, the column flow rate is realistic and set at 500 kg/h. The number of stages in the column is determined based on calculations from experimental data of the previous runs rounded to thousands.

The following table summarizes the parameters of the Antoine equations, saturation temperature, and relative volatility (concerning nitrogen) for each element.

Element	a	b	c	d	T(K)	α
N_2	35.411	-966.2	-4.3185	$7.93 \cdot 10^{-5}$	81.09	1.194
CO_2	13.362	-4735	-21.267	0.0409		
CH_4	31.350	-1307	-3.261	$2.94 \cdot 10^{-5}$	117.01	1.950
Kr	33.207	-1452	-3.516	$2.59 \cdot 10^{-5}$	125.36	3.011
O_2	32.233	-1090	-3.301	$4.06 \cdot 10^{-5}$	94.39	1.059
Ar	31.380	-1039	-3.408	$4.80 \cdot 10^{-5}$	91.47	1.000

Table 6.11: Antoine parameters used for chemical purification via distillation in Seruci-1. T is the saturation temperature and α is the relative volatility between each element and argon.

We underline how carbon dioxide is solid at the column's pressure and temperature; therefore, we expect it to settle downwards and fully join the liquid extracted from the bottom of the column.

We observe that all impurities have a higher saturation temperature than argon, except for nitrogen alone. This implies that CH_4, Kr, and O_2 tend to move downward in the column, while N_2 moves upward. Consider the following gases entering the column (from the top):

In this context, the value of 10^{-30} is unverifiable, as there are no instruments that are sensitive enough to measure it, and it is unlikely to be realistically achievable due to the potential influence of any other form of contamination (such as contaminants in the pipes). Therefore, this value merely represents the column's ability to effectively eliminate such contaminants. Maintaining the column under the same conditions as in the previous paragraphs, with a reflux ratio of R = 50000, the following is obtained, respectively from above and below the column. The amount extracted from below is thus 99.96% of the incoming flow and the concentration of nitrogen has been eliminated. The following graph (6.1) shows the trend of each element's concentration within the column. We notice how

Mass Flow (F)	25 kg/h
N_2	10^{-4}
CO_2	10^{-6}
CH_4	10^{-6}
Kr	10^{-6}
O_2	10^{-6}

Table 6.12: Inlet feed of Seruci-1 column. Hypothesis where only the nitrogen contamination must be reduced.

	B	D
Mass Flow	24.99 kg/h	0.01 kg/h
N_2	$< 10^{-32}$	0.2492
CO_2	10^{-6}	$1.22 \cdot 10^{-30}$
CH_4	10^{-6}	$4.44 \cdot 10^{-31}$
Kr	10^{-6}	$2.32 \cdot 10^{-31}$
O_2	10^{-6}	$8.86 \cdot 10^{-31}$
Ar	$\simeq 1$	0.7508

Table 6.13: Output feed of Seruci-1 column. D is the distillate from the top and B from the bottom

the height of the column is more than enough to perform this distillation as only a few of the stages are in fact separating the elements.

It can be deduced from this that not the entire column is fully used for distillation. Therefore, if the actual number of stages were less than 2000, the simulation results would still remain valid.

In this manner, we can preserve what is extracted from below the column (essentially almost all of what we have in input and a loss of only 0.01 kg/h), while effectively suppressing the most problematic contaminant that is nitrogen. Regarding the other contaminants, they are neither purified nor amplified but remain at a constant level of contamination that we can consider acceptable. Current estimates indicate that the fluid coming from Urania will already be chemically purified by them, and therefore the purpose of Aria will only be to suppress nitrogen. If this is the case, the Seruci-1 column would be perfect, as it would completely eliminate nitrogen and achieve an acceptable production rate (approximately 25 kg/h, equivalent to 600 kg/day). In this way, the 20 tons required by DarkSide 20k could be produced in approximately one month of distillation. The only limitation may arise from the flow that the pipes of the distillation plant and the overall structure may accommodate. For this reason, the next run of Seruci-0 will aim to extract continuously from both above and below the column, rather than operating at total reflux. This will be useful, among other things, to determine the flow capacity of the pipes and identify any issues related to continuous distillation over extended periods.

If, on the other hand, the objective were to suppress all impurities and not just nitrogen, then two successive distillations would be required. First, we would need to introduce the argon from Urania below the column (or in the lower section of the column to enhance separation efficiency) and extract the fluid from the top of the column, which will be purified of all impurities except for nitrogen. Subsequently, the opposite process would

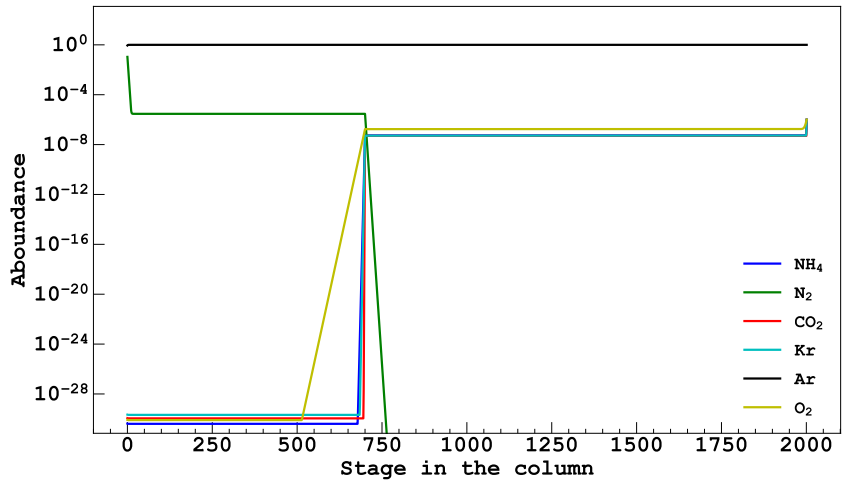

Figure 6.1: Distribution of the mass concentration of the different elements in Seruci-1 simulation

be carried out. That is, we would introduce the just distilled gas into the upper part of the column and extract it from below. In this way, we would be in a similar condition to the case described earlier, thereby achieving significant suppression of nitrogen while leaving the concentrations of other elements unchanged, as they would have already been eliminated in the previous distillation. Overall, two distillations would be sufficient to remove all impurities from argon, including those with lower volatility (like nitrogen). The

Mass Flow (F)	25 kg/h
N_2	10^{-4}
CO_2	10^{-4}
CH_4	10^{-4}
Kr	10^{-4}
O_2	10^{-4}

Table 6.14: Inlet feed of Seruci-1 column. Hypothesis where the concentration of all contaminants must be reduced.

composition distribution inside the column is in plot 6.2 Using the column under the same conditions as described in the previous paragraph and with a reflux ratio of R = 20.0, the following results are obtained from the first distillation 6.15.

In this case, a significant portion of the available flow (99.96%) has been extracted from above, resulting in a substantial reduction of the concentrations of all impurities except for nitrogen. Under these conditions, the nitrogen concentration remains equal to or slightly enriched compared to the inlet. The fluid extracted from above the column will undergo a further distillation process to reduce the nitrogen concentration (by extracting from below) while not increasing the concentrations of other impurities. For this second distillation, the column is in the same conditions as the previous case that is having the inlet at the top. The following results are obtained from this process 6.16.

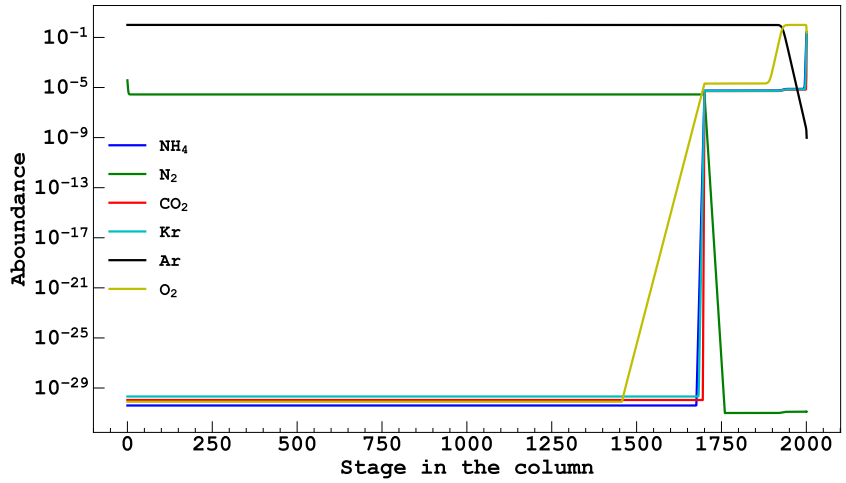

Figure 6.2: Distribution of the mass concentration of the different elements in Seruci-1 simulation, suppression of all contaminants but nitrogen.

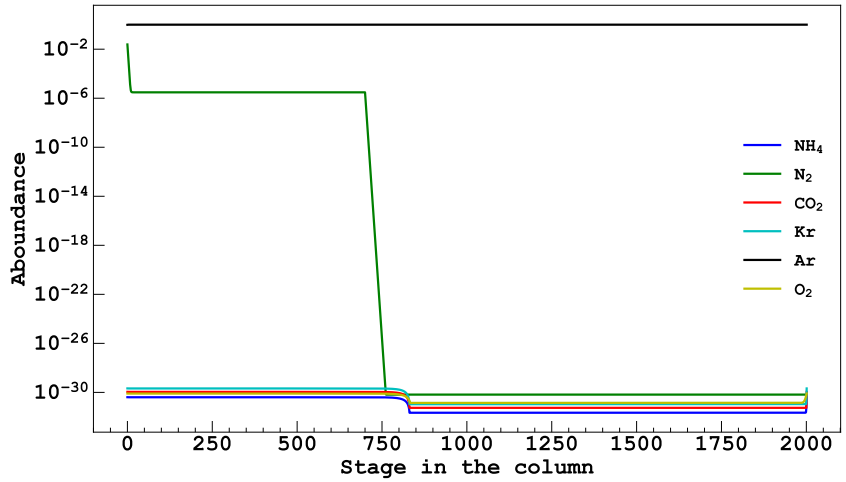

Figure 6.3: Distribution of the mass concentration of the different elements in Seruci-1 simulation, suppression of nitrogen.

	B	D
Mass Flow	0.01 kg/h	24.99 kg/h
N_2	$1.30 \cdot 10^{-31}$	$< 10^{-4}$
CO_2	$\simeq 0.25$	$1.10 \cdot 10^{-30}$
CH_4	$\simeq 0.25$	$4.02 \cdot 10^{-31}$
Kr	$\simeq 0.25$	$2.10 \cdot 10^{-30}$
O_2	$\simeq 0.25$	$8.01 \cdot 10^{-31}$
Ar	$1.71 \cdot 10^{-10}$	$\simeq 1$

Table 6.15: Output feed of Seruci-1 column. D is the distillate from the top and B from the bottom. Suppression of all contaminants but nitrogen.

Thus, after the second distillation, it is possible to eliminate the concentrations of

	B	D
Mass Flow	24.95 kg/h	0.04 kg/h
N_2	$6.60 \cdot 10^{-31}$	$6.25 \cdot 10^{-2}$
CO_2	$1.10 \cdot 10^{-30}$	$1.13 \cdot 10^{-30}$
CH_4	$4.02 \cdot 10^{-31}$	$4.12 \cdot 10^{-31}$
Kr	$2.09 \cdot 10^{-30}$	$2.15 \cdot 10^{-30}$
O_2	$8.01 \cdot 10^{-31}$	$8.22 \cdot 10^{-31}$
Ar	$\simeq 1$	0.9375

Table 6.16: Output feed of Seruci-1 column. D is the distillate from the top and B from the bottom. Suppression of nitrogen.

CH_4, Kr, and O_2, while reducing N significantly to the order of 10^{-31}. Overall, only 0.05 kg/h out of the initial 25 kg/h available at the beginning of the first distillation have been wasted.

Regarding the case of double distillation, it is evident that the time required to produce 20 tons of argon would increase. However, it will still be tolerable. In addition to the fact that performing the distillations would simply take approximately twice as long (in the second case, the outlet flow would decrease from 24.99 to 24.95, but this difference is negligible), it is necessary to consider the time required to fully refill the column a second time before proceeding with the distillation. According to [1], the column will contain a total of approximately 2.5 tons of argon, thus requiring an additional approximately 100 hours from the first run to produce the purified argon to be reintroduced into the column for the second run. Furthermore, the amount of wasted argon from Urania would increase as well. Despite recovering more than 99% of what is input into the feed with the required purity, this does not account for the argon used to fill the column for starting the operation, which, considering two runs, would correspond to 5 tons of unused argon.
It is important to underline that the process is completely reversible. Initially, nitrogen could be eliminated by extracting from the bottom of the column, followed by the removal of other contaminants by extracting from the top: that is the opposite of the current approach. According to simulations, the results would be identical.

6.3.2 Chemical purification via distillation with Seruci-0

Observing the distribution of the elements within the column (6.1, 6.2, and 6.3) it appears that only a fraction of the column is being used. The relative volatilities among different chemical elements are huge when considering a column designed for isotope distillation, where separation is expected to occur between different isotopes of the same atom. Such isotopes are inherently more difficult to separate and exhibit significantly smaller relative volatilities. Thus, it raises the question of whether such distillation would be reasonable with the Seruci-0 prototype column. In this paragraph, we will investigate this hypothesis.

In order to distill a mixture composed almost entirely of argon, the same column conditions of pressure, temperature, and flow were chosen as those used during the previous run of Seruci-0 (November and December 2021). Specifically, the column pressure considered for the simulations is the lowest value stably reached during the run, which is 1.54 bar. This corresponds to an argon saturation temperature of 91.47 K. The column flow rate is set realistically at 500 kg/h. The number of stages in the column is determined by calculations based on experimental data from the separation in the previous run, rounded to 80 stages.

The composition of the mixture entering the column is the same as in Seruci-1 6.12. By using the reflux R=20230 and considering the inlet at the top of the column we obtain the following results 6.17. It can be observed that the effectiveness of the column is much

	B	D
Mass Flow	24.99 kg/h	0.01 kg/h
N_2	$6.62 \cdot 10^{-7}$	0.9917
CO_2	10^{-6}	$1.22 \cdot 10^{-20}$
CH_4	10^{-6}	$2.13 \cdot 10^{-11}$
Kr	10^{-6}	$3.08 \cdot 10^{-12}$
O_2	10^{-6}	$3.54 \cdot 10^{-9}$
Ar	$\simeq 1$	0.0083

Table 6.17: Output feed of Seruci-0 column. D is the distillate from the top and B from the bottom

lower compared to Seruci-1 in terms of suppressing nitrogen concentration, which is reduced to 0.1 ppm, compared to the 10^{-31} achieved in the previous section. However, it should be noted that an extraction flow identical to that of the Seruci-1 case can still be achieved, resulting in the same production rate of purified argon. A significant advantage is the smaller amount of argon required to fill the column (approximately 250 kg, according to [2]), resulting in a reduced waste of underground argon. Additionally, as highlighted by [61], a nitrogen concentration of 1 ppm would be sufficient to avoid any effects on argon scintillation. Analogously to the previous case, it is also possible to perform a double distillation by extracting from below in one case and from above in the other to suppress all impurities. Starting from feed concentrations as given in table 6.14, we obtain the following results in 6.18 by extracting from the top. Subsequently, we can extract from the bottom and obtain 6.19. Once again, the two distillations are reversible.

From these results, we can finally observe that the double distillation ensures the total suppression of all impurities except for nitrogen, which remains at approximately 1 ppm. In summary, although Seruci-0 needs less resource, energy, and argon consumption for performing chemical purification, it does not reduce nitrogen to less than approximately

	B	D
Mass Flow	0.03 kg/h	24.97 kg/h
N_2	$9.57 \cdot 10^{-7}$	10^{-4}
CO_2	0.093	$1.10 \cdot 10^{-30}$
CH_4	0.093	$3.99 \cdot 10^{-31}$
Kr	0.093	$2.09 \cdot 10^{-30}$
O_2	0.093	$3.90 \cdot 10^{-10}$
Ar	0.628	$\simeq 1$

Table 6.18: Output feed of Seruci-1 column. D is the distillate from the top and B from the bottom.

	B	D
Mass Flow	24.95 kg/h	0.02 kg/h
N_2	$1.06 \cdot 10^{-6}$	0.0996
CO_2	$1.10 \cdot 10^{-30}$	$1.15 \cdot 10^{-30}$
CH_4	$3.99 \cdot 10^{-31}$	$4.16 \cdot 10^{-31}$
Kr	$2.09 \cdot 10^{-30}$	$2.18 \cdot 10^{-30}$
O_2	$3.90 \cdot 10^{-10}$	$3.90 \cdot 10^{-10}$
Ar	$\simeq 1$	0.9004

Table 6.19: Output feed of Seruci-0 column. D is the distillate from the top and B from the bottom. Second run for nitrogen suppression.

one part per million. Alternatively, extracting less from the column and requiring a lower nitrogen concentration could be considered (as explained in previous sections discussing the general characteristics of distillation columns), but this would naturally reduce the production speed. In conclusion, Seruci-1 is still the optimal choice for the complete and rapid suppression of all contaminants through a double pass or only nitrogen with a single pass, depending on the impurities present in the argon produced from Urania.

Currently, the decision process regarding which approach to use for argon distillation is still ongoing. Therefore, it remains uncertain whether Seruci-0 or Seruci-1 will be used, and whether a single-pass or double-pass distillation will be performed-
Recent simulations and optimizations suggest that, even with just the prototype Seruci-0, it may be possible to reduce the nitrogen concentration to below ppb in a single pass. However, this hypothesis still requires confirmation, and further developments and studies about this topic are programmed for the near future.
Crucial to the understanding of the process will be the experimental results we expect to obtain from the upcoming run of Seruci-0. This run has the goal of performing chemical distillation (in the previous two runs it was isotopic) and extracting significant quantities of gas. Additionally, an investigation will be conducted to determine if the pipelines pose a bottleneck to the flow of purified argon that can be extracted, a factor not accounted for in the simulations.

6.3.3 Chemical purification via distillation for LEGEND

Based on the previous chapter concerning LEGEND-1000 (see 2.5.3), another application of the Aria project, particularly Seruci-1, would be to produce chemically purified argon

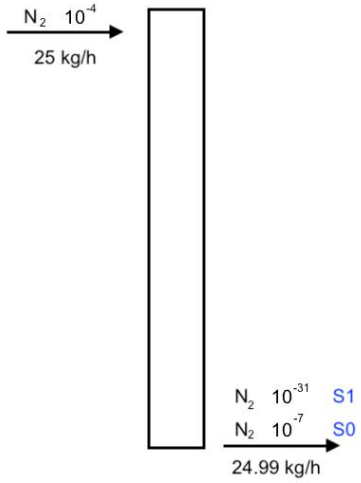

Figure 6.4: Schema of one run of chemical purification via distillation for Seruci-1 and Seruci-0 for nitrogen suppression. In the plot is the concentration of nitrogen in the case of Seruci-1 (S1) and Seruci-0 (S0).

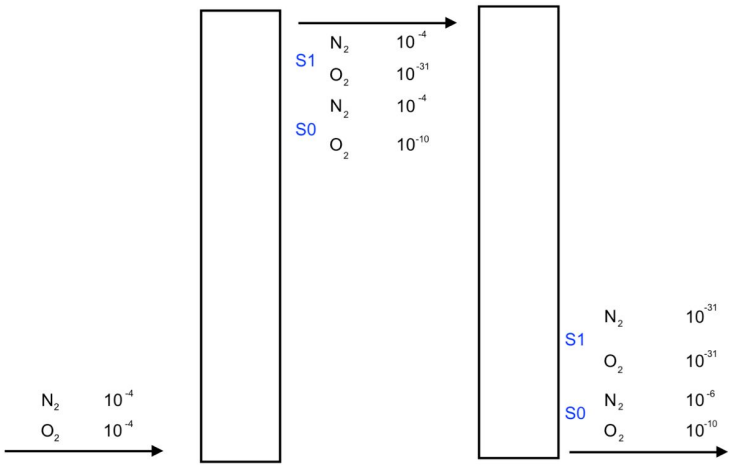

Figure 6.5: Schema of two runs of chemical purification via distillation for Seruci-1 and Seruci-0 for nitrogen and other impurities suppressions. In the plot are the concentration of nitrogen and oxygen in the case of Seruci-1 (S1) and Seruci-0 (S0).

for the veto system of LEGEND-1000. Thus, we would need to produce 25 tons of argon with purity requirements similar to those of DarkSide-20k [81]. In this case, it is enough to adopt the simulations already performed for DarkSide-20k and extend them for an additional 25 tons. Having already demonstrated a production rate of slightly less than 25 kg/h, completely suppressing any impurities in two passes in Seruci-1 (or solely suppressing nitrogen in a single pass), this indicates that we could produce the amount required by LEGEND-1000 in less than one and a half months if we only need to suppress nitrogen, or approximately 3 months if we aim to eliminate each impurity (including the time to refill the column a second time). Since the production for LEGEND is indistinguishable from that of DarkSide-20k, we can execute both productions simultaneously, effectively fulfilling the demands of both DarkSide and LEGEND within 2.5 months (single pass) or over 5 months of run (double pass).

Chapter 7

Distillation with Aria beyond argon

We will start with the first and more realistic scenario, namely the distillation of oxygen 7.1. Despite the fact that it is scheduled after the distillation of argon, we have chosen to study it without making radical changes to the conditions of the Seruci-1 distillation column. Doing so we will consider a distillation process that could potentially begin immediately after the argon distillation. The other future cases will comprehend possible column evolution and, in general, the development of the Aria project. Further in this chapter, we will focus on simulations and long-term predictions much beyond argon distillation, considering even the hypothesis of adding other columns to the Aria project. Specifically, we will consider a Seruci-F column for separating CO and NO isotopes 7.2 7.3, and proceed with the optimization of distillation for both elements 7.3.3, 7.3.4, 7.3.5, 7.3.6. Finally, we will explain the conditions under which the Aria project could be used to produce the germanium isotopes required for LEGEND experiments 7.4.
We emphasize that uncertainties are not included in the tables of this chapter. This is because simulation software does not allow for the input or output of uncertainties. Additionally, the values shown in the table are relative estimates of the column's separation capabilities. Therefore, unless a comparison with other data is necessary, it is preferred not to provide an estimation of the error, as it would inherently be imprecise.

7.1 O_2 distillation with Seruci-1

Magnetic Resonance Imaging [133] and Spectroscopy are methods widely applied in clinical practice for diagnostic purposes, and for monitoring response to therapy in patients affected by pathologies. MR methods detect the magnetic moment associated with nuclear spins, typically ^{1}H. ^{17}O is a stable oxygen isotope with a 5/2 nuclear spin and a large quadrupole moment. Given the presence of oxygen in biological systems and its centrality in many biochemical reactions, ^{17}O would be an exceptionally informative probe for MRI and MRS, with potentially important applications in biomedicine. Studies with ^{17}O labeled molecules have provided preliminary evidence of the feasibility of MRI and MRS with ^{17}O [134] and a demonstration of its sensitivity to biological processes [135],[136],[137]. The only available clinical method to assess metabolism in vivo relies on PET, a radio-diagnostic technique that measures the action of fluorodeoxyglucose (FDG) tagged with a radioactive label as a surrogate measure of metabolic rates. It is worth noticing that ^{18}F-FDG is synthesized from ^{18}O that can be obtained by cryogenic distillation using Aria. ^{17}O MR provides an insight into the rate of oxygen metabolism in living tissues and, unlike PET, does not involve any ionizing radiation dose, thus enabling repeated scans on the same subject. However, the availability and affordability of sufficient quantities of ^{17}O

remain a major impediment to extending these pilot studies and bringing them closer to clinical applications. Furthermore, the detection of oxygen isotopes in exhaled breath could provide us insights about oxygen metabolism in the lungs and other organs. Mass spectrometry detection of ^{13}C in breath has been validated as a diagnostic test looking for helicobacter pylori. The same could be extended to the detection of ^{18}O, thus providing a new, non-invasive approach to the study of problematic metabolism in a variety of diseases.

Rare oxygen isotopes are produced in a few sites in various parts of the world. The

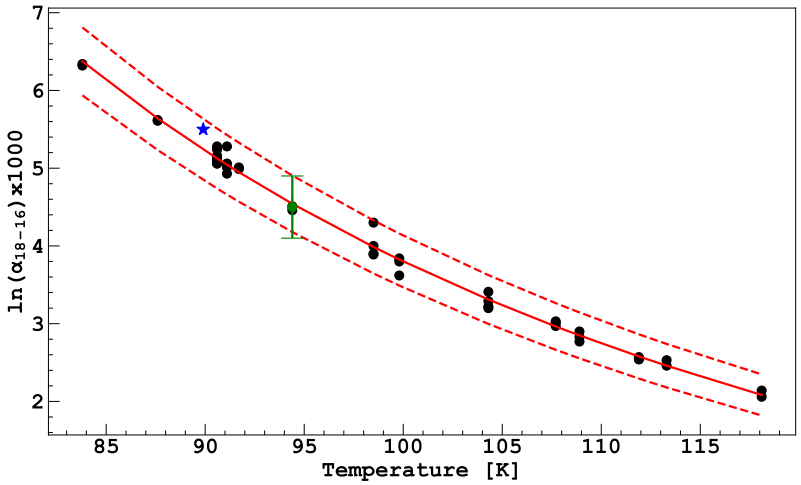

Figure 7.1: Relative volatility α_{18-16} as a function of the temperature. Black point refers to [119] and blue star to [111]. The dotted line corresponds to the interval of accepted volatility as a function of the pressure and temperature chosen for our calculations. The red line is the fit of the points and the green point is the value we are going to use in the next simulations.

production saw a dramatic increase during the last 10-15 years [138] and the final product is sold as water or molecular oxygen [138]. Right now, the production share among technologies of 18-oxygen-water is 26% molecular oxygen rectification ([139], [140]), 1% NO low-temperature rectification (a technology with huge safety issues, that led to major accidents, and therefore almost abandoned), 18% CO low-temperature rectification/rectification of water and 55% vacuum rectification of water.

Compared to the ^{39}Ar to ^{40}Ar, that is the original goal of Aria, the distillation of oxygen isotopes, in terms of the required number of theoretical stages and therefore of column height, is easier, since the relative volatility of $^{18}O^{16}O$ to $^{16}O^{16}O$ is 1.006 [119] and expected (but not measured yet) to be 1.003 to $^{17}O^{16}O$, at 90 K [111]. However, the research target of Aria for the dark matter experiments is to reduce the isotopic abundance of ^{39}Ar only by a factor of about ten. On the contrary, $^{17}O^{16}O$ and $^{18}O^{16}O$ molecules, for medical diagnostics applications, need to be enriched up to dozens of percent, implying enrichment factors from hundredths to thousands, making it very challenging.

Given the just-explained importance of isolating oxygen and carbon isotopes, our objective is to define the future potential of Aria in distilling these isotopes, specifically

Iso.	Ab.	Molecule	Mass frac.	α_{i-16}	a	
^{16}O	0.99762	$^{16}O^{16}O$	0.99524	1.0000	31.2330	$x_{F,16}$
^{17}O	0.00038	$^{17}O^{16}O$	0.00076	1.0022 ± 0.001	31.2305	$x_{F,17}$
^{18}O	0.002	$^{18}O^{16}O$	0.002	1.0045 ± 0.004	31.2285	$x_{F,18}$

Table 7.1: Natural abundance of oxygen isotopes and molecules and relative volatilities between each molecule and $^{16}O^{16}O$.

focusing on molecular oxygen and CO (in gaseous form). Regarding the case of O_2, we will investigate the short-term capabilities of the Seruci-1 distillation column. Thus, we fundamentally are asking whether, immediately after the completion of the most significant distillations for basic research, namely the distillation of argon, we can proceed, based on current knowledge and data, to the distillation of oxygen isotopes. Conversely, the situation is more complex concerning CO, as its production would be particularly challenging with the Seruci-1 column. In this case, we prefer a long-term analysis that also keeps under consideration the construction of new structures around Seruci-1 and working under reasonable but yet unexplored conditions. In this way, we will completely cover the future of the Aria project after argon distillation, both in the short and long term. Furthermore, the pressure and column flow values used will be the lowest we have been able to obtain with Seruci-0. By choosing a lower pressure, we know that the equilibrium temperature of the liquid-vapor would also be lower, which would lead to a higher relative volatility according to the study of previous paragraphs on volatility. However, since we are studying a more realistic case based on known knowledge, we prefer not to work at too low a pressure, which would be more complicated to maintain stability in the plant and would have a high energy cost. Therefore, we choose to use the lowest pressure that we are sure we have been able to reach. Similarly, regarding the column flow rate, we used what has been obtained during the argon run of Seruci-0, rescaled to keep under consideration the density of oxygen which is different from the density of argon.

Parameters	Value
P	1.54 bar
T	94.4 K
F	1-20 kg/h
L	445 kg/h
$x_{B,18}$	0.9
N	2000
Nr	0-300

Table 7.2: Column parameters used for the first simulation of Seruci-1 for oxygen distillation.

In the next table 7.1 is the natural concentration of the oxygen isotopes in nature. We are going to refer to the molecular concentration (different from the isotopic one) as $x_{F-B-D,i}$, where the first subscript is the location (F for feed, B for bottom, and D for top) and i indicates the molecule (16 for $^{16}O^{16}O$, 17 for $^{17}O^{16}O$, and 18 for $^{18}O^{16}O$). The relative volatility between $^{16}O^{16}O$ and $^{18}O^{16}O$ is calculated by fitting the results of two different sources in and is calculated at T=94.4 ± 0.01 K and P 1.54 ± 0.01 bar. The relative volatility for $^{17}O^{16}O$ is calculated using equation 4.21. Other isotope combinations

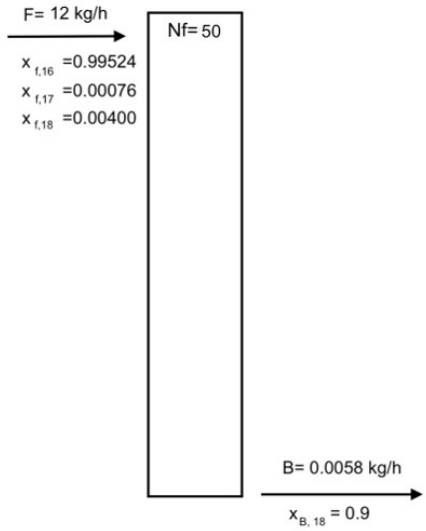

Figure 7.2: Schematic representation and nomenclature of the $^{18}O^{16}O$ double distillation.

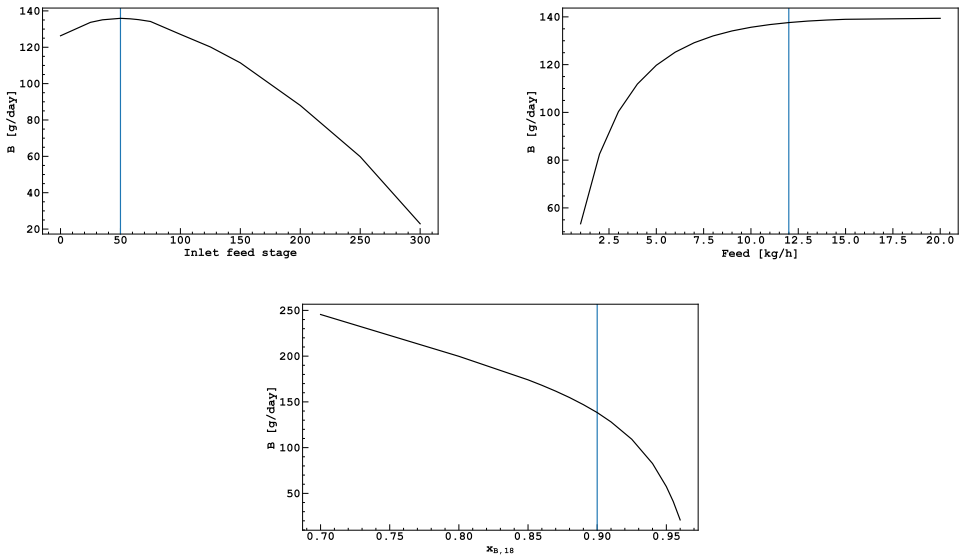

Figure 7.3: Using the input parameters of table 7.2 and simulating in Hysys. On the top left is what we distillate from the bottom of the column as a function of the location where we put the inlet feed. On the top right is the same quantity as a function of the inlet mass flow, and at the bottom, it is as a function of the purity of $^{18}O^{16}O$

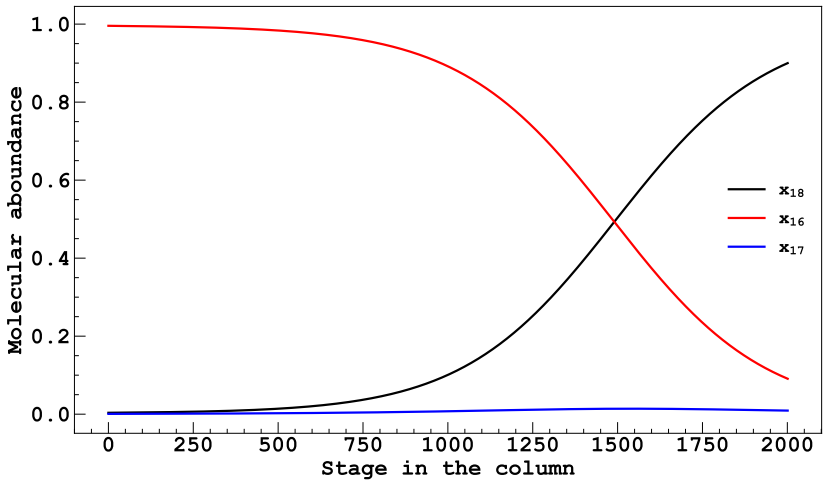

Figure 7.4: Distribution of the concentration of $^{16}O^{16}O$, $^{17}O^{16}O$, and $^{18}O^{16}O$ in the column. In the conditions of table 7.3

($^{17}O^{17}O$ and $^{18}O^{18}O$) may be present only with much lower concentrations and are therefore neglected. Other column parameters are in 7.2: the pressure is based on the lowest we obtained during the previous Seruci-0 runs. L is the one used during run B of argon distillation. The total number of stages is the height of the packing of Seruci-1 (267 m) divided by the HETP=13 cm. Other parameters such as the input feed stage (Nr) and the feed flow rate are going to be optimized to maximize the production rate of oxygen with 0.9 purity when extracted from the bottom of the column ($x_{B,18}$).

Using the conditions of 7.2 we started an optimization of the parameters of the column. In particular, we temporarily set the inlet feed to 10 kg/h and the required concentration of isotope 18 ($x_{B,18}$) to 0.9. We proceeded by performing different simulations for different positions of the inlet feed (i.e., the height (or stage) at which the feed is inserted), identifying at Nr=50 the position that maximizes the flow extraction from the bottom of the column (7.3, top left). We then repeated the previous procedure also with the incoming flow in kg/h. In this case, there is no maximum to the distribution; however, we note that as we increase the feed F more and more, the flow B would gradually saturate and stabilize to a constant value. Therefore, increasing F too much would lead to a non-significant increase in B and a waste of a lot of oxygen. To avoid this, we chose a compromise value of F=12 kg/h corresponding approximately to the flow beyond which the saturation of B begins, (7.3, top right). We emphasize that changing the optimization parameters has not significantly altered the previous measurements. For example, the optimization of the input feed was done using F=10 kg/h, which was later changed to F=12 kg/h. However, this did not significantly change the value Nr for which production is maximized. There may be some differences but since it is difficult to practically identify at what height the different stages correspond, we do not consider it to be a problem in practice. Finally, as always happens in distillation columns due to the equations of mass conservation, as the required purity increases the production rate decreases. For this reason, in (7.3, bottom), we have the trend of the distilled flow from the bottom of column B as a function of $x_{B,18}$. As explained by sources such as [133] and [141], for the applications in the field of medical physics, the

required purity of the molecule with isotope 18 is 90% or 95%. In the second case, as seen from the graph, the production rate would be very low; therefore, we prefer to work in the case of 90%. A schematic representation of the distillation of $^{18}O^{16}O$ in seruci-1 is in picture 7.4.Considering the column in the conditions of 7.2 and having optimized Nr=50, F=12 kg/h, and $x_{B,18} = 0.9$ we get the results in 7.3 and distribution of the concentrations inside the column as in picture 7.4 We note that by optimizing the column and putting

Output steam mass flows			
	F (kg/h)	D (kg/h)	B (kg/h)
	12.0000	11.9942	0.0058
Compositions			
	F	D	B
$^{16}O^{16}O$	0.9976	0.9957	0.0908
$^{17}O^{16}O$	0.00076	0.0008	0.0092
$^{18}O^{16}O$	0.0040	0.036	0.9

Table 7.3: Results of the simulation after optimization for $^{18}O^{16}O$ production.

ourselves in realistic conditions based on the experimental results of Seruci-0, it is possible to obtain a significant production of isotope 18 at 90%, equal to 140 g/day, or 50 kg/year. Considering that global production of isotope 18 from 2000-4000 kg/year ([136]) had been estimated in the past, the production of Aria could constitute from 1% to 2% of the world production.

We also note how the column distribution of the other isotopes is such as not to give us the possibility of significantly separating isotope 17. This presents a peak around stage 1500 but still at a concentration of less than 1%. Therefore, we will consider a double distillation aimed at enriching the $^{17}O^{16}O$ molecule as much as possible. In 7.5 is a schematic representation and nomenclature of the $^{17}O^{16}O$ double distillation. Where we are referring

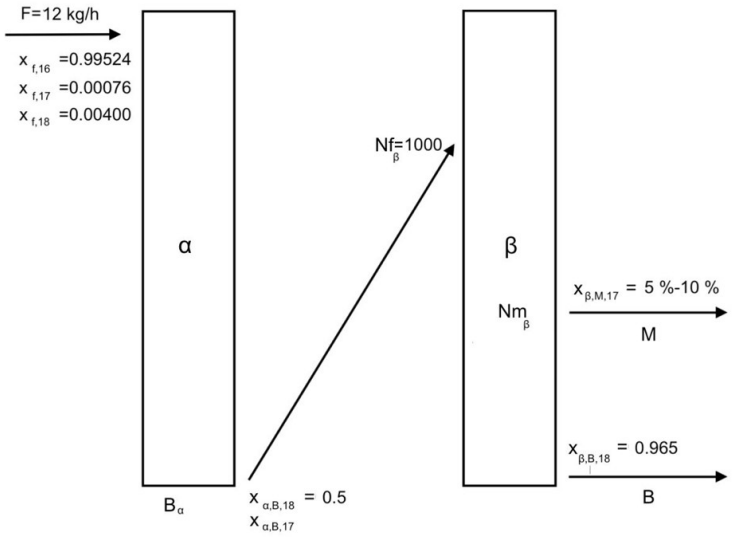

Figure 7.5: Schematic representation and nomenclature of the $^{17}O^{16}O$ double distillation.

to run α as the first run and β as the second and, as they are two different runs of the

same column, they must be performed one after the other: from now on we will use the same nomenclature as before but introducing the subscript α and β to refer to the first and second run. What we distillate from the bottom of the column during the first run will be used as the feed for the next one; during the second distillation we will have one more extraction point in an intermediate position of the column whose goal is going to be the extraction of the isotope 17 and we will refer to this extraction point as M. In terms of flow inside column L, pressure P, and temperature T the two runs are identical. The conditions of the first run are in table 7.4. Here we need to optimize only one parameter

Parameters	Value
P	1.54 bar
T	94.4 K
F	12 kg/h
L	445 kg/h
$x_{\alpha,B,18}$	0.1-0.9
N	2000
Nr	50

Table 7.4: Conditions of the first run α for $^{17}O^{16}O$ distillation

which is the required concentration of $^{18}O^{16}O$ extracted from the bottom to maximize the concentration of the other isotope $^{17}O^{16}O$. This is what has been done in the picture top left in 7.6 for $x_{\alpha,B,18} = 0.5$.

With the input parameters of 7.4 and $x_{\alpha,B,18} = 0.5$ we simulated with Hysys and obtained the results in tabular 7.5.

Output steam mass flows			
	F (kg/h)	D (kg/h)	B (kg/h)
	12.0000	11.9849	0.0151
Compositions			
	F	D	B
$^{16}O^{16}O$	0.9976	0.9959	0.4728
$^{17}O^{16}O$	0.00076	0.0007	0.0272
$^{18}O^{16}O$	0.0040	0.0034	0.5

Table 7.5: Results of the simulation after optimization of the run α for $^{17}O^{16}O$ production.

Then, by inserting what was extracted from below back into the column, we are in the conditions of table 7.6 and we can proceed with two further optimizations. The first concerns the value of $x_{\beta,B,18}$, i.e. the concentration of the molecule with isotope 18 extracted from the column in the second run. In particular, it is found that for $x_{\beta,B,18} = 0.965$ the peak height of isotope 17 inside the column is maximized. Finally, the intermediate extraction point that maximizes $^{17}O^{16}O$ extraction changes depending on the required $^{17}O^{16}O$ concentrations. In particular, we find that when we ask for isotope 17 at 5%, it is convenient to extract around stage 1300, while when we ask for isotope 17 at 10%, it is convenient to extract around stage 1000. About the feed input stage for the second run, it has been noted that this does not alter the concentration or production rate of isotope 17, but only the position of the peak, and therefore we have fixed it at an arbitrary and intermediate value in the column, i.e. at 1000 stages.

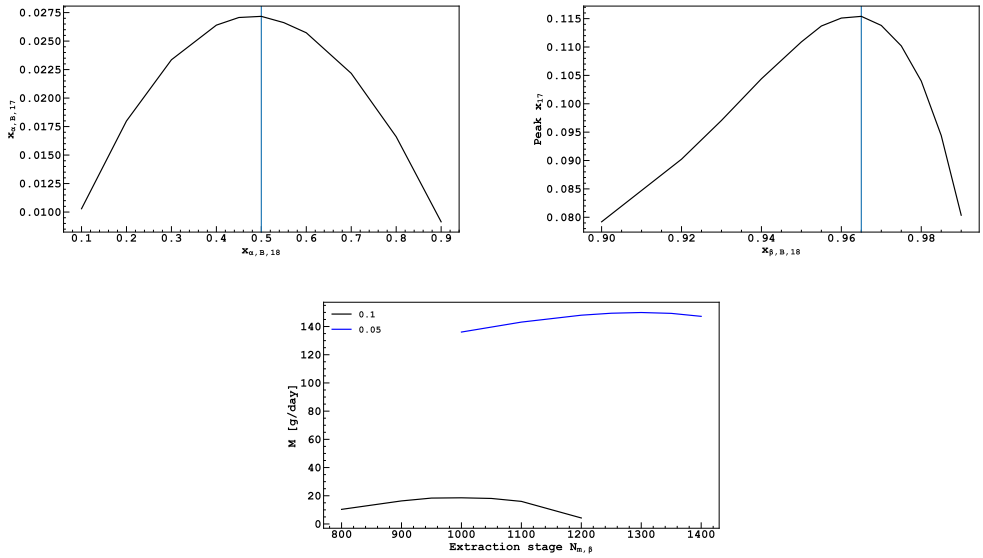

Figure 7.6: Using the input parameters of table 7.4 and simulating in Hysys. Top-left is the concentration $x_{\alpha,B,17}$ as a function of $x_{\alpha,B,17}$ both extracted from the bottom of the first run α. The top right is the peak of isotope 17 concentration as a function of the required concentration extracted from the bottom of the column during the second run 7.7. At the bottom is the flow rate at the intermediate extraction point M as a function of the stage where the extraction is occurring. This is performed for $x_{\beta,M,17} = 0.1$ and $x_{\beta,M,17} = 0.05$.

Finally in the following tables 7.7 and 7.8 we find a summary of the extractions rates and concentrations respectively for $x_{\beta,M,17} = 5$ % and $x_{\beta,M,17} = 10$ %. In 7.7 is the concentration distribution for the case $x_{\beta,M,17} = 10$ % where we notice how we are extracting from the stage corresponding to the peak of isotope 17 concentration. Overall we expect to be able to produce circa 150 g/day or 55 kg/year of $^{17}O^{16}O$ 5% and 18 g/day or 6-7 kg/year of $^{17}O^{16}O$ 10%. As suggested by [142] $^{17}O^{16}O$ enrichment at 3.7 % is already enough for Oxygen-17 Magnetic Resonance.
Higher concentrations would be disadvantageous in terms of production rate. Additionally, we observe that simultaneous extraction from the bottom would lead to a high concentration of isotope 18, reaching 96.5%. Therefore, by conducting two runs, we would be able to extract both isotope 17 from an intermediate zone of the column and isotope 18 from below simultaneously.

In summary, it is possible to use the Seruci-1 column under conditions already tested with Seruci-0 to produce significant quantities of oxygen isotopes 17 and 18. One option, which can be achieved more quickly and easily, is to perform a single distillation and extract molecule $^{18}O^{16}O$ at 90% from under the column, producing approximately 50 kg/year. Alternatively, two consecutive distillations can be performed. In this case, the second distillation would allow us to extract either 55 kg/year of $^{17}O^{16}O$ at 5% from an intermediate extraction point on the column and 30 kg/year of $^{18}O^{16}O$ at 96.5% from below, or 6-7 kg/year of $^{17}O^{16}O$ at 10% and 65 kg/year of $^{18}O^{16}O$ at 96.5%. However, in the case of double distillation, it would be necessary to conclude the first distillation before proceeding to the second, significantly increasing the required time.

Parameters	Value
P	1.54 bar
T	94.4 K
F	0.01514 kg/h
L	445 kg/h
xβ,B,18	0.9-0.99
xβ,M,17	5%-10%
N	2000
Nf$_\beta$	1000
Nm$_\beta$	800-1400

Table 7.6: Conditions for the second run β of $^{17}O^{16}O$ distillation

Output steam mass flows				
	F (kg/h)	D (kg/h)	B (kg/h)	M (kg/h)
	0.0151	0.007069	0.007312	0.0007539
Compositions				
	F	D	B	M
$^{16}O^{16}O$	0.4728	0.9662	0.0086	0.3498
$^{17}O^{16}O$	0.02726	0.0202	0.0264	0.1000
$^{18}O^{16}O$	0.5	0.0136	0.9650	0.5502

Table 7.7: Results of the simulation after optimization of the run β for $^{17}O^{16}O$ production. Requiring $x_{\beta,M,17} = 5$ %

7.2 CO and NO distillation

In this chapter, we are going to develop a method for the production of stable isotopes of carbon, nitrogen, and oxygen via cryogenic distillation using very tall cryogenic distillation towers. The isotopes of interest are ^{13}C, ^{15}N, ^{17}O, and ^{18}O. The Aria technology for the construction of the distillation columns, originally developed for the separation of argon isotopes required by the DarkSide dark matter search program, allows the construction of very tall cryogenic distillation towers. We will focus on the production of the isotopes of interest via the distillation of carbon monoxide (CO) and nitric monoxide (NO). The distillation of the isotopes is carried out in two separate steps through two different columns. In particular, in addition to the previously described and discussed Seruci-1, we consider the possibility of complementing it with a narrower column of the same height. This proposed column incorporates a more modern and recently commercialized internal packing known as low-flow Cannon Instrument Company Pro-Pak packing, or simply Pro-Pak [143]. It is noteworthy that the internal structure of the mine already possesses dimensions able to accommodate a second column, and the expansion of the Aria project in this manner was already taken into account. In this chapter, we specifically discuss the hypothesis that this column, referred to as *Seruci-F*, is 350 m tall overall (including the packing), with a diameter of 12 cm, and composed of Pro-Pak. The HETP for this packing material measures 3 cm, as opposed to the 12 cm of the packing used for Seruci-1, thus ensuring a greater capability of separating elements with low relative volatility. However, the smaller diameter constrains the flow in the column, consequently reducing the distillation rate. Summarizing the two steps of CO and NO distillation we proceed as follows:

Output steam mass flows				
	F (kg/h)	D (kg/h)	B (kg/h)	M (kg/h)
	0.0151	0.005421	0.003460	0.006254
Compositions				
	F	D	B	M
$^{16}O^{16}O$	0.4728	0.9863	0.0172	0.2798
$^{17}O^{16}O$	0.02726	0.0069	0.0177	0.05
$^{18}O^{16}O$	0.5	0.0069	0.9650	0.6702

Table 7.8: Results of the simulation after optimization of the run β for $^{17}O^{16}O$ production. Requiring $x_{\beta,M,17} = 10$ %

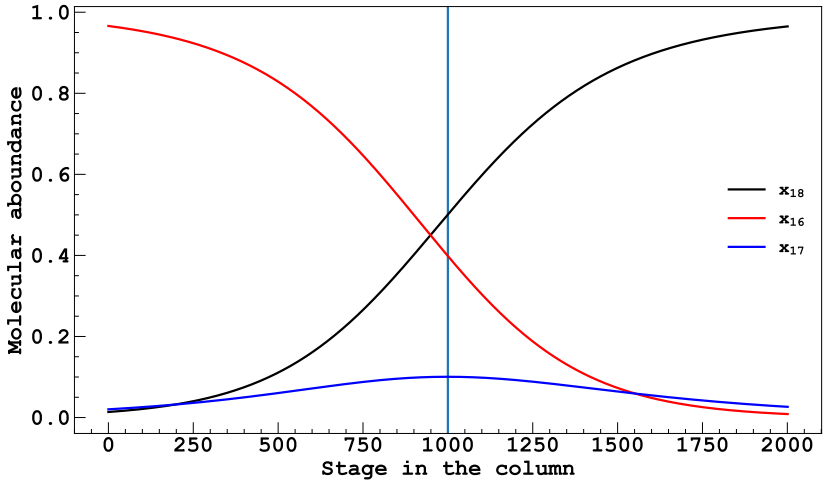

Figure 7.7: Distribution of the concentration of $^{16}O^{16}O$, $^{17}O^{16}O$, and $^{18}O^{16}O$ in the column for the second run */beta*. In the conditions of table 7.6 and for $x_{\beta,M,17} = 10$ %.

1. In the first step, we significantly reduce the dominant components, $^{12}C^{16}O$ and $^{14}N^{16}O$, by using the previously described Seruci-1 column, designed for argon distillation.

2. In the second step, we carry out a chromatographic separation of the Seruci-1 output stream via Seruci-F, a second cryogenic distillation column characterized by its 350-meter height, 12-cm diameter, low-flow Cannon Instrument Company Pro-Pak packing, and 3-cm HETP, providing circa 11,000 equilibrium stages in its normal operating conditions. To carry out the detailed simulation of the two columns we use Aspen Hysys [121].

7.3 CO isotopic distillation parameters for Seruci-1 and Seruci-F

In Hysys libraries [121] are defined the Antoine parameters for a CO molecule 4.15:

1. a = 41.6550

2. b = -1109.8

3. c = 0
4. d = 5.45484
5. e = 0.0000864
6. f = 2

Using these parameters for the Antoine equation we calculated the temperature at a pressure of 1 bar, that is 81.58 K, and the relative volatility of the isotopes of CO (4.21 is exploited as well). In the next table we always refer to the relative volatility between the molecule written in the column and the most commune molecular isotope that is $^{13}C^{16}O$ and are at T = 81.58 K. Notice how different isotopes with the same mass have the same relative volatility.

Isotope	α
$^{13}C^{16}O$	1.00692
$^{12}C^{17}O$	1.00692
$^{13}C^{17}O$	1.01384
$^{12}C^{18}O$	1.01384
$^{13}C^{18}O$	1.02076

Table 7.9: Relative volatility for CO isotopes (all refer to $^{13}C^{16}O$) at T = 81.58 K .

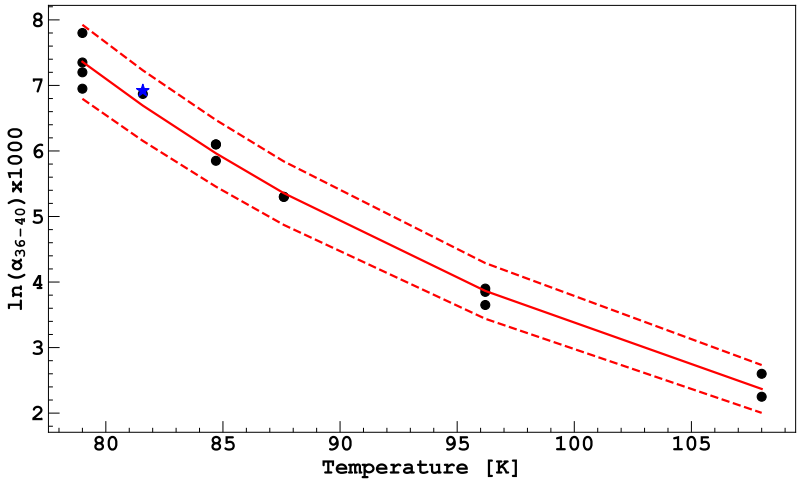

Figure 7.8: Relative volatility between $^{13}C^{16}O$ and of $^{12}C^{16}O$ as a function of the temperature. Black dots refer to [119], the red lines are the result of the fit with a function like 4.23 and the error band (dotted), and the blue star corresponds to T=81.58 K and α=1.00692 and is the one we are going to use in the next calculations.

As further validation of the parameters and relative volatilities, we compared our results with those of [119]. By fitting the measures of the paper and calculating the error we obtain (7.8). Here, the zone between the dotted lines represents the error band and we notice how the point corresponding to T=81.58 K and α=1.00692 (the one we are going to use for the next simulations) falls inside this area.

Finally, we set the Antoine parameters of the other isotopes such that the ratio of the logarithm of the pressures, that is the relative volatility, is equal to the required value. The parameters are summarized in the following tabular.

Isotope	a
$^{12}C^{16}O$	41.65500
$^{13}C^{16}O$	41.64810
$^{12}C^{17}O$	41.64810
$^{13}C^{17}O$	41.64125
$^{12}C^{18}O$	41.64125
$^{13}C^{18}O$	41.63445

Table 7.10: Antoine parameters used for CO. All the other parameters are kept the same.

However, considering Seruci-F, it will be preferable to use a much lower pressure (160 mbar) which corresponds to a temperature of 68.33 K for $^{12}C^{16}O$ and the relative volatility will change accordingly.
However, as Seruci-F will have 11480 stages, Hysys would not be able to simulate properly such a large number of equations. So, to get around the problem, we recall the equations of Fenske 4.55 and the definition of separation 4.2. Thus if we elevate the volatility at the power of a certain factor q we can divide the stages by the same value and still get the same separation.

$$S = \alpha^{N_{min}} = (\alpha^q)^{N_{min}/q} \tag{7.1}$$

In our case, we reduced the number of stages by a factor q = 4 (to obtain the same amount as for Seruci-1) and elevated the volatilities of all the isotopes by the same value. We then looked again for Antoine's parameters to obtain the required volatility.

Isotope	α	a
$^{12}C^{16}O$	1.0000	41.65500
$^{13}C^{16}O$	1.0446	41.61136
$^{12}C^{17}O$	1.0446	41.61136
$^{13}C^{17}O$	1.0892	41.56955
$^{12}C^{18}O$	1.0892	41.56955
$^{13}C^{18}O$	1.1334	41.52942

Table 7.11: Antoine parameters used for CO in Seruci-F and relative volatilities.

7.3.1 NO isotopic distillation parameters for Seruci-1

In [144] is given the equation of the Pressure (in cmHg) as a function of the temperature for $^{14}N^{16}O$

$$\log(P(\text{cmHg})) = -\frac{776}{T(\text{K})} - 0.002364 \cdot T + 8.566128 \tag{7.2}$$

For simplicity, we write the equation as follows:

$$\log(P(\text{cmHg})) = -\frac{A}{T(K)} - B \cdot T + C \tag{7.3}$$

Where

$$A = 776$$

$$B = 0.002364$$

$$C = 8.562128$$

We want to modify these parameters to write it in the formulation of equation 4.15. As a first step, we move from cmHg to kPa and change to base of the logarithms to the natural one.

$$\log(P(\text{cmHg})) = \log(\frac{P(\text{kPa})}{1.33})$$

$$\log(P(\text{kPa})) - \log(1.33) = -\frac{A}{T} - B \cdot T + C + \log(1.33)$$

$$\log(P(\text{kPa})) = -\frac{A}{T} - B \cdot T + C + \log(1.33)$$

Summarizing

$$\log(P(\text{kPa})) = -\frac{776}{T} - 0.002364 \cdot T + 8.68598 \tag{7.4}$$

Then

$$\ln(P(\text{kPa})) = \frac{\log(P(kPa)}{\log(e)}$$

$$\ln(P(\text{kPa})) = -\frac{776T - 0.002364 \cdot T + 8.68598}{\log(e)}$$

$$\ln(P(\text{kPa})) = -\frac{1786.806}{T} - 0.005443 \cdot T + 20.00021 \tag{7.5}$$

Therefore, using the parameters of 4.15

1. a = 20.00021
2. b = -1786.806
3. c = 0
4. d = 0
5. e = 0.005443
6. f = 1

So, once the parameters for the first isotope have been found, we now look for all the others.

In [145] are shown the following equations:

$$\log(\frac{P_{^{14}\text{N}^{16}\text{O}}}{P_{^{15}\text{N}^{16}\text{O}}}) = \frac{3.042}{T} - 0.01353 \tag{7.6}$$

$$\log(\frac{P_{^{14}\text{N}^{16}\text{O}}}{P_{^{14}\text{N}^{18}\text{O}}}) = \frac{4.399}{T} - 0.02042 \tag{7.7}$$

$$\log(\frac{P_{^{14}\text{N}^{16}\text{O}}}{P_{^{15}\text{N}^{18}\text{O}}}) = \frac{7.441}{T} - 0.03395 \tag{7.8}$$

$$\log(\frac{P_{^{14}\text{N}^{16}\text{O}}}{P_{^{14}\text{N}^{17}\text{O}}}) = \frac{2.200}{T} - 0.01021 \tag{7.9}$$

$$\log(\frac{P_{^{14}\text{N}^{16}\text{O}}}{P_{^{15}\text{N}^{17}\text{O}}}) = \frac{5.241}{T} - 0.02374 \tag{7.10}$$

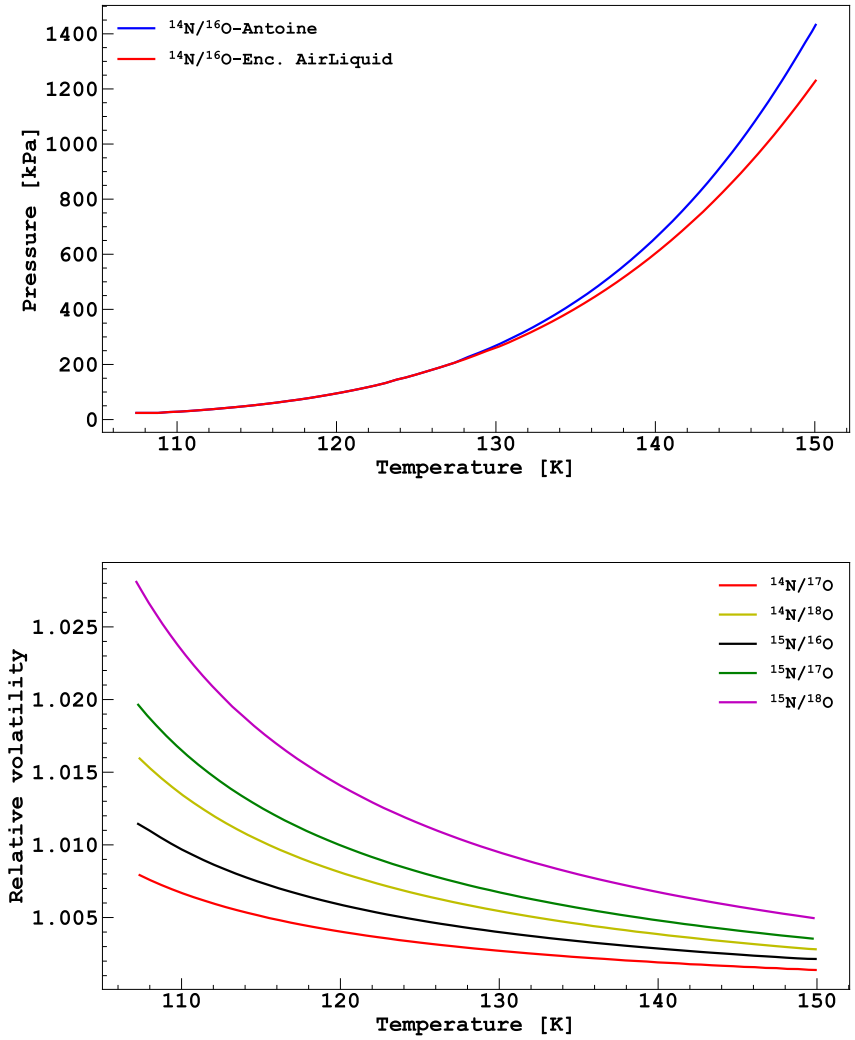

Figure 7.9: Pressure vs temperature for $^{14}N^{16}O$ (up), for all the NO isotopes (down).

Each of these equations can be generically written as

$$\log(\frac{P_{^{14}N^{16}O}}{P_{^{i}NO}}) = \frac{\alpha_i}{T} - \beta_i \tag{7.11}$$

Where β_i is negative. As in the previous case we switch to natural logarithm.

$$\alpha_i' = \frac{\alpha_i}{log(e)}$$

$$\beta_i' = \frac{\beta_i}{log(e)}$$

Thus we can write

$$\ln(\frac{P_{^{14}N^{16}O}}{P_{^{i}NO}}) = \frac{\alpha_i'}{T} - \beta_i' \tag{7.12}$$

Looking for P_i we obtain:

$$\ln(P_{^{14}N^{16}O}) - \ln(P_{^{i}NO}) = \frac{\alpha_i'}{T} + \beta_i'$$

$$\ln(P_{^{i}NO}) = \frac{\alpha_i'}{T} + \beta_i' + a + e \cdot T + \frac{b}{T}$$

$$\ln(P_{^{i}NO}) = (a + \beta_i') + \frac{(b + \alpha_i')}{T} + e \cdot T \tag{7.13}$$

Therefore, to obtain Antoine's parameters, it is sufficient to add the values of a and b respectively to β_i' and α_i' for each isotope. The parameters are summarized in the following table:

Isotope	a	b	e	
$^{14}N^{16}O$	20.0002	-1786.8	-0.0054	1
$^{15}N^{16}O$	20.0314	-1793.8	-0.0054	1
$^{14}N^{17}O$	20.0237	-1791.9	-0.0054	1
$^{15}N^{17}O$	20.0549	-1798.9	-0.0054	1
$^{14}N^{18}O$	20.0472	-1796.9	-0.0054	1
$^{15}N^{18}O$	20.0784	-1803.9	-0.0054	1

Table 7.12: Antoine parameters used for NO.

The following graphs show the pressure and the relative volatilities as functions of the temperature according to these parameters and calculated via the Antoine equation. In [146] are represented the main properties of NO. Based on this and knowing that we want to perform a distillation (and therefore we are interested in the liquid-gas separation line) we limited our calculations to the range going from 108 K to 150 K. In 7.9, is represented the pressure as a function of the temperature calculated with our parameters and given by [146]: the two graphs show an excellent agreement, especially for lower temperatures.

Moreover, as a further validation of the chosen parameters, we can notice how the trend of both pressure and volatility has the shape we expected as a function of the temperature, and how these values are realistic along the range 108 K - 150 K. As further confirmation of the results just obtained, we check their compatibility with [147] measures. In (7.10) is shown how the pressure changes within the temperature in a smaller range. This function, for each isotope, is compared with the measures of [147]: in both cases is highlighted a perfect overlapping between our and their graph.

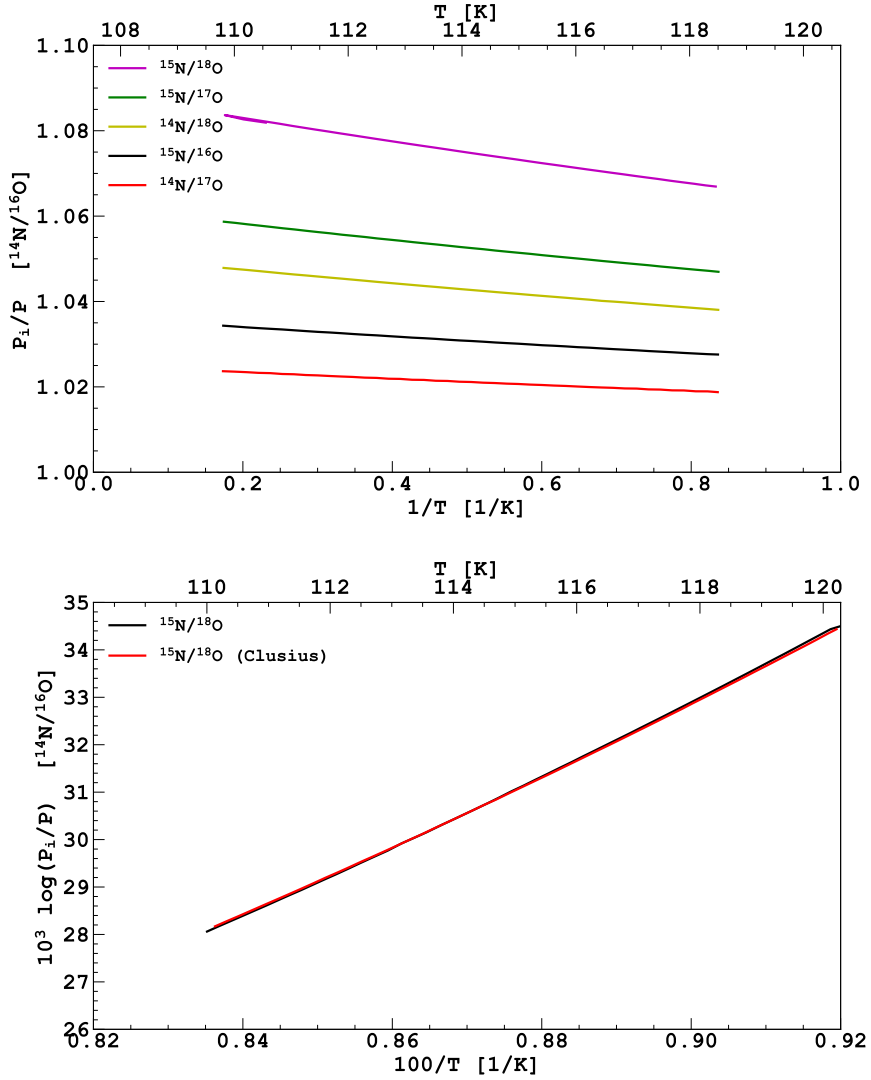

Figure 7.10: Pressure as a function of the temperature for NO isotopes. In the bottom figure we compare our calculations with [147], showing a perfect agreement.

Isotope	α
$^{14}N^{16}O$	1.00000
$^{15}N^{16}O$	1.005802
$^{14}N^{17}O$	1.003976
$^{15}N^{17}O$	1.009820
$^{14}N^{18}O$	1.007978
$^{15}N^{18}O$	1.013874

Table 7.13: Relative volatility for NO isotopes (always with respect to $^{13}N^{16}O$) at T = 121.3 K used for Seruci-1.

Isotope	α
$^{14}N^{16}O$	1.000000
$^{15}N^{16}O$	1.039698
$^{14}N^{17}O$	1.027288
$^{15}N^{17}O$	1.068325
$^{14}N^{18}O$	1.055486
$^{15}N^{18}O$	1.097971

Table 7.14: Relative volatility for NO isotopes at T = 111.74 K used for Seruci-F, all are concerning $^{14}N^{16}O$.

7.3.2 NO isotopic distillation parameters for Seruci-F

In Seruci-F P = 300 mbar and T = 111.7 K, we used the formulas of the previous subsection to find the relative volatilities under these conditions. The values of α are the following.

Proceeding in the same way as for CO we elevate the relative volatility at the power of 4 while keeping the same number of stages. Subsequently, an attempt was made to modify the parameters of Antoine in such a way as to obtain these relative α values. By changing the parameters a and b of the Antoine equation of each isotope (except the lightest, whose parameters are kept unchanged) it is possible to ensure that the resulting volatility is the fourth power of the initial one for a certain temperature value (in our case T = 111.74 K). However, this is no longer valid for different temperatures. It will therefore be necessary to choose parameters that will change α to its fourth power at T = 111.74 K and for which this relationship is as true as possible in the temperature range of the column. In other words, the difference between the relative volatility given by Antoine and α^4 must be 0 for T =111.74 K and as small as possible for the other temperatures of the column. By making several attempts it has been noticed that this discrepancy is minor by modifying only the b parameter and therefore the following parameters have been chosen. The pressure

Isotope	b
$^{14}N^{16}O$	-1786.806
$^{15}N^{16}O$	-1801.3175
$^{14}N^{17}O$	-1796.9015
$^{15}N^{17}O$	-1811.1127
$^{14}N^{18}O$	-1806.7854
$^{15}N^{18}O$	-1820.7183

Table 7.15: Antoine parameters used for NO in Seruci-F, all the others are left unchanged.

as a function of the temperature given by these parameters is in (7.11, up). Using these parameters the relation between temperature and pressure changes: at P=300 mbar will correspond to a different temperature for each isotope.

Isotope	Temperature (K)
$^{14}N^{16}O$	111.74
$^{15}N^{16}O$	112.68
$^{14}N^{17}O$	112.40
$^{15}N^{17}O$	113.32
$^{14}N^{18}O$	113.04
$^{15}N^{18}O$	113.95

Table 7.16: Temperature corresponding to P = 300 mbar for NO isotopes.

From this, it is clear that the temperature, in the areas of the column with a prevalence of the heavier isotope, can reach at most 113.95 K. In (7.11, down) is represented the discrepancy between $\ln(\alpha)$ given by Antoine equation with the parameters of NO (Seruci-F) and the expected $\ln(\alpha^4)$: at T = 111.74 K. The difference is of course 0 as the parameters have been calibrated at this temperature. However, in the range of the column (111-114) K we notice how the discrepancy is always <7 % for each isotope. Therefore we can affirm that, considering our type of column, these parameters allow us to obtain a good approximation α^4 for each possible temperature, thus simulating a column with 4 times the actual number of stages.

7.3.3 Optimization for CO in Seruci-1

We performed several simulations searching for the best extraction to use as input for the second column: the main goals consist of both maximizing the production rate from the bottom of Seruci-1 and minimizing the concentration of the lightest element ($^{12}C^{16}O$): a compromise was therefore found between these two requests. The input parameters used for the simulation are summarized in the following tabular. Where F and L are respectively

Parameters	Value
P	1.0 bar
T	81.58 K
F	10 kg/h
L	700 kg/h
$x_{B,^{13}C^{16}O}$	0.2
N	2870
Nr	700

Table 7.17: Input parameters used to simulate CO distillation in Seruci-1.

the input mass flow and the liquid flow inside the column. N represents the total number of stages of the column and Nr is the stage corresponding to the input feed. L has been chosen as it is the greatest before making the column incompatible with the hydraulic structure. F has already been saturated, as increasing the input mass flow would not significantly change B. A 20% concentration of ($^{12}C^{16}O$) has been requested in the bottom flow as a result of an optimization procedure. In the next tabular are shown the output results of this simulation. Where are shown the composition and mass flow respectively from the feed F

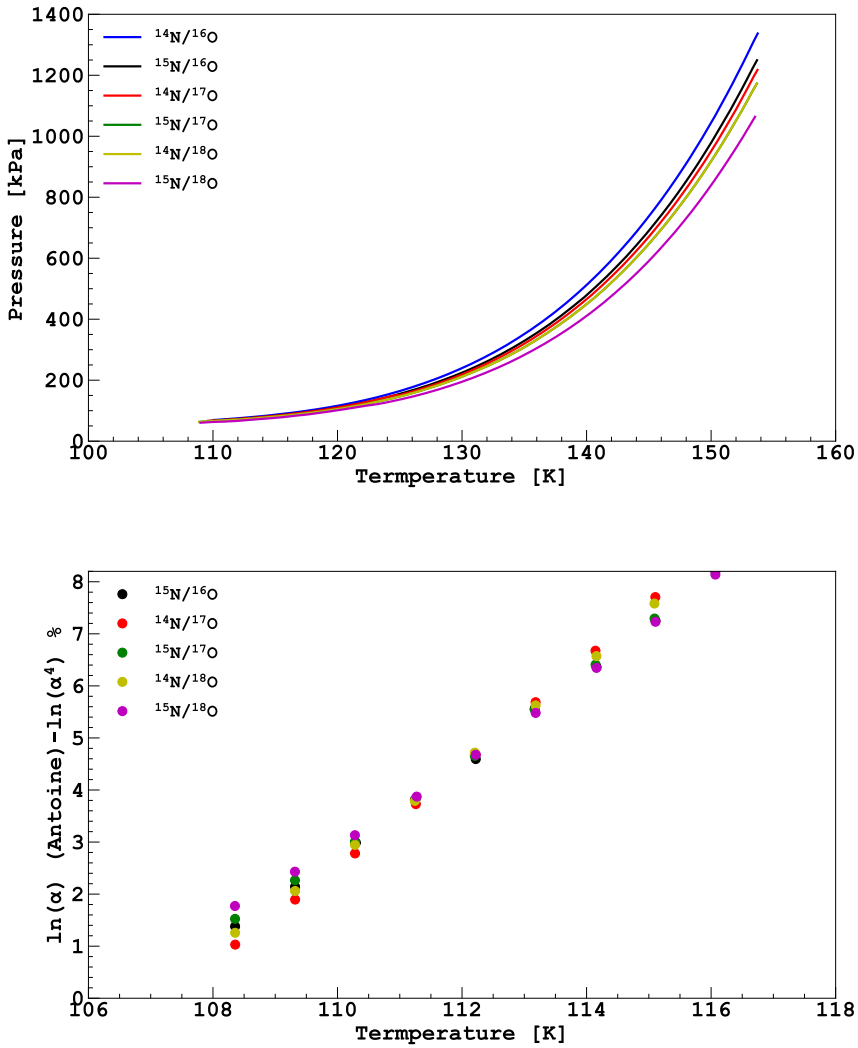

Figure 7.11: Up: pressure as a function of the temperature with the new parameters (NO, Seruci-F). Down: Discrepancy between the α^4 and α given by Antoine equation with the new parameters.

Output steam mass flows			
		D (kg/h)	B (kg/h)
		9.728870	0.271128
Compositions			
	F	D	B
$^{12}C^{16}O$	0.986890	0.994238	0.723442
$^{13}C^{16}O$	0.010670	0.005398	0.200000
$^{12}C^{17}O$	0.000370	0.000190	0.007045
$^{13}C^{17}O$	0,000004	$3.43 \cdot 10^{-07}$	0.000135
$^{12}C^{18}O$	0.002020	0.000174	0.06856
$^{13}C^{18}O$	0.000020	$4.08 \cdot 10^{-08}$	0.000810

Table 7.18: Output parameters used to simulate CO distillation in Seruci-1 and input concentrations (natural abundances).

Component flows			
	F (kg/h)	D (kg/h)	B (kg/h)
$^{12}C^{16}O$	9.868960	9.672813	0.196146
$^{13}C^{16}O$	0.106740	0.052514	0.054226
$^{12}C^{17}O$	0.003760	0.001850	0.001910
$^{13}C^{17}O$	0.000040	0.000003	0.000037
$^{12}C^{18}O$	0.020280	0.001689	0.018591
$^{13}C^{18}O$	0.000220	$3.97 \cdot 10^{-07}$	0.000220

Table 7.19: Output parameters used to simulate CO distillation in Seruci-1.

(input), from the top (D) and bottom (B) (output). The bottom isotopic concentrations are fundamental as they will constitute the input feed for the Seruci-F distillation column. Note above all how the concentration of the most common isotope $^{12}C^{16}O$ has been reduced from 99% to 72%. Therefore Seruci-1, under these conditions, effectively performs a first screening of the isotopes.

7.3.4 Optimization of CO in Seruci-F

The goal of this simulation is to perform a purification of the CO isotopes, to reach a composition of 99% in each extraction point. This is a multi-component simulation with two extraction points at different heights of the column, in particular at the 1362 stage (first line out) and at the 2000 stage (second line out). The height of the column is determined by the depth of the well (in Seruci mine), therefore the height of Seruci-F is expected to be maintained at 287 m like the other column. The current flow extracted from the bottom of Seruci-1 passes through a scrambler which recombines it. By summing the molecules with the same isotopes, the following results are obtained:

The effect of the scrambler is to recombine the isotopes, therefore the new concentration can be obtained by multiplying the isotopes constituting each molecule.

The discussion about the relative volatilities has been done in the previous chapters. Furthermore, it was decided to combine the isotopes having the same molecular mass as they have the same relative volatility as well. Summarizing:

Picture (7.12) represents the general structure of the Seruci-1 distillation column: SP1-M29 and SP1-M30 are the two intermediate extraction feeds, respectively at stages 1362

Isotope	Abundances
^{12}C	0.799055
^{13}C	0.200945
^{16}O	0.923442
^{17}O	0.007180
^{18}O	0.069378

Table 7.20: Atomic abundance after the scrambler.

Isotopes	Abundances
^{12}C^{16}O	0.737881
^{13}C^{16}O	0.185561
^{12}C^{17}O	0.005738
^{13}C^{17}O	0.001443
^{12}C^{18}O	0.055437
^{13}C^{18}O	0.013941

Table 7.21: Molecular abundance after the scrambler.

and 2000. Our goal is to extract with the highest possible purity M31 from B, M30 from SP2, M29 from SP1, and M28 from D. Similarly to what was done for CO, also in this case we proceeded to optimize the column, trying to extract from each of the four feeds a high concentration of the required isotope and with enough kg/h. The following input parameters have been chosen (7.24).

Where SP1 and SP2 are the output feed stage location. x_{Mi} is the concentration of the molecule of molecular mass i in the corresponding feed.
The results are summarized in tabular 5.1.

In which a good production of all the isotopes is obtained both in terms of kg/h and of concentration.
Below are the graphs of the concentration profile as a function of the number of stages, in linear scale and logarithmic scale (7.13). We can notice how, before the feeding point, the concentration of M29, M3, and M31 are decreasing, getting always closer to zero: in the top distillate, we will obtain high purity ^{12}C^{16}O. Further down the column, we see a notably

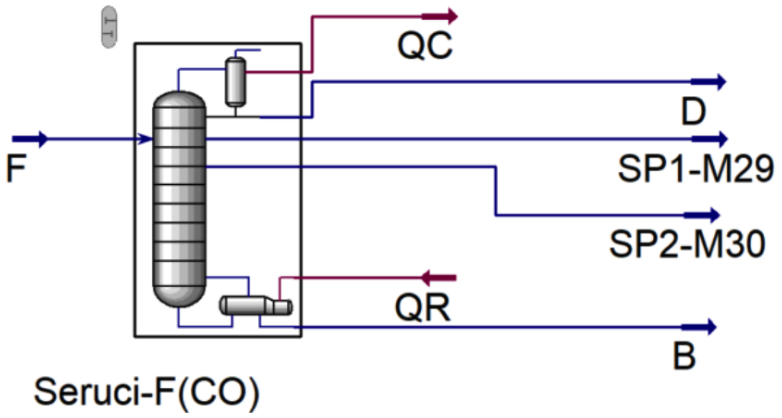

Figure 7.12: General structure of Seruci-F column for CO distillation

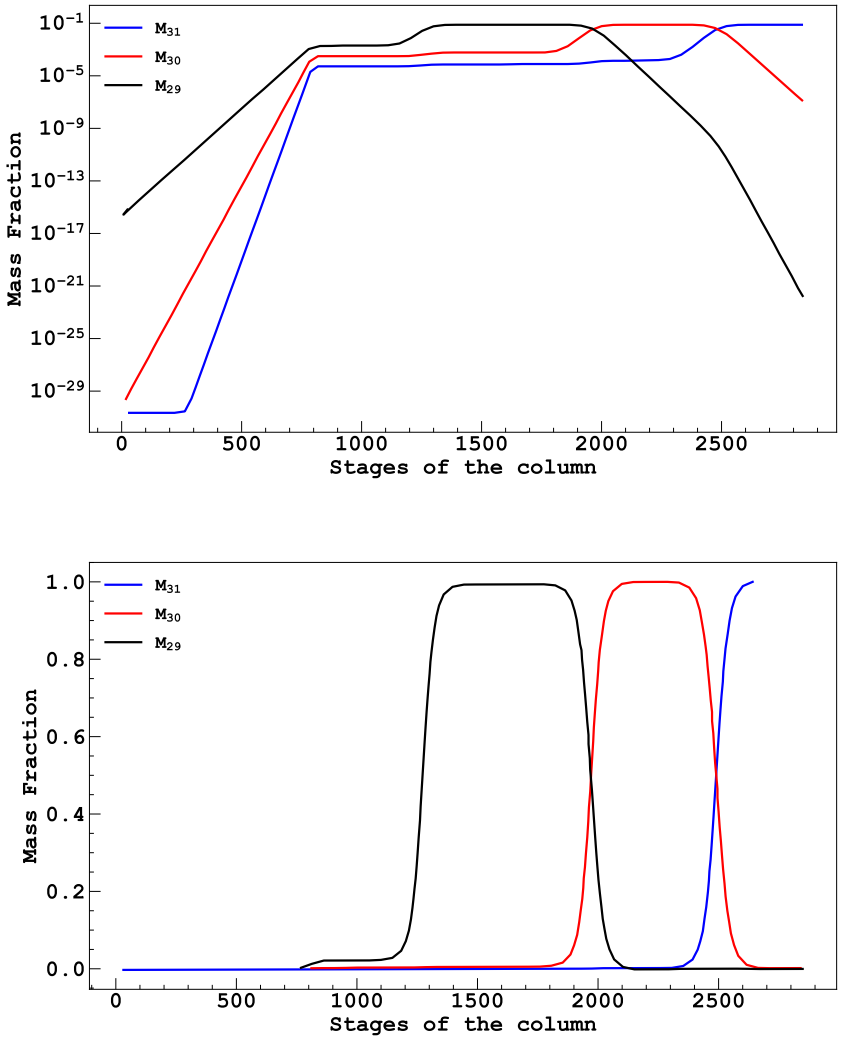

Figure 7.13: Distribution of the isotopes inside the column (bottom in log scale) for Seruci-F (CO).

Isotope	Name	Abund.
$^{12}C^{16}O$	M28	0.737881
$^{13}C^{16}O$+$^{12}C^{17}O$	M29	0.191298
$^{13}C^{17}O$+$^{12}C^{18}O$	M30	0.056879
$^{13}C^{18}O$	M31	0.013941

Table 7.22: Summary of the inputs for Seruci-F.

Input parameter	Values
P	0.160 bar
T	68.33 K
F	0.271 kg/h
L	50 kg/h
x_{M29}	0.99
x_{M30}	0.99
x_{M31}	0.99
SP1	1362
SP2	2000
N	2725
Nr	764

Table 7.23: Input parameters used to simulate CO distillation in Seruci-F.

different situation, in which at different heights we have high concentration plateaus of M29, M30, and M31 respectively. Therefore, by extracting from the bottom of the column and in correspondence with these zones, it is possible to obtain high-purity M29, M30, and M31.

7.3.5 Optimization of NO in Seruci-1

In a similar way to what happened with CO, for NO we will proceed to optimize the distillation of Seruci-1 and Seruci-F in order to maximize the separation of the isotopes. As we can deduce from the previous chapters, the molecules of NO have relative volatility greater than CO and we therefore expect to be able to separate them more easily. As we will see later in this chapter, NO distillation with Seruci-1 will allow us not only to significantly reduce the concentration of the most common isotopes $^{14}N^{16}O$ but also to immediately extract another isotope $^{14}N^{17}O$ at an intermediate height of the column. Therefore another extraction point was added, to collect the isotope $^{14}N^{17}O$ at high purity: we have chosen to call this M and (after an optimization process) to place it in correspondence of the stage Nm = 1325. In the table 7.26 are summarized the parameters used as input after careful optimization. In particular, we notice how increasing both the input feed F and the liquid flow L would significantly improve the distillation by increasing the extraction from the bottom of the column while keeping acceptable isotopic separation. However, the maximum acceptable column flow is 800 kg/h, given the hydraulic structure of Seruci-1 and therefore L has been fixed at this value. Subsequently, different values of the input mass flow were tested: while increasing F we were improving the extraction from the bottom (B) but at the same time the separation among the components was worsening. Eventually, F = 16 kg/h was chosen as a compromise. The results of the optimization are summarized in tabular (7.27):

Where we notice how we can produce 122 g/day (or 44.6 kg/year) of $^{14}N^{17}O$ from the

Output steam mass flows					
		D (kg/h)	SP1 (kg/h)	SP2 (kg/h)	B (kg/h)
		0.199954	0.052264	0.015167	0.003743
Compositions					
	F	D	SP1	SP2	B
M28	0.737882	1.000000	0.002040	$1.39{\cdot}10^{-17}$	$9.03{\cdot}10^{-31}$
M29	0.191298	$1.58{\cdot}10^{-15}$	0.990000	0.008261	$5.48{\cdot}10^{-18}$
M30	0.056879	$3.45{\cdot}10^{-30}$	0.007049	0.989999	0.010000
M31	0.013941	$1.07{\cdot}10^{-30}$	0.000910	0.001740	0.990000

Table 7.24: Output parameters for CO distillation in Seruci-F.

Component flows					
	F (kg/h)	D (kg/h)	SP1 (kg/h)	SP2 (kg/h)	B (kg/h)
M28	0.200060	0.199954	0.000107	$2.11{\cdot}10^{-19}$	$3.38{\cdot}10^{-33}$
M29	0.051866	$3.17{\cdot}10^{-16}$	0.051741	0.000125	$2.05{\cdot}10^{-20}$
M30	0.015422	$6.90{\cdot}10^{-31}$	0.000368	0.015016	0.000037
M31	0.003780	0.003780	0.000048	0.000026	0.003706

Table 7.25: Output mass flows in Seruci-F (CO).

intermediate extraction point with a 93.7 % purity. Similarly, the top of the column leads to 15.9 kg/h of $^{14}N^{16}O$ with 99.994 %. The lighter isotope has been completely removed from the bottom of the column, and therefore what is obtained can be inserted directly into Seruci-F without recombination. Having already isolated high purity $^{14}N^{17}O$ and $^{14}N^{16}O$, the purpose of the last distillation will be, ideally, to separate the four remaining isotope. In pictures 7.14 are shown the distributions of the concentration inside the column: we notice how the column is exploited in its entirety and how the extraction stages have been chosen wisely.

7.3.6 Optimization of NO in Seruci-F

To simplify the simulation, it was decided not to consider isotopes with lower concentrations, that are $^{14}N^{16}O$ and $^{15}N^{17}O$. Not extracting the first is not an issue as it has already been obtained from Seruci-1 (distilled from the top). While $^{15}N^{17}O$ unfortunately cannot be isolated like the other isotopes due to the low initial concentration. We then proceeded similarly to what was done with Seruci-F in the case of CO: the main difference is that for NO we have only one intermediate extraction point at the stage 1950. The parameters used as inputs for this simulation are the following:

Where is required the extraction of ($^{14}N^{18}O$) and ($^{15}N^{18}O$) with very high purity. The outputs of the simulation are the following

Where we can produce $^{15}N^{16}O$, $^{14}N^{18}O$ and $^{15}N^{18}O$) with respectively 99.8 %, 99.9 % and 99.9 % purity from the top, middle and bottom of the column. This distillation, together with Seruci-1 allows us to extract all the isotopes of NO apart from the very rare $^{15}N^{17}O$.

The purpose of this chapter was to show the enormous potential of the Seruci-1 distillation column when coupled with another one of the same height, made of Pro-Pak packing material. We have demonstrated with rigorous simulations how it is potentially possible to separate each isotope of CO having the same molecular mass and five out of six isotopes of

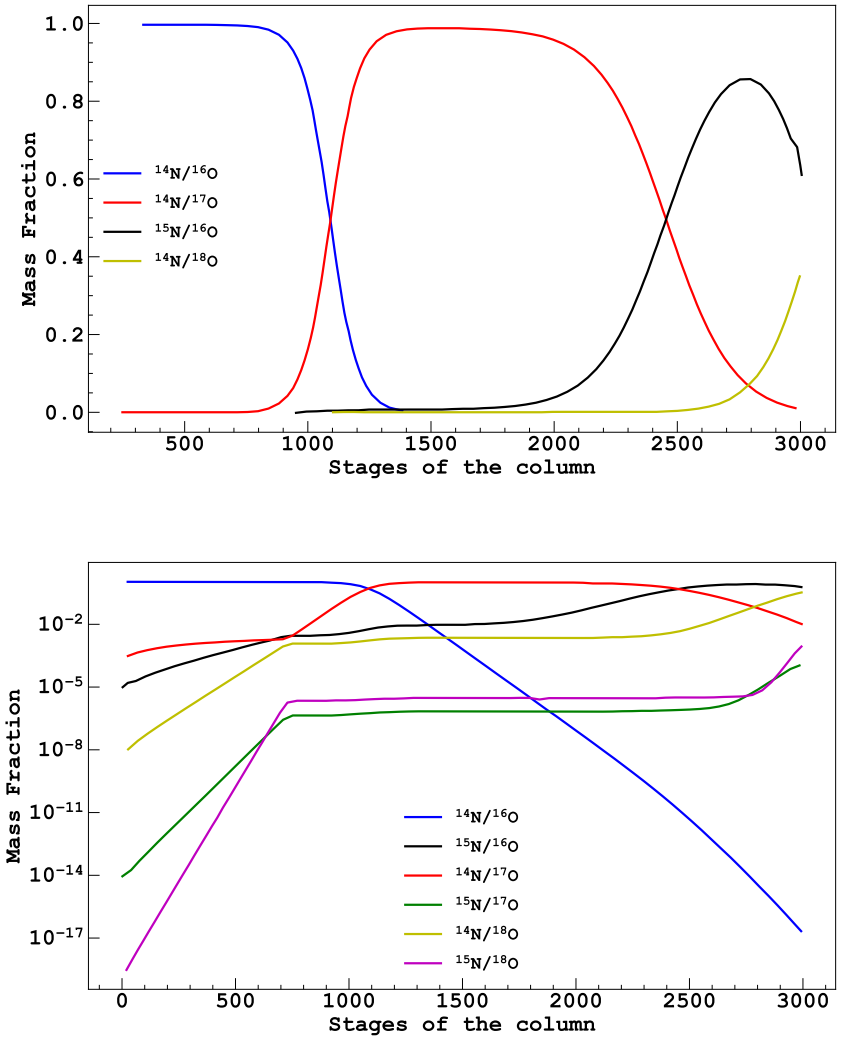

Figure 7.14: Distribution of the isotopes inside the column (bottom in log scale) for Seruci-1 (NO)

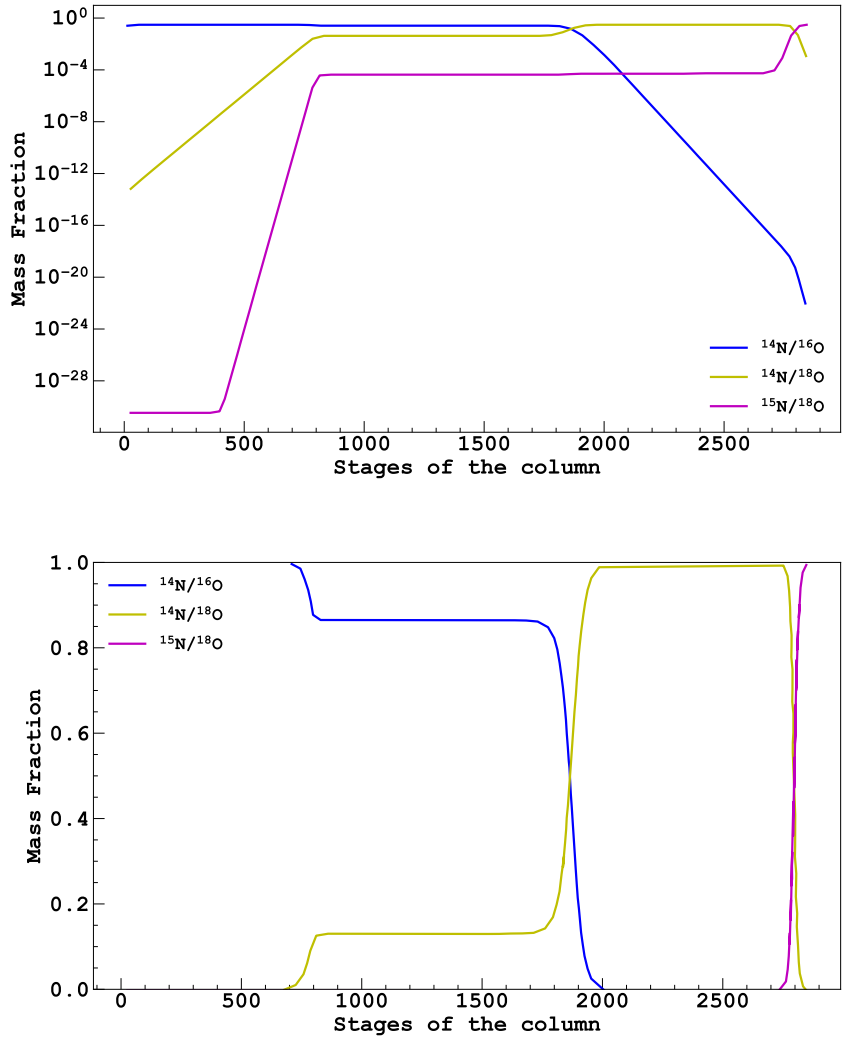

Figure 7.15: Distribution of the isotopes inside the column (bottom in log scale) for Seruci-F (NO).

Parameters	Values
P	1.0 bar
T	121.3 K
F	16 kg/h
L	800 kg/h
$x_{B,^{14}N^{17}O}$	0.937458
M (kg/h)	0.005431
N	2870
Nr	700

Table 7.26: Input parameters used to simulate NO distillation in Seruci-1.

Output steam mass flows				
		D (kg/h)	M (kg/h)	B (kg/h)
		15.903725	0.005431	0.090841
Composition				
	F	D	M	B
$^{14}N^{16}O$	0.993939	0.999939	0.048870	$2.49{\cdot}10^{-17}$
$^{15}N^{16}O$	0.003631	$6.39{\cdot}10^{-06}$	0.011464	0.637730
$^{14}N^{17}O$	0.000379	$5.45{\cdot}10^{-05}$	0.937458	0.001157
$^{15}N^{17}O$	0.000001	$5.03{\cdot}10^{-15}$	$7.27{\cdot}10^{-07}$	0.000176
$^{14}N^{18}O$	0.002043	$4.86{\cdot}10^{-09}$	0.002204	0.359704
$^{15}N^{18}O$	0.000007	$1.26{\cdot}10^{-19}$	$3.10{\cdot}10^{-06}$	0.001233

Table 7.27: Output parameters for NO distillation in Seruci-1.

NO: each with high purity and with sufficient production rate (as shown in the following tabular).

Component flows				
	F (kg/h)	D (kg/h)	M (kg/h)	B (kg/h)
$^{14}N^{16}O$	15.903024	15.902756	0.000265	$2.26{\cdot}10^{-18}$
$^{15}N^{16}O$	0.058096	0.000102	$6.23{\cdot}10^{-05}$	0.057932
$^{14}N^{17}O$	0.006064	0.000868	0.005091	0.000105
$^{15}N^{17}O$	0.000016	$7.99{\cdot}10^{-14}$	$3.95{\cdot}10^{-09}$	0.000016
$^{14}N^{18}O$	0.032688	$7.73{\cdot}10^{-08}$	$1.20{\cdot}10^{-05}$	0.032676
$^{15}N^{18}O$	0.000112	$2.01{\cdot}10^{-18}$	$1.68{\cdot}10^{-08}$	0.000112

Table 7.28: Output mass flows for NO distillation in Seruci-1.

Input parameters	Values
P	0.300 bar
T	111.74 K
F	0.090841 kg/h
L	22.0 kg/h
$x_{B,^{15}N^{18}O}$	0.999
$x_{SP1,^{14}N^{18}O}$	0.999
SP1	1950
N	2725
Nr	764

Table 7.29: Input parameters used to simulate NO distillation in Seruci-F.

Output steam mass flows			
	D (kg/h)	S1 (kg/h)	B (kg/h)
	0.058018	0.032714	0.000109
Composition			
	D	S1	B
$^{15}N^{16}O$	0.998188	0.000910	$4.64{\cdot}10^{-23}$
$^{14}N^{17}O$	0.001812	$1.48{\cdot}10^{-27}$	$9.39{\cdot}10^{-31}$
$^{14}N^{18}O$	$4.24{\cdot}10^{-16}$	0.998999	0.000999
$^{15}N^{18}O$	$1.06{\cdot}10^{-30}$	$9.03{\cdot}10^{-05}$	0.999000

Table 7.30: Output parameters for NO distillation in Seruci-F.

Component flows			
	D (kg/h)	S1 (kg/h)	B (kg/h)
$^{15}N^{16}O$	0.057913	$2.98{\cdot}10^{-05}$	$5.06{\cdot}10^{-27}$
$^{14}N^{17}O$	0.000105	$4.86{\cdot}10^{-29}$	$1.03{\cdot}10^{-34}$
$^{14}N^{18}O$	$2.46{\cdot}10^{-17}$	0.032682	$1.09{\cdot}10^{-07}$
$^{15}N^{18}O$	$6.16{\cdot}10^{-32}$	$2.96{\cdot}10^{-06}$	0.000109

Table 7.31: Output mass flows in Seruci-F (NO).

Isotopes	Mass flow (kg/h)	Mass flow (kg/year)	purity %
$^{12}C^{16}O$	9.868960	$8.65 \cdot 10^4$	99.4
$^{13}C^{16}O$+$^{12}C^{17}O$	0.051741	453.25	99.0
$^{12}C^{18}O$+$^{13}C^{17}O$	0.015016	131.54	99.0
$^{13}C^{18}O$	0.003706	32.46	99.0
$^{14}N^{16}O$	15.90276	$1.39 \cdot 10^5$	100.0
$^{15}N^{16}O$	0.057913	507.31	99.8
$^{14}N^{17}O$	0.005091	44.60	93.7
$^{14}N^{18}O$	0.032682	286.29	99.9
$^{15}N^{18}O$	0.000109	0.95	99.9

Table 7.32: Summary of output mass flows for NO and CO isotopes.

7.4 Germanium isotopic enrichment for LEGEND

After having demonstrated in 6.3.3 how we can exploit Seruci-1 to produce chemically pure liquid argon for the veto of LEGEND, we are currently exploring how the Aria project could provide an alternative for producing germanium for future development of the LEGEND project. So far LEGEND has reached an isotope 76 concentration of 86.8% ([81]) compared to its natural abundance of 7.7%. Germanium is a solid at cryogenic or ambient temperatures, so to separate it, we need to work with germane, the GeH_4 molecule, which undergoes a phase transition from liquid to gas at cryogenic temperatures and pressures near atmospheric pressure. Therefore, in this chapter, we will study the conditions that must be satisfied to produce germanium at the desired concentration for LEGEND within reasonable time frames. A similar procedure has already been described in [148].

Similar to the optimization procedure for CO and NO, we are considering a long-term project for Aria, and therefore, we are not considering columns that are already under construction, such as Seruci-1. Instead, we will design distillations for the future. The simulation optimization process is similar to the one used for CO and NO, so we will not repeat the entire procedure here. Instead, we will show only the key moments and the final results.

Assuming that in the future we will be able to build the Seruci-F distillation column described in the previous section for the distillation of CO and NO, we will optimize the conditions and operational parameters to ensure its suitability for the distillation of GeH_4 as well. We are considering the case of a 350 m tall column, using Pro-pack as the packing material, with a diameter of 12 cm (essentially the maximum achievable with Pro-pack [149]). The HETP is estimated to be 2.5 cm, resulting in a total of 14,500 stages. Similarly to the cases of CO and NO, the relative volatility used in Hysys has been adjusted from the actual values to account for a reduced number of stages in the simulation. This adjustment is necessary because the program is not able to handle simulations with more than approximately 3000 stages.
The estimation of relative volatility is complicated. In [150], instead of directly measuring the relative volatility between $^{76}GeH_4$ and its isotopes, an assumption is made based on known measurements of volatilities between different isotopes of Si_4, CH_4, SiF_4, and other compounds. A relationship between 1-α (where α represents the relative volatility) and the atomic masses of the elements and isotopes under consideration is hypothesized. Further details can be found in [151], Chapter 6. Using this hypothesis, the relative volatilities between different isotopes of GeH_4 at 1 bar are calculated. Subsequently, exploiting the Antoine equation 4.15, the variation of relative volatility with different pressures and saturation temperatures is reconstructed. As done in the previous CO and NO chapter, we consider the future and optimistic scenario of operating at pressures below atmospheric pressure, specifically at 0.25 bar. The lower pressure increases the volatility and consequently improves our ability to separate the isotopes. The table below 7.33 summarizes the values of the volatilities:

Hydraulic parameters of the packing material are evaluated similarly to what has been done for CO and NO. In particular, considering a maximum diameter of 12 cm, we assess the maximum feed flow rate (F) and liquid flow rate in the column (L) that the hydraulic system can support. As has been explained in the previous section, we will state that an inlet flow rate of approximately 1 kg/h can be used (slightly exceeding this value would not significantly increase the distilled quantity). As for the liquid flow rate, L is set to 50 kg/h,

Isotope	α
$^{76}GeH_4$	1.00121
$^{74}GeH_4$	1.00099
$^{73}GeH_4$	1.00086
$^{72}GeH_4$	1.00073
$^{70}GeH_4$	1.00000

Table 7.33: Relative volatility for $GeH_4$1.00000 isotopes (always with respect to $^{76}GeH_4$) at p = 0.25 bar and T = 161.1 K used for Seruci-F.

which is essentially the upper limit for this type of packing. Additionally, it is necessary to ensure that the distillate from the top of the column has a purity of 86.8% for the 76 isotopes (higher purities would result in lower outlet flow rates). To summarize, the input parameters for the simulation are the following 7.34.

Parameters	Value
P	0.25 bar
T	161.1 K
F	1 kg/h
L	50 kg/h
$x_{B,76}$	0.868
N	145000
Nr	1000

Table 7.34: Column parameters used for the simulation of Seruci-F for GeH_4 distillation

Since these parameters have been chosen, and not measured, to optimize the column we decided not to define any error. Here Nr is the input feed location and it has been optimized to maximize the production rate D. $x_{B,76}$ indicates the concentration of $^{76}GeH_4$ is the distillate B. The outputs of the simulation are in table 7.35 and the distribution of the concentration of the different isotopes is 7.16.

Output steam mass flows			
	F (kg/h)	D (kg/h)	B (kg/h)
	1.0000	0.9844	0.0156
Compositions			
	F	D	B
$^{76}GeH_4$	0.0773	0.06477	0.8680
$^{74}GeH_4$	0.3650	0.3688	0.2232
$^{73}GeH_4$	0.0775	0.07864	0.005273
$^{72}GeH_4$	0.2745	0.2788	0.003475
$^{70}GeH_4$	0.2057	0.2090	0.00007025

Table 7.35: .Results of the simulation after optimization for $^{76}GeH_4$ production.

The effectiveness of the optimizations can be observed from the concentration distribution within the column. There are no regions in the column where the concentrations remain unchanged, particularly concerning the 76 isotopes. This indicates that we are

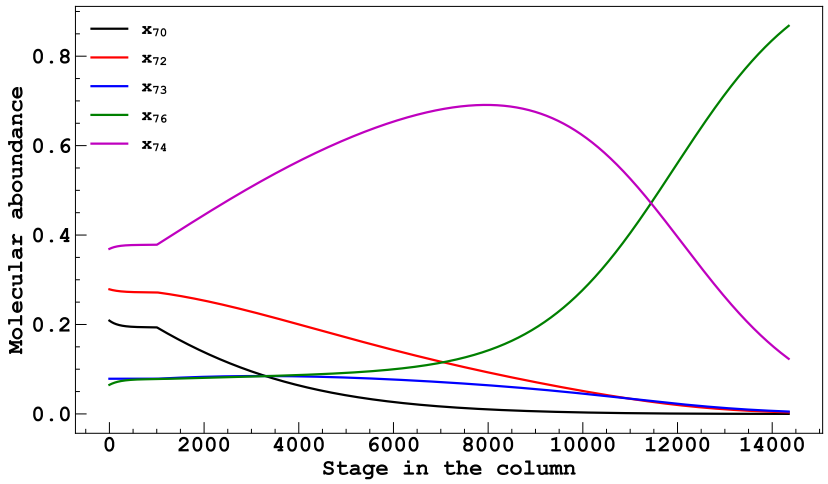

Figure 7.16: Distribution of the isotopes concentrations inside the column Seruci-F for $^{76}GeH_4$ production.

effectively using the column throughout its entirety. The most important data from the table is the production rate of 0.0156 kg/h, equivalent to 374 g/day. Overall, only 1.56% of the incoming germane in the feed is used, while the remaining portion exits from under the column and is not used (in addition to the amount used to fill the column). However, this production rate is insufficient as it would take approximately 7 years to produce the required tons.
However, we can now consider one of the most important aspects of the Pro-pack, which is its small diameter of 2.5 cm. On one hand, this is a disadvantage as it limits the flow rates in the column, which would subsequently increase the production time at the same required purity [104]. On the other hand, the compact size allows for the insertion of multiple columns within the mine where Seruci-1 is being constructed. If we had n columns, the time required to produce the desired tons would be 7 years/n. The columns could be identical and maintained under the same thermal conditions, eliminating the need to replicate the entire cooling and control system n times. On the other side, it could be extended to accommodate multiple columns, which could also be housed within a single external cylinder forming a single unit. Of course, considering the high cost of the packing, a compromise is necessary, and it has been determined that a reasonable solution could involve n=5 columns. With 5 columns, the production time could be reduced to approximately 1.5 years of continuous operation, which is certainly achievable.

In summary, we have explored the potential of the Aria project beyond the argon distillation. A distillation column using Pro-Pack as the packing material and integrated alongside Seruci-1, comprehending 5 internal columns with a diameter of 2.5 cm each, could efficiently produce the isotopes required by LEGEND. The column could also be exploited for the production of CO and NO isotopes, which have various applications, particularly in the medical and biochemical fields. Overall, in the past two chapters, we have demonstrated the importance of the Aria project, both in the immediate term by chemically purifying argon for DarkSide-50, in the medium term by producing oxygen isotopes under experimental conditions already achieved in the Seruci-0 prototype, and in the long term by considering the potential expansion of the project with the construction of additional columns.

Chapter 8

Conclusions

The topics of this thesis are strongly connected to the search for dark matter, in particular through direct interactions between WIMPs and a target material, specifically argon. One of the most promising projects in this field is DarkSide and in particular DarkSide-20k, which is currently under construction. Through an analysis of the results from the DarkSide-50 experiment, we have defined the required purity specifications for the argon used in DarkSide-50 based on the findings in [61] and in Figure 3.1. To reach this goal, it is fundamental to establish a production and purification chain for argon, which, after extraction from the Urania facility, must undergo purification by the primary subject of this thesis, which is the Aria project. Through simulations, we demonstrated the potential to reduce impurities to a level as low as 10^{-30} (actually eliminating them) while maintaining a satisfactory production rate.
Considering the argon required for the DarkSide experiment and for LEGEND-1000 (which requires argon as a veto in the search for neutrinoless beta decay events), both can be produced within a few months, assuming we only need to remove nitrogen (since other contaminants may already be suppressed in Urania) and carry out a single distillation. Alternatively, if a two-step process is necessary (extracting from the top and then from the bottom) to effectively suppress all contaminants, it would require approximately 10 months of running to accomplish.
A fundamental part of the thesis was dedicated to studying the simulation systems used for distillation. In particular, rigorous techniques were compared to shortcuts (using simplified formulas), two-component, and multi-component approaches. The commercial simulation software Hysys was employed for the simulations [121]. The results of simulations conducted in a previous study [1], which used a non-rigorous two-component approach, were reproduced and further analyzed with rigorous and multi-component approaches. It was demonstrated that, under the conditions of argon isotopic distillation in Seruci-1, the multi-component approach was not necessary, thus confirming the findings of that paper.
Furthermore, extensive analyses were carried out about the last run of the distillation column, Seruci-0, during which separation of argon isotopes ^{36}Ar, ^{38}Ar, and ^{40}Ar was achieved. The Universal Gas Analyzer and its calibration were also discussed. An HETP of 13 cm was measured, consistent with errors in the results of the previous run of Seruci-0, which was conducted with nitrogen.
We then demonstrated, through simulations, which configuration optimizes the production of oxygen isotopes ^{17}O and ^{18}O at acceptable concentrations for medical diagnostic purposes. Specifically, we observed that it is possible to produce, for instance, 50 kg of ^{18}O at 90% purity within a year of running a single distillation.
Finally, we have considered the potential beyond the argon applications of the Aria project.

In particular, to determine how to extend the project once the main distillation of argon for DarkSide is completed, we simulated the capacity to separate all isotopic combinations of CO and NO molecules. These can be extracted with acceptable concentrations provided that another distillation column is employed, with the same height but a smaller diameter and made of a different packing material. The reduced diameter would allow for the installation of multiple columns side by side (all within the same Seruci-1 cave). This multi-column structure would enable the production of approximately 87% pure germane $^{76}GeH_4$. With this setup, the one tonne of germanium required by LEGEND to produce germanium crystals could be obtained within 1.5 years of running.
This thesis has successfully demonstrated, through simulations based on and corroborated by experimental results, the potential of the Aria project concerning the following aspects:

1. The capability to distillate chemically pure argon for DarkSide-20k and LEGEND.
2. The distillation of argon purified from the ^{39}Ar isotope for DarkSide-LowMass.
3. The short-term distillation of oxygen isotopes, as achieved in the Seruci-0 prototype configuration.
4. The long-term separation of CO and NO isotopes, introducing a possible future project expansion with an additional distillation column.
5. Also in the long term, the distillation of ^{76}Ge for LEGEND.

My specific personal contributions to the project involved:

1. Analyzing reconstructed waveforms and fitting them to investigate the effects of potential nitrogen or oxygen concentrations on the triplet lifetime of argon scintillation.
2. Conducting all simulations and optimizations reported in the thesis using Hysys software or by performing calculations directly.
3. Performing calibration and tuning of the UGA for the argon run in Seruci-0.

Overall, this study has emphasized how the Aria project constitutes an essential step in creating the necessary conditions and producing the required materials for the projects dedicated to dark matter research and neutrino-less double beta decay, as they are two of the most crucial topics in modern physics research. In conclusion, I would like to underline the groundbreaking potential of the Aria project, which has been the main topic of this thesis.

Bibliography

[1] Agnes, P., et al. "Separating 39 Ar from 40 Ar by cryogenic distillation with Aria for dark-matter searches." The European Physical Journal C 81.4 (2021): 359.

[2] 20k Collaboration. "Measurement of isotopic separation of argon with the prototype of the cryogenic distillation plant Aria for dark matter searches." arXiv preprint arXiv:2301.09639 (2023).

[3] Bertone, Gianfranco, and Dan Hooper. "History of dark matter." Reviews of Modern Physics 90.4 (2018): 045002.

[4] Blumenthal, George R., et al. "Formation of galaxies and large-scale structure with cold dark matter." Nature 311.5986 (1984): 517-525.

[5] Aalseth, Craig E., et al. "DarkSide-20k: A 20 tonne two-phase LAr TPC for direct dark matter detection at LNGS." The European Physical Journal Plus 133 (2018): 1-129.

[6] Back, Henning O., et al. "A Facility for Low-Radioactivity Underground Argon." arXiv preprint arXiv:2203.09734 (2022).

[7] Agnes, Paolo, et al. "First results from the DarkSide-50 dark matter experiment at Laboratori Nazionali del Gran Sasso." Physics Letters B 743 (2015): 456-466.

[8] Cui, Xiangyi, et al. "Dark matter results from 54-ton-day exposure of PandaX-II experiment." Physical review letters 119.18 (2017): 181302.

[9] Agnes, P., et al. "Low-mass dark matter search with the DarkSide-50 experiment." Physical review letters 121.8 (2018): 081307.

[10] Mattewh Newby, MilkyWay@home

[11] Stefanizzi, Riccardo. "Ritardi temporali da lenti gravitazionali su scala di ammassi di galssie ed applicazioni per la misura della costante di Hubble." (2018).

[12] Giovanetti, Cara, et al. "Joint cosmic microwave background and big bang nucleosynthesis constraints on light dark sectors with dark radiation." Physical review letters 129.2 (2022): 021302.

[13] Mather, John C., et al. "A preliminary measurement of the cosmic microwave background spectrum by the Cosmic Background Explorer (COBE) satellite." Astrophysical Journal, Part 2-Letters (ISSN 0004-637X), vol. 354, May 10, 1990, p. L37-L40. 354 (1990): L37-L40.

[14] Bennett, C. L., et al. "Seven-year wilkinson microwave anisotropy probe (WMAP*) observations: Are there cosmic microwave background anomalies?." The Astrophysical journal supplement series 192.2 (2011): 17.

[15] Aghanim, Nabila, et al. "Planck 2018 results-VI. Cosmological parameters." Astronomy Astrophysics 641 (2020): A6.

[16] Roszkowski, Leszek, Enrico Maria Sessolo, and Sebastian Trojanowski. "WIMP dark matter candidates and searches—current status and future prospects." Reports on Progress in Physics 81.6 (2018): 066201.

[17] Han, Tao, Zhen Liu, and Shufang Su. "Light neutralino dark matter: direct/indirect detection and collider searches." Journal of High Energy Physics 2014.8 (2014): 1-37.

[18] Del Nobile, Eugenio. "The Theory of Direct Dark Matter Detection." (2022).

[19] Bernabei, R., et al. "Dark matter investigation by DAMA at Gran Sasso." International Journal of Modern Physics A 28.16 (2013): 1330022.

[20] Bernabei, Rita, et al. "Dark Matter with DAMA/LIBRA and its perspectives." Journal of Physics: Conference Series. Vol. 2586. No. 1. IOP Publishing, 2023.

[21] Cebrian, Susana, et al. "Status of the ANAIS experiment at Canfranc." Nuclear Physics B-Proceedings Supplements 114 (2003): 111-115.

[22] Amaré, J., et al. "Annual modulation results from three-year exposure of ANAIS-112." Physical Review D 103.10 (2021): 102005.

[23] Adhikari, G., et al. "Search for a dark matter-induced annual modulation signal in NaI (Tl) with the COSINE-100 experiment." Physical review letters 123.3 (2019): 031302.

[24] Tralli, Francesco. "Elements of Subnuclear Physics." (2019)

[25] Tongyan Lin. Dark matter models and direct detection. PoS, 333:009, 2019.

[26] Rau, Wolfgang. "Dark matter search experiments." Physics of Particles and Nuclei 42 (2011): 650-660.

[27] Billard, Julien, et al. "Direct detection of dark matter—APPEC committee report." Reports on Progress in Physics 85.5 (2022): 056201.

[28] Schumann, Marc. "Direct detection of WIMP dark matter: concepts and status." Journal of Physics G: Nuclear and Particle Physics 46.10 (2019): 103003.

[29] Suzuki, Yoichiro. "The super-kamiokande experiment." The European Physical Journal C 79 (2019): 1-18.

[30] Doglioni, Caterina, and Dan Tovey. "Searching for Dark Matter with the ATLAS detector." Advances in Cosmology: Science-Art-Philosophy. Cham: Springer International Publishing, 2022. 93-115.

[31] Kerszberg, Daniel, et al. "Search for dark matter annihilation with a combined analysis of dwarf spheroidal galaxies from Fermi-LAT, HAWC, HESS, MAGIC and VERITAS." (2023).

[32] Giuliani, F., and DEAP/CLEAN collaboration. "Hunting the dark matter with DEAP/CLEAN." AIP Conference Proceedings. Vol. 1200. No. 1. American Institute of Physics, 2010.

[33] Westerdale, S., and DEAP-3600 Collaboration. "Analysis and Dark Matter Search Results from DEAP-3600 with 231 Live Days at SNOLAB." Journal of Physics: Conference Series. Vol. 1468. No. 1. IOP Publishing, 2020.

[34] Kwong, John, et al. "Liquefied noble gas detectors for detection of nuclear materials." IEEE Transactions on Nuclear Science 60.2 (2013): 652-657.

[35] Doke, Tadayoshi, et al. "Absolute scintillation yields in liquid argon and xenon for various particles." Japanese journal of applied physics 41.3R (2002): 1538.

[36] Segreto, Ettore. "Properties of liquid argon scintillation light emission." Physical Review D 103.4 (2021): 043001.

[37] Billard, J., E. Figueroa-Feliciano, and L. Strigari. "Implication of neutrino backgrounds on the reach of next-generation dark matter direct detection experiments." Physical Review D 89.2 (2014): 023524.

[38] O'Hare, Ciaran AJ. "New definition of the neutrino floor for direct dark matter searches." Physical Review Letters 127.25 (2021): 251802.

[39] Schumann, Marc. "Dark matter search with liquid noble gases." arXiv preprint arXiv:1206.2169 (2012).

[40] Picciau, Emmanuele. "Low-energy signatures in DarkSide-50 experiment and neutrino scattering processes." (2022).

[41] Chepel, Vitaly, and Henrique Araújo. "Liquid noble gas detectors for low energy particle physics." Journal of Instrumentation 8.04 (2013): R04001.

[42] Akimov, Dmitry Yu, et al. Two-Phase Emission Detectors. World Scientific, 2021.

[43] Aalbers, J., et al. "A next-generation liquid xenon observatory for dark matter and neutrino physics." Journal of Physics G: Nuclear and Particle Physics 50.1 (2022): 013001.

[44] Szydagis, M., et al. "NEST: a comprehensive model for scintillation yield in liquid xenon." Journal of Instrumentation 6.10 (2011): P10002.

[45] Szydagis, Matthew, et al. "A review of basic energy reconstruction techniques in liquid xenon and argon detectors for dark matter and neutrino physics using nest." Instruments 5.1 (2021): 13.

[46] Aprile, Elena, et al. "Dark matter results from 225 live days of XENON100 data." Physical review letters 109.18 (2012): 181301.

[47] Agostini, Matteo, et al. "Toward the discovery of matter creation with neutrinoless decay." Reviews of Modern Physics 95.2 (2023): 025002.

[48] https://www.lngs.infn.it/en/xenon

[49] Aprile, E., et al. "Projected WIMP sensitivity of the XENONnT dark matter experiment." Journal of Cosmology and Astroparticle Physics 2020.11 (2020): 031-031.

[50] Szydagis, Matthew, et al. "A review of basic energy reconstruction techniques in liquid xenon and argon detectors for dark matter and neutrino physics using nest." Instruments 5.1 (2021): 13.

[51] J. A. Cameron, J. Chen, Balraj Singh, and N. Nica. Nuclear data sheets for a = 37. Nuclear Data Sheets, 113:365–514, 2012.

[52] Zhang, Chao, and D-M. Mei. "Evaluation of cosmogenic production of 39Ar and 42Ar for rare-event physics using underground argon." Astroparticle Physics 142 (2022): 102733.

[53] Hitachi, Akira, et al. "Effect of ionization density on the time dependence of luminescence from liquid argon and xenon." Physical Review B 27.9 (1983): 5279.

[54] Hitachi, Akira. "Luminescence response and quenching models for heavy ions of 0.5 keV to 1 GeV/n in liquid argon and xenon." Instruments 5.1 (2021): 5.

[55] Agnes, P., et al. "The electronics, trigger and data acquisition system for the liquid argon time projection chamber of the DarkSide-50 search for dark matter." Journal of Instrumentation 12.12 (2017): P12011.

[56] Xiang, Xin. Cherenkov Related Backgrounds in the DarkSide-50 Experiment. Diss. Princeton University, 2018.

[57] Agnes, Paolo, et al. "DarkSide-50 532-day dark matter search with low-radioactivity argon." Physical Review D 98.10 (2018): 102006

[58] Agnes, P., et al. "The veto system of the DarkSide-50 experiment." Journal of Instrumentation 11.03 (2016): P03016.

[59] Doke, Tadayoshi, et al. "Let dependence of scintillation yields in liquid argon." Nuclear Instruments and Methods in Physics Research Section A: Accelerators, Spectrometers, Detectors and Associated Equipment 269.1 (1988): 291-296.

[60] Agnes, P. "Simulation of the argon response and light detection in a dual-phase TPC." Journal of Instrumentation 15.01 (2020): C01044.

[61] Acciarri, R., et al. "Effects of Nitrogen contamination in liquid Argon." Journal of Instrumentation 5.06 (2010): P06003.

[62] Morikawa, E., et al. "Argon, krypton, and xenon excimer luminescence: From the dilute gas to the condensed phase." The Journal of chemical physics 91.3 (1989): 1469-1477.

[63] Lippincott, W. H., et al. "Scintillation time dependence and pulse shape discrimination in liquid argon." Physical Review C 78.3 (2008): 035801.

[64] Boccone, V., and ArDM Collaboration. "Development and test in liquid argon of the light readout system for the ArDM experiment." AIP Conference Proceedings. Vol. 1182. No. 1. American Institute of Physics, 2009.

[65] Kubota, Shinzou, Masahiko Hishida, and Akira Nohara. "Variation of scintillation decay in liquid argon excited by electrons and alpha particles." Nuclear Instruments and Methods 150.3 (1978): 561-564.

[66] Segreto, Ettore. "Properties of liquid argon scintillation light emission." Physical Review D 103.4 (2021): 043001.

[67] Negulescu, Ana-Maria, and Patrick Mehlen. "Dependence receptors–the dark side awakens." The FEBS journal 285.21 (2018): 3909-3924.

[68] Kimura, Masato, et al. "Measurement of liquid argon scintillation and ionization response on nuclear recoils under electric fields up to 3 kV/cm." Journal of Instrumentation 15.03 (2020): C03042.

[69] Zuzel, Grzegorz, et al. "The darkside experiment: Present status and future." Journal of Physics: Conference Series. Vol. 798. No. 1. IOP Publishing, 2017.

[70] https://2022.kashiwa-darkmatter-symposia.org/posters.html. Talk Slides at Kashiwa 2022 symposium by M. Kimura at beahlf of the DarkSide group

[71] Carnesecchi, F. "Light detection in DarkSide-20k." Journal of Instrumentation 15.03 (2020): C03038.

[72] Abi, B., et al. "The single-phase ProtoDUNE technical design report." arXiv preprint arXiv:1706.07081 (2017).

[73] https://indico.cern.ch/event/1082486/contributions Talk slides at TeVPA 2022 by Marek Walczakon behalf of The Global Argon Dark Matter Collaboration

[74]

[75] Agnes, Paolo. "Direct Detection of Dark Matter with DarkSide-20k." EPJ Web of Conferences. Vol. 280. EDP Sciences, 2023.

[76] Agnes, P., et al. "Sensitivity projections for a dual-phase argon TPC optimized for light dark matter searches through the ionization channel." Physical Review D 107.11 (2023): 112006.

[77] Saes getters, www.saesgetters.com

[78] Agnes, P., et al. "A study of events with photoelectric emission in the DarkSide-50 liquid argon Time Projection Chamber." Astroparticle Physics 140 (2022): 102704.

[79] Cadeddu, Matteo. "DarkSide-20k sensitivity, directional dark matter detection and the role of coherent elastic neutrino-nucleus scattering background." (2018).

[80] The DarkSide-50 Collaboration, A study of isolated single-electron signals with the double-phase liquid-argon TPC DarkSide-50 at LNGS. *Currently under review*

[81] Massarczyk, Ralph, et al. The Large Enriched Germanium Experiment for Neutrinoless Decay (LEGEND-1000 Preconceptual Design Report). No. LA-UR-21-27433. Los Alamos National Lab.(LANL), Los Alamos, NM (United States), 2021.

[82] Dolinski, Michelle J., Alan WP Poon, and Werner Rodejohann. "Neutrinoless double-beta decay: status and prospects." Annual Review of Nuclear and Particle Science 69 (2019): 219-251.

[83] Forero, D. V., M. Tortola, and J. W. F. Valle. "Neutrino oscillations refitted." Physical Review D 90.9 (2014): 093006.

[84] Branco, Gustavo C., and M. N. Rebelo. "Building the full Pontecorvo-Maki-Nakagawa-Sakata matrix from six independent Majorana-type phases." Physical Review D 79.1 (2009): 013001.

[85] Ejiri, H. "Neutrinos and Spin Coupled Dark Matters Studied by ELEGANT V and ELEGANT VI." Origin of Matter and Evolution of Galaxies in the Universe 1996 (1997): 160.

[86] Agostini, Matteo, et al. "Measurement of the half-life of the two-neutrino double beta decay of 76Ge with the GERDA experiment." Journal of Physics G: Nuclear and Particle Physics 40.3 (2013): 035110.

[87] Amore, Isabella, et al. "NEMO: A Project for a km3 Underwater Detector for Astrophysical Neutrinos in the Mediterranean Sea." International Journal of Modern Physics A 22.21 (2007): 3509-3520.

[88] Barabash, A. S., et al. "Final results of the Aurora experiment to study 2 decay of Cd 116 with enriched Cd 116 WO 4 crystal scintillators." Physical Review D 98.9 (2018): 092007.

[89] "Search for Majorana neutrinos exploiting millikelvin cryogenics with CUORE." Nature 604, no. 7904 (2022): 53-58.

[90] "Search for Majorana neutrinos with the first two years of EXO-200 data." Nature 510, no. 7504 (2014): 229-234.

[91] Gando, Yoshihito. "First results of KamLAND-Zen 800." Journal of Physics: Conference Series. Vol. 1468. No. 1. IOP Publishing, 2020.

[92] Edzards, Frank. Characterization of Point Contact Germanium Detectors and Development of Signal Readout Electronics for LEGEND. Diss. TU München Munich, 2021.

[93] Zsigmond, Anna Julia, and LEGEND Collaboration. "LEGEND: The future of neutrinoless double-beta decay search with germanium detectors." Journal of Physics: Conference Series. Vol. 1468. No. 1. IOP Publishing, 2020.

[94] Abgrall, N., et al. "LEGEND-1000 preconceptual design report." arXiv preprint arXiv:2107.11462 (2021)

[95] Mirza, M. Ibrahim. "Mitigation Strategies for ^{42} Ar/^{42} K Background Reduction using Encapsulation with Ultra-Pure Plastic for the LEGEND Experiment." arXiv preprint arXiv:2209.07598 (2022).

[96] E. Morikawa et al., Argon, Krypton an Xenon excimer luminescence: from dilute gas to the condensed phase, J. Phys. Chem. 91 (1989) 1469

[97] Agnes, P., et al. "Characterization of the scintillation time response of liquid argon detectors for dark matter search." Journal of Instrumentation 16.11 (2021): P11026.

[98] M.J. Carvalho et al., Luminescence decay in condensed Argon under high energy excitation, J. Lumin. 18-19 (1979) 487

[99] Bellamy, EH others, et al. "Absolute calibration and monitoring of a spectrometric channel using a photomultiplier." Nuclear Instruments and Methods in Physics Research Section A: Accelerators, Spectrometers, Detectors and Associated Equipment 339.3 (1994): 468-476.

[100] DEAP Collaboration deap-papers@ snolab. ca, et al. "The liquid-argon scintillation pulseshape in DEAP-3600." The European Physical Journal C 80 (2020): 1-12.

[101] Agnes, P., Albuquerque, I. F. M., Alexander, T., Alton, A. K., Ave, M., Back, H. O., ... & DarkSide-50 Collaboration. (2023). Search for low-mass dark matter WIMPs with 12 ton-day exposure of DarkSide-50. Physical Review D, 107(6), 063001.

[102] Agnes, P., et al. "Calibration of the liquid argon ionization response to low energy electronic and nuclear recoils with DarkSide-50." Physical Review D 104.8 (2021): 082005.

[103] Acciarri, R., et al. "Oxygen contamination in liquid Argon: combined effects on ionization electron charge and scintillation light." Journal of Instrumentation 5.05 (2010): P05003.

[104] Kister, Henry Z., et al. Distillation design. Vol. 1. New York: McGraw-Hill, 1992.

[105] Agnes, P., et al. "Separating 39 Ar from 40 Ar by cryogenic distillation with Aria for dark-matter searches." The European Physical Journal C 81.4 (2021): 359.

[106] https://en.citizendium.org/wiki/User:MiltonBeychok/ImageGallery

[107] Back, H. O., et al. "136Xe enrichment through cryogenic distillation." Journal of Instrumentation 12.09 (2017): P09033.

[108] O.R. Frisch, Progress in Nuclear Physics. Volume 6: The Leading International Review Series in Nuclear Physics, Pergamon Press, London U.K. New York U.S.A. Paris France (1957).

[109] Dreisbach, R. R., and R. S. Spencer. "Infinite Points of Cox Chart Families and dt/dP Values at any Pressure. Mathematical Formulas." Industrial Engineering Chemistry 41.1 (1949): 176-181.

[110] Thomson, George Wm. "The Antoine equation for vapor-pressure data." Chemical reviews 38.1 (1946): 1-39.

[111] Canongia Lopes, J. N., et al. "Calculation of vapor pressure isotope effects in the rare gases and their mixtures using an integral equation theory." The Journal of chemical physics 118.11 (2003): 5028-5037.

[112] Yin, Daxu, and Alexander D. MacKerell Jr. "Combined ab initio/empirical approach for optimization of Lennard–Jones parameters." Journal of Computational Chemistry 19.3 (1998): 334-348.

[113] Boato, G., et al. "Vapour pressure of isotopic liquids: III.—Some corrections to previous papers." Il Nuovo Cimento (1955-1965) 20 (1961): 87-93.

[114] Phillips, James T., Carl U. Linderstrom-Lang, and Jacob Bigeleisen. "Liquid-Vapor Argon Isotope Fractionation from the Triple Point to the Critical Point. Mean Laplacian of the Intermolecular Potential in Liquid Argon." The Journal of Chemical Physics 56.10 (1972): 5053-5062.

[115] Lee, Myung W., Salomon Fuks, and Jacob Bigeleisen. "Vapor pressures of 36Ar and 40Ar. Intermolecular forces in solid and liquid argon." The Journal of Chemical Physics 53.10 (1970): 4066-4076.

[116] Ancona, E., G. Boato, and G. Casanova. "Vapour pressure of isotopic liquids." Il Nuovo Cimento (1955-1965) 24.1 (1962): 111-121.

[117] Clusius, Klaus, and Kuno Schleich. "Ergebnisse der Tieftemperaturforschung XXII. Zur Anreicherung von 15N durch Rektifikation von Stickoxyd." Helvetica Chimica Acta 42.1 (1959): 232-239.

[118] CLUSIUS, K.; VECCHI, M. Ergebnisse der Tieftemperaturforschung XXV. Weitere Rektifikationsversuche mit Stickoxyd. Helvetica Chimica Acta, 1959, 42.6: 1921-1923.

[119] Boato, G., G. Casanova, and A. Levi. "Isotope effect in phase equilibria." The Journal of Chemical Physics 37.1 (1962): 201-202.

[120] H. J. H. Richardson, J. F. and J. R. Backhurst, Coulson and Richardson's CHEMICAL ENGINEERING, 5th Edition, vol. 2. Butterworth-Heinemann, 2002.

[121] https://www.aspentech.com/en/products/engineering/aspen-hysys

[122] Sundaram, Suresh, and Lawrence B. Evans. "Shortcut procedure for simulating batch distillation operations." Industrial engineering chemistry research 32.3 (1993): 511-518

[123] Lee, J. W., et al. "A graphical method for designing reactive distillation columns. II. The McCabe-Thiele method." Proceedings of the Royal Society of London. Series A: Mathematical, Physical and Engineering Sciences 456.2000 (2000): 1965-1978.

[124] Lee, J. W., et al. "A graphical method for designing reactive distillation columns. II. The McCabe-Thiele method." Proceedings of the Royal Society of London. Series A: Mathematical, Physical and Engineering Sciences 456.2000 (2000): 1965-1978.

[125] Copyright (C) 2000,2001,2002 Free Software Foundation, Inc. 51 Franklin St, Fifth Floor, Boston, MA 02110-1301 USA. Link to the lincence: https://commons.wikimedia.org/wiki/Commons:GNU_Free_Documentation_License,_version_1.2

[126] https://www.sulzer.com/en/shared/products/gauze-packings

[127] https://www.mks.com/f/cirrus-3-xd-atmospheric-pressure-gas-monitor

[128] Garcia, E. Sanchez. "DArT, a detector for measuring the 39Ar depletion factor." Journal of Instrumentation 15.02 (2020): C02044.

[129] Budzikiewicz, Herbert, and Ronald D. Grigsby. "Mass spectrometry and isotopes: a century of research and discussion." Mass spectrometry reviews 25.1 (2006): 146-157.

[130] Nowak, J., and Darkside Collaboration. Eur.Phys.J.C 81, 4, 359 (2021)

[131] https://www.process-insights.com/products-3/products-industrial/mass-spectrometers-gas-analyzers/

[132] R. Saldanha, H. Back, R. Tsang, T. Alexander, S. Elliott, S. Ferrara, E. Mace, C. Overman, M. Zalavadia, Phys. Rev. C100, 024608 (2019)

[133] Condon, Barrie. "Magnetic resonance imaging and spectroscopy: how useful is it for prediction and prognosis?." EPMA journal 2 (2011): 403-410.

[134] KIHARA, Hitoshi, et al. Method for concentrating oxygen isotope or isotopes. U.S. Patent No 8,337,802, 2012.

[135] Clusius, Klaus, and Kuno Schleich. "Ergebnisse der Tieftemperaturforschung XXII. Zur Anreicherung von 15N durch Rektifikation von Stickoxyd." Helvetica Chimica Acta 42.1 (1959): 232-239.

[136] KHOROSHILOV, A. V. Production of stable isotopes of light elements: past, present and future. In: Journal of Physics: Conference Series. IOP Publishing, 2018. p. 012002

[137] MATEESCU, Gheorghe D. ISMRM Workshop onCerebral Perfusion March 2004, Venice, Italy. 13

[138] Turchyn, Alexandra V., and Daniel P. Schrag. "Oxygen isotope constraints on the sulfur cycle over the past 10 million years." Science 303.5666 (2004): 2004-2007.

[139] JOHNS, T. F. Vapour pressures of some isotopic substances. In: Proceedings of the Symposium on Isotope Separation, Amsterdam. 1957. p. 85.

[140] Steffen, Vilmar, and Edson Antonio da Silva. "Steady-State Modeling of Equilibrium Distillation." Distillation-Innovative Applications and Modeling. IntechOpen, 2017.

[141] Bushberg, Jerrold T., and John M. Boone. The essential physics of medical imaging. Lippincott Williams Wilkins, 2011.

[142] Mateescu, Gheorghe D. "ISMRM Workshop on Cerebral Perfusion March 2004, Venice, Italy."

[143] https://cannoninstrument.com/distillation-packing.html

[144] CLUSIUS, Kalus; SCHLEICH, Kuno. Ergebnisse der Tieftemperaturforschung XX. Direkter Vergleich der Dampfdrucke von 14N2

[145] CLUSIUS, K., et al. Ergebnisse der Tieftemperaturforschung XXVI. Die Dampfdrucke im System 14NO/15NO zwischen Schmelz-und Siedepunkt. Helvetica Chimica Acta, 1959, 42.6: 1975-1984.

[146] https://encyclopedia.airliquide.com/

[147] CLUSIUS, Klaus; SCHLEICH, Kuno; VECCHI, Max. Ergebnisse der Tieftemperaturforschung XXIX. Über den abnorm grossen Dampfdruckunterschied zwischen 14N16O und 15N18O. Helvetica Chimica Acta, 1959, 42.7: 2654-2666.

[148] Adamchik, S. A., et al. "Ultrapurification of 76 Ge-enriched GeH 4 by distillation." Inorganic Materials 47 (2011): 694-696.

[149] https://www.sigmaaldrich.com/IT/it/product/aldrich/z210536

[150] Bornhorst, W. R., and Morey A. Ring. "Formation and cleavage of the germanium-germanium bond in digermane." Inorganic Chemistry 7.5 (1968): 1009-1011.

[151] TeGrotenhuis, Ward E., et al. Isotope Enrichment Using Microchannel Distillation Technology. No. PNNL-28208. Pacific Northwest National Lab.(PNNL), Richland, WA (United States), 2018.